Low-Cost Submersible Fluorometer for Fresh and Marine Water Environments

by

Joshua J. Creelman

Submitted in partial fulfilment of the requirements
For the degree of Master of Applied Science

at

Dalhousie University
Halifax, Nova Scotia
December 2022

Dalhousie University is located in Mi'kma'ki, the
Ancestral and unceded territory of the Mi'kmaq.
We are all Treaty people.

TABLE OF CONTENTS

LIST OF TABLES

LIST OF FIGURES

ABSTRACT

Fluorescence technology is a powerful tool for the detection of harmful algal blooms, oil spill response, oceanographic tracer experiments, and much more. Two ways of fluorescence detection are presented here, a novel microfluidic inlaid approach and a classical approach. The lower limit of detection for the microfluidic approach was 47 nM (27 ppb) Rhodamine, whereas the submersible had 0.39 nM (0.22 ppb). The classical approach is a submersible which was simulated, implemented, temperature calibrated and deployed for field trials. The submersible uses a digital lock-in amplifier, and the housing is made from off-the-shelf components. When temperature calibrating the device the commercial Turner Cyclops 7 was calibrated along side it, yielding comparable results. The prototype and commercial sensors were mounted to an underwater remotely operated vehicle which was deployed in the Gulf of Saint Lawrence for tracer studies.

LIST OF ABBREVIATIONS USED

LOD	limit of detection
OTS	off the shelf
ROV	remotely operated underwater vehicle
SUT	sample under interrogation
WLEF	white light excitation fluorescence
LOC	lab-on-chip
HAB	harmful algal bloom
CyanoHAB	cyanobacteria HAB
eDNA	environmental DNA
CDOM	chromophoric dissolved organic matter
RT-PCR	real time PCR
qPCR	quantitative PCR
DOM	dissolved organic matter
CEAS	cavity-enhanced absorption spectroscopy
PMMA	poly(methyl methacrylate)
RMSE	root-mean-square-error
DMA	direct memory access
ISR	interrupt service routine
SNR	signal to noise ratio
LPF	low pass filter
PCB	printed circuit board
TReX	Tracer Release Experiment

ACKNOWLEDGEMENTS

There have been many who have helped me along the way in this seemingly endless journey. Ben murphy has worked along my side since midway through my undergraduate degree and we have worked well together, helping each other along the way. When first joining the lab, it was Sean Morgan and Eddy Luy that introduced me to what the lab was all about, microfluidics and their novel idea the inlay. I would soon make friends with these two. Later joining the lab, or rather the oldest member returning, Andre Hendricks, who had designed the first nitrite sensor in the lab, quickly became my friend as we had both been quite the software enthusiasts. Each of the members had some expertise that would help with the others project, and it felt like we all synergised well. I would also have to thank Gabryelle Beland, an undergraduate at the time during her co-op, for helping me when first starting the fluorescence project.

My committee, both past and present, have given me valuable knowledge in their respective fields; Aaron MacNeil, my co-supervisor, Kamal El-Sankary, new internal committee member, Robert Beiko, past external supervisor, and Ghada Koleilat, new external committee member. A special thanks to my current committee members as they had both joined on such late notice. Another well deserved acknowledgement would have to go to Alison Chua, a fellow graduate student who without I would have not been able to calibrate and test my prototype so easily.

Most importantly, my supervisor Vincent Sieben, who has helped me the most. I still remember being recruited to the lab after the academic term had begun and how Vincent helped me join the department even though the deadline had passed. He has given me valuable guidance and knowledge ever step of the way.

CHAPTER 1 INTRODUCTION

1.1 Project Description

The goal of this work is to develop a microfluidic fluorescence spectroscopy approach that can be integrated with other lab-on-chip technologies for performing a variety of *in situ* measurements underwater that are reagent efficient. The thesis initially explores the development of a novel microfluidic inlaid approach for performing fluorescence measurements on-chip. However, the performance of the microfluidic cell required improvement for many applications. The remainder of the thesis is comprised of deep-dive improvements of the sub-systems. I show ray-tracing optical simulations, lock-in amplification signal processing, and finally the deployment of a low-cost and high performance submersible fluorometer.

This chapter will describe fundamentals and the overall thesis layout. Individual chapters will discus relevant contributions and brief literature reviews pertaining to their topic, prior to discussing my work. Chapter 2 introduces a microfluidic approach invented in the Sieben Laboratory for performing absorbance-based spectroscopy. My worked used this inlaid microfabrication technique to build and characterize a novel fluorescence cell. The final on-chip spectroscopy cell is capable of simultaneous measurements of absorbance and fluorescence. The outcome of Chapter 2 highlighted a requirement to attain better parts-per-billion limits of detection (LOD), typically required for oceanographic applications. Therefore, in Chapter 3, my work started on enhanced signal processing techniques. The chapter covers lock-in amplifier theory, simulations of lock-in detection, and finally my work on implementing a digital lock-in amplifier on a PIC microprocessor. Chapter 4 focuses on the optical configuration and optimization, ultimately designing a standalone and submersible fluorometer. Ray tracing simulations are performed in Optic Studios, where an optimized design was fully simulated to yield a calculated and anticipated calibration curve. Chapter 5 details the results from laboratory testing and temperature calibration. The chapter also demonstrates my novel fluorometer used in the Gulf of Saint Lawrence, Canada. The novel fluorometer was mounted alongside an off-the-shelf (OTS) commercial fluorometer, both of which were deployed on a remotely operated underwater vehicle (ROV). Chapter 6 is the summary of my work, and recommendations for future improvements and applications.

1.2 Background

1.2.1 Fundamentals of Fluorometry

To understand where fluorescence comes from in a molecule, the electronic and vibrational states will be explored using a Jablonski diagram as a visual aid as shown in Figure 1.1. Molecules begin in their ground electronic state S_0 [1]. Each electronic state has many vibrational states[1], [2]. Molecules become excited upon absorption of photon(s), typically in $<10^{-15}$ seconds [1], [3]. Depending on the energy absorbed, the molecule will be in either the S_1 or S_2 state [1]. If in the S_1 state the molecule undergoes internal conversion, loss of energy through internal vibration, and energy loss from external collisions until it has reached its lowest vibrational state for its electronic state [1], [3]. This period of loss of energy occurs around 10^{-10} to 10^{-12} seconds [1], [3]. If in the S_2 state rapid internal conversion occurs, causing a drop in vibrational states until the molecule is in the S_1 state [1]. This energy loss occurs in a period of approximately $<10^{-12}$ seconds [1]. Note there is an overlap in S_1 state's upper vibrational state and S_2 state's lower vibrational states [1]. Once in the lower vibrational level of the S_1 state energy dissipation between the S_1 state and S_0 state can be in the form of a photon [1], [3]. This photon would have lower energy, a longer wavelength, due to the vibrational losses [1]. A photon released from the transition from S_1 to S_0 is considered fluorescence [1], [3].

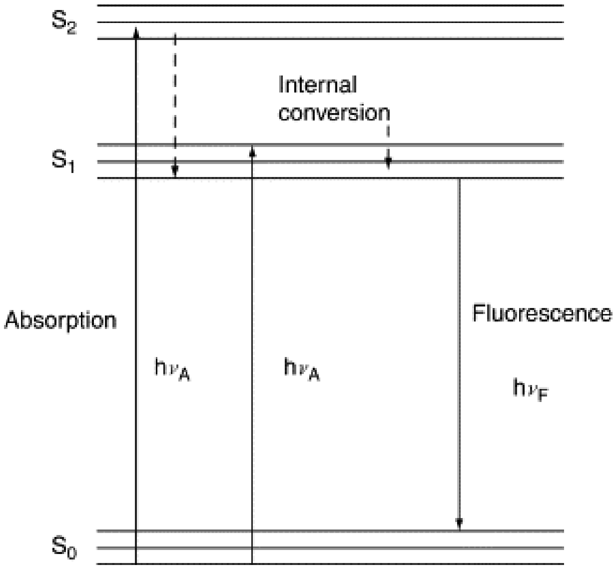

Figure 1.1 Jablonski diagram of a generic fluorescent material. Reprinted from reference [3].

Next it is important to understand the spectra of both the material's absorbance and emission. Coloured solutes absorb light of specific wavelengths [4]. Absorbance is defined as the amount of light attenuation across the target medium [4]. This attenuation can be observed by measuring the incident light intensity (I_0) prior to hitting a material, and by measuring the light that exits the material (I) [4]. This attenuation is dependant on three parameters, the concentration (C) of the absorber in the material in question, the optical path length in cm (l), and the molar attenuation coefficient ε (a function of wavelength) [4]. The formula describing the absorption phenomena is called the Beer-Lambert law, written in equation 1.1.

$$A = \varepsilon(\lambda)cl = -\log_{10}\left(\frac{I}{I_0}\right) \qquad 1.1$$

It is important to note that the molar attenuation coefficient is wavelength dependent [4]. The absorption spectra of materials are important to fluorometry as they can be used to identify the maximum absorbance versus wavelengths of excitation. These spectra are also known as excitation spectra [4]. Once the energy has been transferred to a molecule via an absorbance event, fluorescence may occur. The resulting intensity versus wavelength yields an emission spectrum [3]. The spectra usually are smeared (meaning horizontally stretched) due to collisional interactions with the environment and other molecules in the material [1].

Lastly, the intensity of fluorescence is proportional to a physical characteristic of the material, quantum yield (φ), and absorbed light [5]. Quantum yield is defined as the ratio between photons absorbed and fluorescent photons released [5]. Fluorescence intensity is described by equation 1.2. By rearranging equation 1.1 and substituting it into equation 1.2 a more general fluorescence equation can be obtained as seen in equation 1.3.

$$F = \varphi(I_0 - I) \tag{1.2}$$

$$F = \varphi I_0(1 - 10^{\varepsilon c l}) \tag{1.3}$$

1.2.2 Fluorometer Optical Design

From an instrumentation perspective, there are three main components to performing a fluorescence measurement: a light source, a sample under interrogation (SUT), and a photodetector. The simplest design would have a light source exciting the sample volume and a photodetector reading orthogonally from where the light source is positioned and beside the sample volume. This positioning minimizes light from the source reaching the detector, ultimately increasing the LOD for the sensor. Building upon this concept, the addition of lenses increases control of the light path, optimizing illumination and collection efficiency. Lensing the light source towards the sample and using lenses to focus a portion of the isotropic fluorescence towards the detector will increase the fluorescence intensity generated and the amount collected, respectively. This simple system is sufficient when the photodetector is capable of differentiating wavelengths, i.e. a spectrometer. The white light excitation fluorescence (WLEF) fluorometer uses such a setup [6]. This WLEF uses a white light as a source and measures intensity by wavelength using a spectrometer [6]. This more general sensor has poor sensitivity and can be improved upon by introducing light filters and wavelength specific sources such as LEDs and lasers [6]. A fluorometer with filters would be less versatile but more effective for specific targets. A light source with a narrow spectrum may not require an excitation filter but would still require an emission filter. The emission filter would be placed in front of the detector and only allow the wavelengths corresponding to the target's fluorescence emission. A typical filtered fluorometer has three filters: an excitation filter, a dichroic mirror, and an emission filter [7]. These filters would be configured in an epi-illuminated microscope configuration as shown in Figure 1.2. The light source passes through the excitation filter, narrowing the spectrum, and is reflected off the dichroic mirror towards the sample [7]. The sample then emits fluorescence which passes through both the dichroic mirror and the emission filter. Finally, the detector receives wavelengths corresponding to the fluorescence and transduces the light intensity to a voltage reading, after amplification [7].

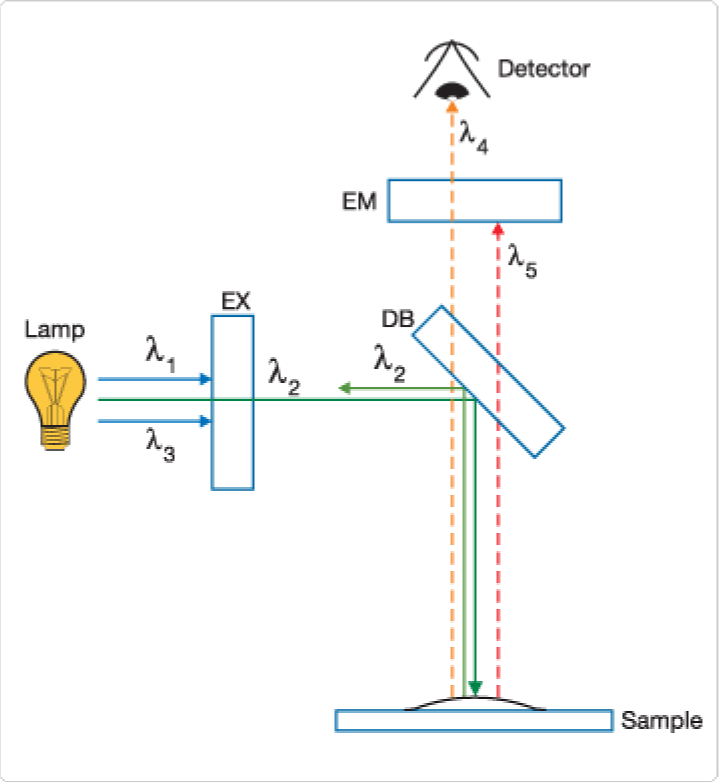

Figure 1.2 Diagram of an epi-illuminated microscope configuration. Reprinted from reference [7].

As a relevant example for this thesis, Figure 1.3 shows the light source or LED spectrum, the spectrum of the excitation filter, the spectra of Rhodamine B dye (absorbance and fluorescence), and the spectrum of the excitation filter. For simplicity, it is assumed that the detector has uniform spectral sensitivity, but that is not usually the case. In this case it is noticeable that the absorbance spectrum's peak (552 nm) is near the fluorescence peak (573 nm) and so the LED chosen was centered further back on the absorption curve (at 521 nm). A shortpass filter was chosen to cut off the tail of this LED spectrum such that it does not overlap with the fluorescence peak. A tight bandpass filter was chosen to isolate the fluorescence peak. Selecting filters is key in isolating the fluorescence from any other sources of light.

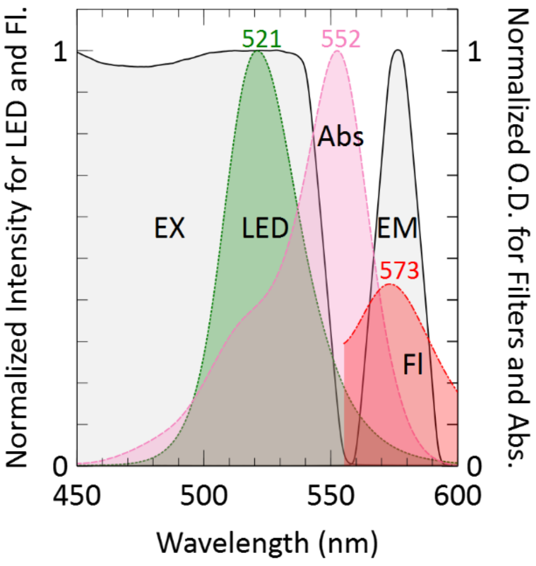

Figure 1.3 Spectra of an LED, Rhodamine absorbance, Abs, and fluorescence, Fl, excitation filter, EX, and emission filter, EM. Reprinted from reference [8].

1.2.3 Lab-on-chip Technology

Lab-on-chip (LOC) sensors have emerged as a promising technology to reduce costs in environmental and diagnostic sampling [9]. By consolidating the chemistry and instrumentation from analytical laboratory techniques onto a network of microfluidic channels, expensive and time-consuming steps can be automated and streamlined. LOC further allows the collection of real-time data in remote settings by non-technical personnel. For example, current colorimetric LOC technologies have led to sensitive platforms for in situ measurement of nitrate/nitrite [2,3], phosphate [4–6], *E. coli* [15], and various heavy metals [8–10]. There are also LOC technologies which use electrochemical techniques, often used to monitor biological cell death and protein/DNA separation/purifications [19] and determining corrosion including corrosion caused by microbiology [20]. These field portable and *in situ* LOC devices are often sensing small volumes of fluid and as such typically use electrochemical detection or optical spectroscopy interrogation. Absorption and fluorescence detection are the mainstay approaches to optical spectroscopy due to their simplicity [21]. While LOC platforms have enabled widespread and low-cost sensing, it would be advantageous for microfluidic devices to perform combined spectroscopic measurements on the same sample under investigation.

1.3 Initial Thesis Target Requirements

Algal blooms occur in both freshwater and marine environments [22]. Algae, a key part of the food chain [22], can proliferate to the point of causing major harm. These harmful algal blooms (HAB)s will reduce the levels of oxygen in the water causing hypoxia in fish and invertebrates [22]. HABs containing diatoms can lead to the death of fish because the shape of diatoms irritates the gills [22]. HABs can also produce toxins, these toxins can kill fish and harm humans who consume seafood or drink contaminated water [22]. The effects of toxins can range from shellfish poisoning to fatal neurotoxins [23]. HABs can grow to be so large that they can be identified from space via satellite [22], [24]–[26].

Most algae use chlorophyll-a, a protein pigment which is fluorescent, [27] to photosynthesize and because of this chlorophyll-a concentrations can be used to correlate algae biomass. Therefore, chlorophyll-a can be used as an indication of a HAB by observing for a threshold density starting at 10^4 cells per milliliter [22]. To some extent, identification, and classification of the HAB is also possible using the fluorescence of pigments. Cyanobacteria have a protein pigment phycocyanin in fresh waters or phycoerythrin in marine waters, which is a good indicator because only a few classes of algae have this protein (Rhodophyceae and Cryptophyceae being the only other two) [27]. HABs caused by cyanobacteria (CyanoHABs) are often the toxic variety as many cyanobacteria will produce toxic secondary metabolites [28], [29]. Microbes will not have a fixed pigment protein content even within the same species. It is beneficial to use a fluorescent dye like Rhodamine instead when calibration as the dye concentration is more easily known.

Oils spills like the Deepwater Horizon Gulf of Mexico oil spill can have serious effects on the environment. Oils spills in marine environments cause damage to fish and other aquatic animals, degrade oceans and coastal habitats and can bring about human harm [30, p. 1]. The first step in an oil spill response would be to detect where the oil is. In response to the Deepwater Horizon incident various commercial sensors including the Turner Design Cyclops were deployed because fluorometers can detect crude and fine oils [31]. It is beneficial to send AUVs with mounted fluorometer as they can navigate underwater and detect subsurface oil plumbs. Often the fluorescent dye Rhodamine WT will be used to simulate an oil spill in the environment by doping a body of water with the dye instead of oil as it is a non-toxic tracer alternative [32]. As an example, a cyclops 7 which has a 0.01 ppb limit of detection for Rhodamine was mounted to an AUV and piloted through such a plumb, detecting sub ppb Rhodamine [32].

The thesis will focus mainly on Rhodamine because Rhodamine is stable and can be used for inter-comparisons more easily than pigments, oils or other complex chemistries. However, when considering HABs it is chlorophyll-a, phycocyanin and phycoerythrin that are the fluorescent pigment proteins of interest. The developed sensor must be able to detect sub ppb Rhodamine, as this is what has been seen in past tracer experiments and is what is capable of current commercial products. In a design where possible reagent waste is of concern a fluid consumption should be kept to a minimum, ideally sub 100 µL as smaller fluid volumes lead to longer deployments. Low power consumption will also lead to longer deployments and so a sub watt power draw is ideal. Given advantages of LOC the design should be easily integrable to LOC automation. The optics in the design should be decoupled from the sample chamber as with LOC designs it is advantageous to have the microfluidic chip decoupled. This modular decoupling allows the chip to be replaced without having to replace optics.

1.4 Thesis Results

1.4.1 Peer-Reviewed Journal Articles

1 **Joshua J Creelman**, Edward A Luy, Gabryelle C H Beland, Colin Sonnichsen, Vincent J Sieben, "Simultaneous Absorbance and Fluorescence Measurements Using an Inlaid Microfluidic Approach", *Sensors*, vol. 21(18), 2021. DOI: 10.3390/s21186250

2 Edward Arthur Luy, Sean Christopher Morgan, **Joshua J Creelman**, Benjamin J Murphy, and Vincent Joseph Sieben. Inlaid microfluidic optics: absorbance cells in clear devices applied to nitrite and phosphate detection. *Journal of Micromechanics and Microengineering*, 30(9):15, 2020. DOI: 10.1088/1361-6439/ab9202

1.4.2 Manuscripts in Progress

1 **Joshua J. Creelman**, Allison Chua, Kyle Park, Teala Chambers, Jack Tsao, Piotr Kawalec, Aaron MacNeil, Doug Wallace and Vincent J. Sieben, "In-Situ Low-Cost Lock-In Fluorometer Applied to the Gulf of Saint Lawrence Rhodamine Tracer Experiment"

1.4.3 Peer-Reviewed Conference Proceedings

1 **Joshua Creelman**, Gabryelle Beland, Benjamin Murphy, Mahtab Tavasoli, James Dean-Moore, Arnold Furlong, Julie LaRoche, Robert Beiko and Vincent Sieben. "HAB Hunter:

progress toward an in situ Lab-on-Chip eDNA sensor." Accepted to Proceedings of the Canadian Society for Mechanical Engineering (CSME) International Congress 2020 (Charlottetown, PE); COVID-19 postponement to summer 2021.

2 Benjamin Murphy, Sean Morgan, Edward Luy, **Josh Creelman** and Vincent Sieben. "Lab-on-a-chip Sensor of In Situ Nutrient Monitoring." OCEANS 2019, (pp. 1 – 7). Seattle, USA: The IEEE Oceanic Engineering Society. October 27-31, 2019.

1.4.4 Patent Applications

1 Microfluidic sampler for selective capturing of environmental DNA with integral optical spectroscopy. US Application No. 63_075548. Inventors: **Josh Creelman**, Edward Luy, Sean Morgan, Gabyrelle Belland, et al., and Vincent Sieben.

CHAPTER 2 NOVEL INLAID MICROFLUIDIC FLUORESCENCE CELL

My contributions to microfluidic projects resulted in two published articles during my thesis research. The first of these publications was to realize a microfluidic nitrite sensor based on a novel fabrication approach, called “inlaid microfluidics”. The approach was initially developed by Sean Morgan and Eddy Luy for performing absorbance spectroscopy [33]. The second of these publications was centrally my work on using the inlaid technique for performing fluorescence spectroscopy on-chip. The requirement was to realize a microfluidic fluorescence sensor that targeted microalgae pigments, Chlorophyl-a, phycocyanin, and phycoerythrin for eventual inclusion in an environmental DNA (eDNA) sampler. The modified version of this inlaid chip for fluorescence was conceptualized by Gabryelle Béland (summer intern), Eddy Luy (MASc student) and myself, while the fabrication of the chip was conducted by Gabryelle, Eddy and Sean. The experimental work, chemistry and testing was done by myself and Eddy.

2.1 Literature Review

Measuring both fluorescence and absorbance simultaneously covers a wide range of potential applications. For example, the Cyclops-7F commercial fluorometer from Turner can measure various target substances like chromophoric dissolved organic matter (CDOM), protein pigments in algae, fluorescent dyes, oils, etc. Fluorometers simply change the filter set and excitation source to match the target substance’s absorbance and fluorescence spectra. Fluorometers are also capable of measuring substances lacking native fluorescence, like real-time PCR (RT-PCR) devices, provided reagents and automated protocols are integrated with the optical technique. Such devices use fluorophores which bind to DNA and therefore fluorescence can be used to quantify the DNA. The work of Preston et al. demonstrates the utility of microfluidics on an *in situ* quantitative PCR (qPCR) platform [34]; where, portable or *in situ* versions of these devices aim to minimize reagent consumption and sample waste. Fluorescence is also used for taxonomic discrimination of phytoplankton [35]. The work of MacIntyre et al. involves detection of HAB forming organisms, both quantifying them [36] and differentiating between viable and unviable cells [37]. However, it is notable that fluorescent pigment protein content can vary cell-to-cell and species-to-species [38], so it is advantageous to have a multiparameter analysis when evaluating environmental samples. Dissolved organic matter (DOM) also plays a role in HAB formation [39]. There are several studies of CDOM which require both absorbance and fluorescence measurements, specifically when determining seasonal changes in the optical properties [36–38]. Algae fluorescent measurements are influenced by CDOM as they can share an overlap in fluorescence spectra [43]. Therefore, simultaneous detection of fluorescence and absorbance better contextualizes the sample under investigation than a single measurement, producing more accurate differentiation of chromophores and fluorophores than either measurement alone.

There have been several reports of microfluidic sensors with the ability to simultaneously detect fluorescence and absorbance signals [21–23]. Recent advances have demonstrated the ability to distinguish multiple analytes through simultaneous absorption and fluorescence [44] or couple scattering, fluorescence and absorption into a single device [45]. Simultaneous fluorescence and absorbance microfluidic measurements of droplets have also been shown to be able to detect pH gradients of 3.9–8 in real-time with a fluorescence detection limit of 400 nM fluorescein in water [46]. Yang et al. accomplished this by using a laser coupled to a microfluidic chip via waveguides for measuring picolitre volumes in a 10 mm long optical cell; the fluorescence was measured from the side of the same optical cell, with a cross-section of 35 × 26 μm [46]. Fibre optics and waveguides have been a robust tool for guiding light to interrogate fluids since the early

1990s [47]. However, due to the nature of *in situ* instruments, shock and vibration can lead to physical misalignment that is often addressed by using adhesives and epoxy bonding of the fibre to the waveguide/carrier. The main challenge with adhesives arises if the chip must be replaced or serviced, and when packaging the overall instrument to fit into a submersible canister, where the minimum bend radius must be respected. Another important difficulty for realizing simultaneous optical measurements lies in creating a long-pathlength absorption cell for low analyte concentrations.

For sensitive measurements, effective path lengths of 10–100 mm are typical for absorbance cells, such as the work of Floquet et al. [48]. On bench, Floquet et al. demonstrated absorbance cell path lengths that ranged from 25–100 mm for nanomolar detection of iron and manganese, and Milani et al. deployed these chips in natural waters based on a 100 mm flow cell [49]. Additionally, these pathlengths allow for nanomolar concentrations of key limiting nutrients nitrate and phosphate [3,27,28]. Cavity enhancement is a proven solution to decrease physical path lengths down to 50 μm with reflective surfaces while maintaining absorbance measurements in the micromolar range [52]. Through cavity-enhanced absorption spectroscopy (CEAS), the light from the source bounces back-and-forth through the droplet sample to enhance the path length by a factor of 28 [52], which yielded an effective pathlength of 1.4 mm. Rushworth et al. used thymol blue indicator dye in a range of 50–2000 μM, measured using CEAS with a 1s integration time [52]. The authors noted that reliably placing and aligning mirrors in such a microfluidic cell for CEAS-based approaches can be challenging. Optical fibres are another solution for increased sensitivity in absorption experiments, through improved coupling of light into and out of the sample area [21]. However optical fibres may introduce complexities when mated with a microfluidic channel, often relying on UV-curable or time-set epoxies that can hinder scaled manufacturability, as well as having minimum bend radii that can restrict miniaturization efforts. It is, therefore, ideal to have more optical elements integrated on-chip when robustness and field portability are eventual requirements.

2.2 Design

Here I introduce a novel inlaid optical cell for measuring both absorbance and fluorescence simultaneously on-chip, without the use of fibers or glue. The basic design of the optical channel in the microfluidic chip follows what our lab has done in the past, a straight inlaid channel with embedded microprisms on either end, capable of absorbance measurements. Here a long path length is necessary for nanomolar concentrations. What makes this chip different was the addition of what we called a fluorescent well, as shown in Figure 2.1. This well is an area within the channel that has been widened to permit fluorescence emission and acts as a point for fluorescence measurement.

Microfluidic chips that we have designed in the past use clear and opaque poly(methyl methacrylate) (PMMA) to create optical paths and selectively block light. This is typically done by having the absorbance path encased in the opaque material and having clear windows at each end of the path. In the fluorescence design there is a third window between these other windows, it resides above the well so that fluorescence can escape the chip and be measured. As shown in Figure 2.1 (a), there are three total windows which are labeled, the first — the excitation window — the window which allows light into the system from the light source, the second and middle-most window — the fluorescence window — the window which allows fluorescence from the well out of the chip to be measured and the last window — the absorbance window — which allows attenuated light out of the chip to be measured. In Figure 2.1 (b) the optical elements and fluid channels can be seen clearly, along with the microprisms at the two ends. The absorbance measurement is made by directing light with the prisms across a long narrow microchannel, while the fluorescence measurement does not use a prism as the light is isotropic when generated. Figure 2.1 (b) also shows an “air channel” that spans through an opaque portion of the chip. The purpose of the air channel is to provide physical space to separate the LED, photodiode, and EM/EX filters above the chip. The two EM and EX filters are also shown, one residing over the excitation window and the other over the fluorescence window.

In Figure 2.1 (c) the fluidic schematic is presented showing the path the fluid sample takes, from inlet to outlet. First, a sample is pumped into the system to perform simultaneous measurements of fluorescence and absorbance. The LED light source then sends light through the excitation filter, narrowing the spectrum of the excitation light. The light then passes through the excitation window, where some of the light will be redirected down the channel by the first embedded microprism. This light passes through the air channel, across the fluorescence well, and through the absorption channel. A portion of the fluorescence generated in the well will escape through the fluorescence window. The fluorescence will pass through the emission filter and reach a mini spectrometer. The light originating from the LED which continues down the absorption channel will become attenuated and eventually reach the second microprism which will direct this attenuated light out of the chip through the absorption window and to a second mini spectrometer. At this point the two simultaneous measurements have been recorded and a new sample can be injected, which will also push out the previous sample. This system was determined to be capable of detecting nanomolar limits of detection for both absorbance and fluorescence measurements, which is further discussed later in this chapter.

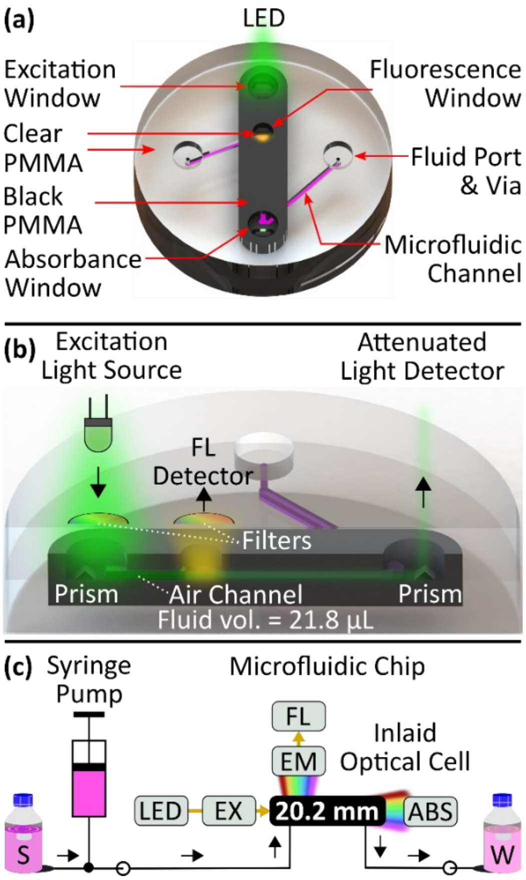

Figure 2.1: Novel Inlaid Cell. (a) A top-down view of a 3D rendering of the microfluidic chip with labelled features. The three windows, the excitation, fluorescence, and absorbance windows, can be seen as clear PMMA encapsulated by opaque PMMA. At the excitation window the green light can be seen entering the chip. At the fluorescence window a yellow fluorescence can be seen exiting the chip. At the absorbance window, attenuated green light can be seen leaving the chip. The fluid ports labelled are used to connected to tubing, allowing samples to be pumped into the chip. (b) A cross-sectional view of a 3D rending of the microfluidic chip with labelled features. The embedded black PMMA is encased in clear PMMA which blocks extraneous light with optical windows for the excitation light to enter, the fluorescence to exit and the attenuated light to exit. The optical path has a total sample volume of 21.8µL. A cone of light can be seen leaving the LED, notably this light is a graphical representation and does not accurately display the radiation pattern of the LED but is there to convey the general path that the light takes. (c) A fluid schematic of the system. This schematic shows how a single sample enters the chip; this schematic does not include the selector value for multiple samples. This schematic presents the characterizing apparatus for validation of the microfluidic cell using fluorescent dye Rhodamine B. The light source (LED) emits light through the excitation filter (EX), the fluorescence (FL) generated passes through the emission filter (EM) where it is measured by a mini spectrometer. The attenuated light (ABS) is also measured by a mini spectrometer. The filters are implemented to prevent spectral overlap of the LED and fluorescence, along with isolating the fluorescence spectra desired in the event other fluorescent material is excited in the sample. Reprinted from reference [8].

2.3 Materials and Methods

2.3.1 Microfluidic Chip

The fabrication of the microfluidic chip involves the process of inlaying opaque PMMA into clear PMMA, this process was developed by Sean Morgan and Eddy Luy, based on a modification of a bonding method described in Ogilvie *et al*. [53]. Gabryelle Beland and Sean Morgan were the ones to fabricate the microfluidic chip. The black oblong inserts were cut from a sheet of black extruded PMMA (9M001, Acrylite, Sanford, ME, USA) using an Epilog Mini24 (Epilog, Golden, CO, USA). One of the inserts had three holes milled into it. These holes would later serve as the windows into the device. The two holes at the ends were each 6 mm in diameter and the middlemost hole 4 mm in diameter. These inserts are bonded into place in clear PMMA which has been milled to hold the inserts such that they have a uniformed finish as shown in Figure 2.2 (a). The milled features in the clear PMMA matched the dimensions of the black inserts with an additional 25 µm as a tolerance such that the black inserts would fit into the clear PMMA easily but still taut. In the case of the insert with three holes, the clear PMMA had three pillars corresponding to the holes. Prior to bonding each piece required a pre-treatment, this pre-treatment involved sanding each rough edge with a fine-grit paper and light scrubbing. A toothbrush was used to clean the cavities, and they were rinsed using Milli-Q. To dry the pieces, compressed air and IPA were used to blast the surfaces. The bonding process involves treating the PMMA pieces with chloroform (C607-4). The chloroform was preheated to 30 °C in a petri-dish. The pieces were mounted 2 mm above chloroform for 45 seconds such that the chloroform-vapor softens the PMMA. The pieces are then pressed together by hand and inserted into a LPKF MutliPress II machine to undergo extreme pressure and temperature to permanently bind the pieces. The pressure used was 625 N/cm^2 and the temperature was 115 °C such that the glass transition temperature of PMMA is approach as described by Becker and Gärtner in 2000 [54], [55]. The inlay was kept under pressure and temperature for 2.5 hours. After bonding, the pieces often had minor protrusions from the inserts that would prohibit further processing. Therefore, the inlaid PMMA sheet is milled down to be uniform thickness by milling down the entire sheet by 200 µm. The results of the inlaying process can be shown in Figure 2.2 (b). Once opaque PMMA has been inlaid into clear PMMA, the channels, vias, prisms and syringe ports are milled into the hybrid sheets of PMMA. The channel dimensions for this design had a depth and width of 1 mm. The absorbance cell is created using a "z-shape" design, typical for light absorbance measurements [8], [33], [55]. The total length of the optical propagation, or the pathlength, in the absorption channel is 20.2 mm. A well was milled underneath the middle window. At the end windows prisms are milled, inspired by the work of Grumann et al. [56]. The prisms are made by using a tapered drill bit, where the tip of the bit is 45° from the center. To realize the prism, a small straight line is milled to achieve a straight edge that forms a 45° prism; however, the ends of the prism are conical from the rotating drill bit. There is an air channel between the excitation window and the fluorescence window. This air channel was milled into the chip to create physical space between the off-chip LED and photodiode, such that light would be able to travel through the black PMMA without propagating in the sample fluid. This was done instead of a fluid channel to minimize optical losses before the well caused by absorption that a fluid channel would have. This air channel was 2 mm wide, 1 mm deep and 7.7 mm long. In addition to the functional features, alignment holes are cut such that when bonding pins hold the chip halves in alignment. After all the features were milled, the two halves of the inlayed chip are then cut from the sheet and bonded together using a similar method of bonding the inlaid components. The only difference between the inlayed bonding and this bonding is that the temperature was reduced to 85 °C to prevent channel distortion. Photos of the final chip are shown in Figure 2.2 (c). The figure also gives the approximate time it took at each step, the overall process being approximately 7 to 8 hours.

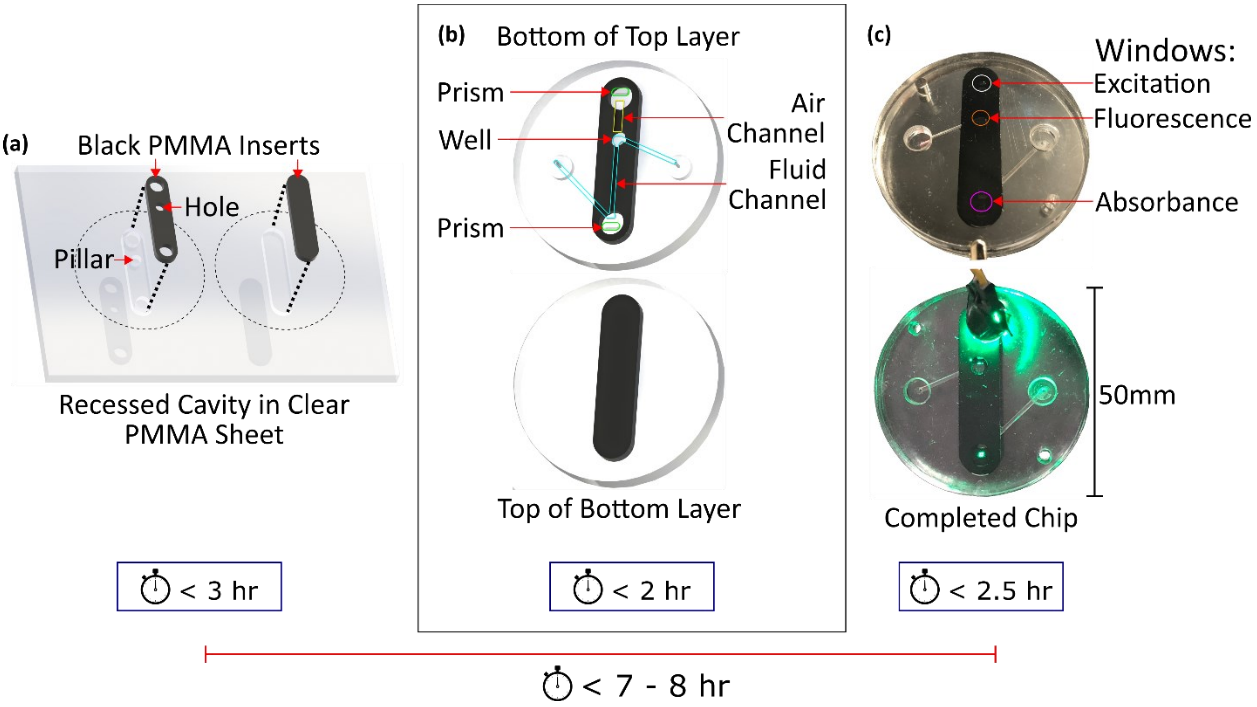

Figure 2.2: Inlaid Fabrication. (a) The first step in the bonding process. The black PMMA oblong pieces are inserted into their respective cavities of the clear PMMA. It can be seen that there are pillars in the clear PMMA cavity that match the black PMMA's holes. (b) The second step involves milling out the features of the chip, the channels, prisms and well. Notably the channel crosses the clear to black interface for integral optical windows in an opaque cell. Each chip half is then cut from the sheet. (c) The final step is to bond each chip half together. In the top the completed chip can be seen, and the windows labelled. In the bottom the LED is used to demonstrate that the prisms are directing the LED's light though the channel, as the light can be seen exiting the chip via the absorbance window. Reprinted from reference [8].

2.3.2 Optical Assembly

The optical assembly was mounted above the chip. The assembly consisted of a 3D print which held: an LED, an emission filter, excitation filter and 2 SMA-905 optical fiber couplers. The optical fibers each connected to a mini spectrometer. The print held the filters above their respective windows, the LED above the excitation filter and the optical fibers above the other two remaining windows. The design of this print allowed up to two LEDs, one 3 mm and one 5 mm. An isometric view of the print is shown in Figure 2.3 (a) and a top-down view in Figure 2.3 (b). A cross-sectional view of the print revealing the filter trays as shown in Figure 2.3 (c).

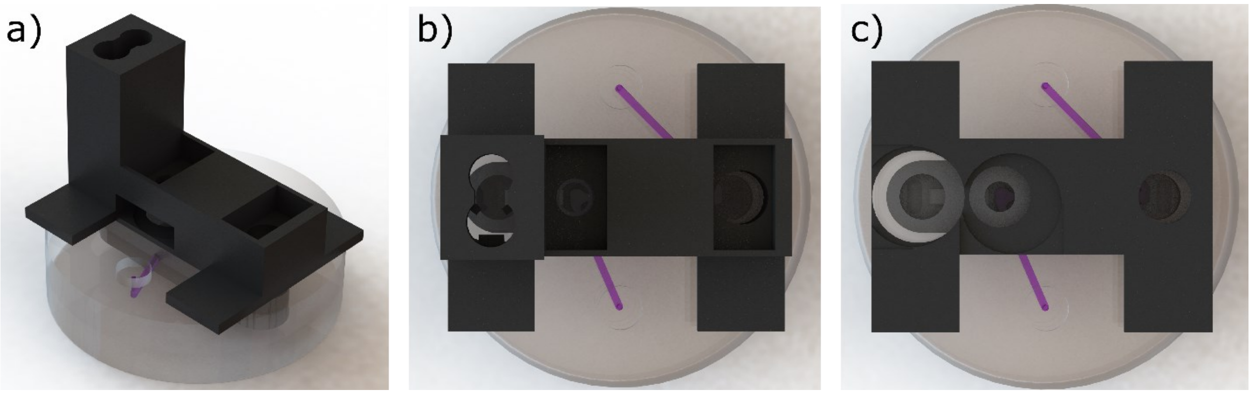

Figure 2.3: Optical Stack for Inlaid Chip. (a) An isometric view of a 3D rendering of the optical mount above the chip. (b) A top-down view of a 3D rendering of the optical mount above the chip. This shows the alignment of the optical assembly to the chip. The LED and spectrometer used for absorbance are not centered around the windows but rather the prisms, whereas the fluorescence well has the spectrometer mounted centering above it. (c) A top-down cross-sectional view of a 3D rendering of the optical mount above the chip. Here the filter trays are easily visible. Due to space constraints the filters were not centered with the windows, however the performance is unaffected.

2.3.3 Chemistry

To calibrate the optics of the chip the fluorescent dye Rhodamine B was used. A 2.5 g/L stock solution of Rhodamine B was prepared by diluting 0.5 g of Rhodamine B ($C_{28}H_{31}ClN_2O_3$, ≥95%, R6626, CAS 81-88-9, Lot # SHBL5990, Sigma-Aldrich, Oakville, Ontario, Canada) with Milli-Q water to a total volume of 200 mL. A series of standards were produced from highest concentration to lowest through serial dilution. The standards produced were: 0.1, 0.25, 0.5, 1, 2, 5 and 10 µM.

2.3.4 Experimental Setup

The chip and optical assembly were encased in a black plastic box with electrical tape covering the tinted box. This was done to block any stray background rays from entering the system. Holes were made in the side of the box to feed fiber and electrical cables and fluid tubes which were necessary to operate the device.

Injection of fluids through the microfluidic chip was achieved using several off-the-shelf components. A Vici Cheminert C65Z 10-port selector valve (Valco Instruments Co. Inc., Houston, TX, USA) was used to pull from different samples without cross-contamination. FEP tubing connected each sample to a respective intake port on the valve. The output connected to the intake of an off-the-shelf Cavro XC syringe pump (Tecan Systems, San Jose, CA, USA) which was used to drive fluid flow. The output of the syringe pump was directly connected to the input of the microfluidic chip. Fluids were pumped through the chip at a consistent flow rate of 1.5 mL/min, and flow was paused during each sample/blank measurement.

As shown in Figure 2.1 (c), the total amount of light absorbed by the fluid in the 20.2 mm long optical path is measured using the first spectrometer (USB2000+, Ocean Optics). Similarly, a portion of the light emitted by the fluid through fluorescence is measured simultaneously using the second spectrometer (Flame, Ocean Optics). The LED used for excitation of Rhodamine B had a centre wavelength of 521 nm (Cree C503B-GANCB0F0791-ND, measured FWHM ≈ 35 nm). The excitation filter used was a shortpass filter 550 nm cut off (Edmund Optics, 84–695) and the emission filter used was a band pass with a centre of 578 nm with 16 nm width (Edmund Optics, 87–738). The excitation filter had an optical density of 4 whereas the emission filter had an optical density of 6.

The mini spectrometers were connected using USB to a computer and used Ocean Optics software. The integration time for the absorbance spectrometer was 10 ms whereas the fluorescence spectrometer used 10 s. The fluorescence signal was significantly smaller than the absorbance signal therefore requiring a much longer integration time. For each sample three measurements were taking and averaged together for a single data point, in addition to this averaging three data points were collected per sample, totalling nine individual measurements per sample.

2.3.5 Analytics

Prior to sample acquisition the Ocean Optics software took a measurement with both spectrometers to use as a dark reference; this was done with the LED off. This dark reference was subtracted by all subsequent measurements via the Ocean Optics software. The procedure for acquiring sample measurements included measuring a blank sample before each standard. A blank sample is just milli-Q without any Rhodamine B. These blank samples help in quantifying any carryover between samples and gives a reference spectrum for subsequent calculation for both absorbance and fluorescence. For absorbance, A(λ), the Beer-Lambert law is used at each wavelength, λ. This is done by using equation 2.1, where $S_a(\lambda)$ is the counts measured sample from the absorption channel and $B_a(\lambda)$ is the blank counts measured from the absorption channel.

$$A(\lambda) = -\log\left(\frac{S_a(\lambda)}{B_a(\lambda)}\right) \tag{2.1}$$

Fluorescence, F(λ), at each wavelength is calculated by using a differential between the fluorescence sample counts $S_f(\lambda)$ and the fluorescence blank counts $B_f(\lambda)$. This can be seen in equation 2.2.

$$F(\lambda) = S_f(\lambda) - B_f(\lambda) \qquad 2.2$$

The units of counts are an arbitrary light intensity unit provided by the Ocean Optics software. The data was processed by a LabVIEW program. This program used equations 2.1 and 2.2 to generate processed data for each blank and sample pair. This processed data is discussed in the next section of this chapter.

2.4 Results and Discussion

2.4.1 Calibration

The results of the Rhodamine B calibration are shown in Figure 2.4. In Figure 2.4 (a) the absorbance vs. wavelength results are plotted. There are 7 differently coloured curves, each corresponding to a different concentration as indicated by the legend. The absorbance trend is as expected by the Beer-Lambert law, higher concentrations absorb more incident light. Another observation is a sharp drop in the absorbance approximately at 550 nm, however this is explained by the shortpass filter used which had a cut-off at this wavelength. Similarly, in Figure 2.4 (b), the fluorescence vs. wavelength of 7 differently coloured curves show the fluorescence results. As expected, the higher the concentration of Rhodamine, the more fluorescence produced. The spectrum captured is between the cut-off points of the optical bandpass filter used.

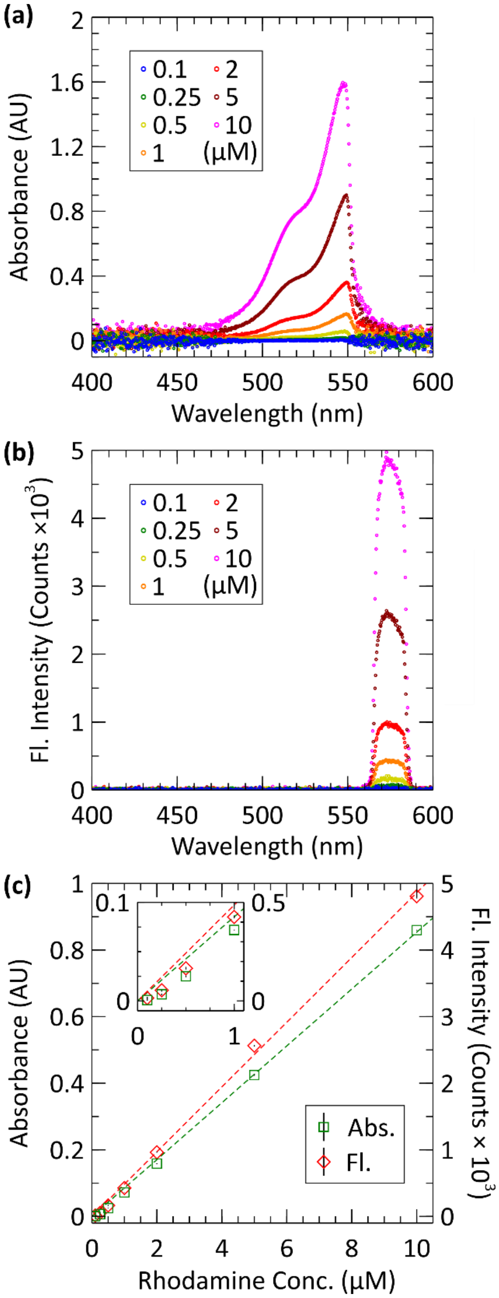

Figure 2.4: Fluorescence data from Inlaid chip. (a) The processed absorbance vs. wavelength measurements from the calibration of Rhodamine B 0.1 to 10 µM. Each series shown is the average of the triplicate taken. (b) The processed fluorescence vs. wavelength measurements from the calibration of Rhodamine B 0.1 to 10 µM. Each series shown is the average of the triplicate taken. (c) Both absorbance and fluorescence vs. Rhodamine B concentration. The data points for absorbance were the average for absorbance from wavelengths 525 to 530 nm. The data points for fluorescence were the average fluorescence from wavelengths 570 to 575 nm. The inset graph shows data for low concentrations of 0.1 to 1 µM. Reprinted from reference [8].

Figure 2.4 (c) is the results of processing the data from Figure 2.4 (a) and (b). In this figure, the calibration curves are presented: absorbance vs. concentration, and fluorescence vs. concentration. The green series represents the absorbance and the red series represents the fluorescence. The data was produced by taking the average absorbance/fluorescence over a know range of wavelengths. For absorbance the average was taken over the wavelength range 525 to 530 nm and for fluorescence 570 to 575 nm. For each set of data, linear trendlines were applied. The line of best fit for absorbance vs concentration was calculated such that A = (0.0854 ± 0.0002)C. Using A = 0.08535C, a root-mean-squared-error (RMSE) of 0.0126 and R^2 value of 0.998 was found. Similarly, a line of best-fit between fluorescence and concentration was calculated such that F = (486 ± 11)C. Using F = 486C a RMSE of 77.5 and R^2 value of 0.998 was found. This demonstrates that, in either case, a linear model accurately describes the data.

2.4.2 Attenuation Coefficient

The attenuation coefficient, ϵ, of a species can be determined from the slope of its absorbance vs. concentration curve. The attenuation coefficient, ϵ, is a function of wavelength, λ, and is unique to the measured species:

$$\epsilon = \frac{M(\lambda)}{l} \tag{2.3}$$

where the slope of the light absorbance calibration curve, M, is divided by the optical path length, l. M was determined at each wavelength by using the data shown in Figure 2.4 (a). Due to the use of the short-pass excitation filter, data obtained for wavelengths above ~550 nm are artificially near zero from the optical filter blocking those wavelengths. Similarly, the transmission spectra of the light source are limited to a 15 nm FWHM centred at 521 nm. The light source emits roughly 1% of its maximum at 470 nm. Consequently, the attenuation coefficient of Rhodamine B was determined for a wavelength range of 470 nm to 550 nm—this is shown in Figure 2.5. Equation 2.3 was used to calculate each attenuation coefficient using the 20.2 mm optical path length of the fluid. The data in Figure 2.5 show a maximum attenuation coefficient of 80,774 $(\mu M\cdot cm)^{-1}$ at λ = 549 nm. As a comparison, the measured values of a range of Rhodamine dyes by Yuan et al. showed the maximum molar extinction coefficient to be in the range of 80,000–120,000 $(\mu M\cdot cm)^{-1}$ [57]. Therefore, our measured values are like those reported in the literature. It is noteworthy, that the peak extinction coefficient may occur at slightly different wavelengths due to solvato-chromic effects. For example, a peak wavelength of λ = 545 nm has been reported for Rhodamine B with methanol as the solvent [58], whereas we observe the peak in Milli-Q water at λ = 549 nm. Given that our samples are highly filtered, the attenuation coefficient and the molar extinction coefficients should be comparable as there are minimal scattering loses in the channel.

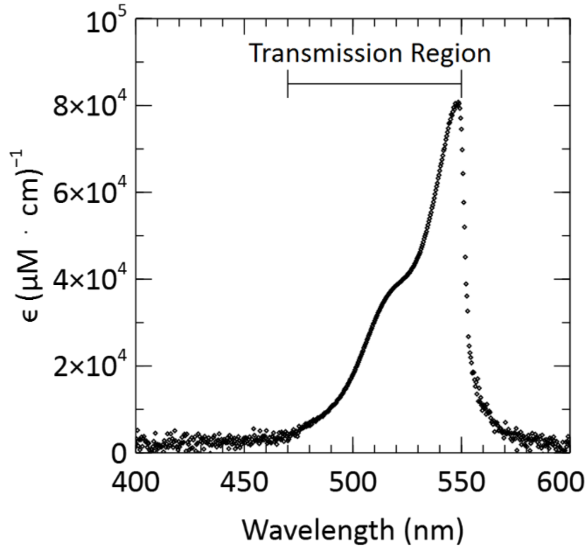

Figure 2.5: Attenuation coefficient, ϵ, of Rhodamine B in Milli-Q water. The drop at wavelengths greater than ~550 nm is due to the cut-off of the excitation filter. Reprinted from reference [8].

2.4.3 Limit of Detection

The limit of detection can be defined as three times the standard deviation using the triple-sigma method [27,28,43,44]. The LOD for absorbance was calculated using the blanks preceding the 0.1 μM measurements, which ensured minimum crosstalk for evaluating the LOD. First each blank measurement was averaged over a 5 nm window centred at 527 nm as this is what was used when determining absorbance for the sample measurements. The data in the blank measurements ranged from 48 k – 50 k counts, with a standard deviation of 666 counts. This results in 0.006 AU against the average blank; therefore, the triple sigma method yields 0.018 AU and when using the line of best fit from our calibration curve, the absorbance LOD equates to 208 nM Rhodamine B. The LOD for fluorescence was similarly calculated using the same blanks but measured from the fluorescence window. The intensities were averaged between 570 – 575 nm. The data in the blank measurements ranged from 24 – 40 intensity counts, with a standard deviation of 7.6 counts, therefore the triple-sigma method yielded 23 counts of intensity. Using the line of best fit from the fluorescence calibration curve, the fluorescence LOD equates to 47 nM Rhodamine B. For a point of reference, the Turner Cyclops-7F is a commercially available marine fluorometer and states a 0.01 ppb Rhodamine (0.02 nM) is the LOD. However, this sensor is not a microfluidic device and the volume of interrogation from the LED beam into the water is orders of magnitude higher than the 20 μL of volume contained in our fluorescence chamber. The LOD of fluorescence is insufficient compared to the thesis requirement of sub 1 ppb (1.8 nM) and an improvement of at least x26 is required. Another target for this thesis is to measure chlorophyll-a. To measure a different fluorescence species only the filters and LED would need to be changed.

To get a relative benchmark for how Rhodamine compares to chlorophyll, the LODs of the Turner Cyclops 7F can be compared. The LOD of chlorophyll on the Turner Cyclops-7F is 0.03

μg/L compared to the 0.01 ppb Rhodamine. However, the datasheet also claims that more power is required to measure chlorophyll, 240 mW when measuring chlorophyll compared to 175 mW for Rhodamine. Using a ratio between the power consumptions it can be assumed that 0.007 ppb (0.01 nM) Rhodamine is comparable to measuring 0.03 μg/L chlorophyll. If this is the case, then the LOD of the developed sensor would need an improvement of x4700 to match the commercial sensor's LOD. However the formation of HABs can be considered when chlorophyll reaches 5 μg/L [61] and so detecting below this threshold would be sufficient. Using the linear range of the Cyclops 7 for both Rhodamine 0 – 1000 ppb and chlorophyll 0 – 500 a rough estimate of Rhodamine to chlorophyll can be determined. For 5 μg/L chlorophyll the approximate Rhodamine concentration would be 2.5 ppb (4.4 nM) using the linear range ratio conversion and applying the power ratio subsequently results in 1.8 ppb (3.1 nM), a much easier concentration to detect and only requiring a x15 improvement of the developed sensor.

To achieve a better LOD the use of collimating optics and signal processing such as lock-in amplification can be implemented and would considerably improve the LOD. The use of lenses could greatly increase both the results of the excitation and emission. When considering the LED, it is uncollimated and the number of rays from the LED reaching the fluorescence well could be improved by collimating the light from the LED. Similarly, the fluorescence from the well could be collimated and subsequently focused on the detector. An example of lock-in improving LOD can be seen in the work of Banerjee et al. [62]. Pais et al. showed an LOD of 100 nM using a microfluidic chip measuring fluorescence of Rhodamine 6G [63] which was improved to 10 nM using a lock-in amplification approach by Banerjee et al. [62]. Further chapters of this thesis describe exactly these kinds of improvements that were explored, implemented and field tested.

CHAPTER 3 LOCK-IN AMPLIFIER

This chapter starts with the basics and theory of lock-in amplification. The chapter then describes the MATLAB simulations of lock-in amplification and the application on a microprocessor. Lock-in amplification is not a new signal processing method; however, the MATLAB simulations and microprocessor implementation are my own work.

3.1 Literature Review

Lock-in technology has been advancing for over half a century. Analog lock-in amplification had advanced enough by the mid 1960's such that analog lock-in amplifiers were commercially feasible, but cost as much as a high end oscilloscope and therefore limited to a few undergraduate laboratories [64]. By the late 1960's "do-it-yourself" techniques for simpler analog circuits were possible [65]. By the mid 1970's lock-in amplifiers had become one of the most common and efficient tools in chemical analysis. Subsequent research and development efforts aimed at making lock-in amplifier circuits more cost effective [66]. At this time, simulations of digital lock-in amplifiers were being performed as an alternative to the tuning and adjustments required in a complete analog lock-in [67]. With the rise of microprocessors and the advent of high-precision ADCs and DACs, it was not uncommon to see fully digital lock-in techniques by the early 2000s [68]–[70]. Digital lock-in amplifiers typically are driven at much lower frequencies compared to their analog counter parts, the limiting factors being the ADC sample rates and DAC transition rates. Digital lock-in amplifiers were typically in the 5 to 20 kHz range [71]–[73], whereas analog circuits easily attained MHz frequencies [74]. More recent digital lock-in amplifiers, implemented in FPGAs, can reach several hundred kHz [75].

3.2 Theory

A lock-in amplifier aims to extract the amplitude and phase from an arbitrary signal in relation to a reference waveform; this arbitrary signal is often buried within substantial noise. The reference wave form's signal and phase are known in advance. Figure 3.1 illustrates the lock-in process. To perform lock-in amplification, the received signal is first multiplied by the reference signal. This is done with both an in-phase version of the reference and out-of-phase version of the reference, meaning the reference's phase are 90° apart. The now mixed signals are each fed through a lowpass filter, and then used to obtain the buried signal's amplitude and phase, provided it has a matching frequency to the reference signal.

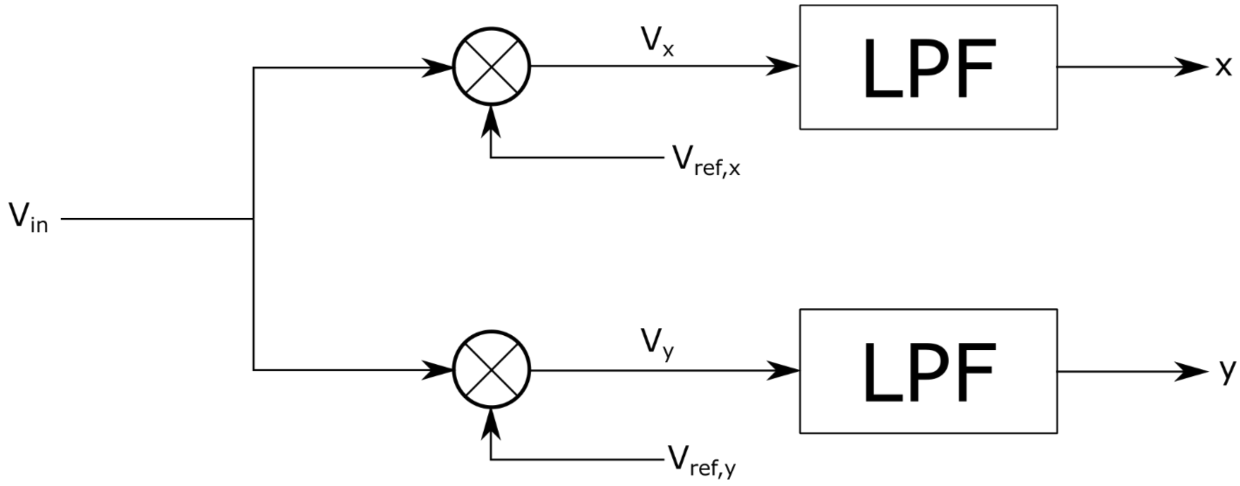

Figure 3.1: Diagram of lock-in amplification. V_{in} is the received signal, contains a signal with known frequency. V_{ref} is the reference signal, having the same frequency as the signal that is targeted for recovery. There is an in phase and out of phase component, the x and y components respectively. V_{in} is mixed with both these reference signals giving V_x and V_y. These two mixed signals are then fed through low pass filters resulting in the X and Y variables.

Mathematically, this lock-in process can be described as follows. To start, the input signal is a sinusoid with amplitude V_{sig}, frequency ω_s and phase shift θ_s in equation 3.1.

$$V_{in} = V_{sig}\sin(\omega_s t + \theta_s) \qquad 3.1$$

This signal is then multiplied by an in-phase reference sinusoid and out-of-phase reference sinusoid. The reference in-phase component $V_{ref,x}$ is a sinusoid with an amplitude V_{ref}, frequency ω_r and phase delay θ_r as seen in equation 3.2. Similarly the out of phase component $V_{ref,y}$ is a cosinusoidal with the same amplitude, frequency and phase delay as seen in equation 3.3.

$$V_{ref,x} = V_{ref} \sin(\omega_r t + \theta_r) \tag{3.2}$$

$$V_{ref,y} = V_{ref} \cos(\omega_r t + \theta_r) \tag{3.3}$$

The resulting multiplied signals can be seen in equation 3.4 and 3.5.

$$V_x = V_{sig} V_{ref} \sin(\omega_s t + \theta_s) \sin(\omega_r t + \theta_r) \tag{3.4}$$

$$V_y = V_{sig} V_{ref} \sin(\omega_s t + \theta_s) \cos(\omega_r t + \theta_r) \tag{3.5}$$

Assuming an ideal square lowpass filter, defined as LPF, we would have a cut-off frequency W, as seen in equation 3.6.

$$LPF = \mathrm{sinc}\,(t) = \frac{\sin(Wt)}{\pi t} \tag{3.6}$$

The lowpass filter would then be applied to each multiplied signal, as shown in equations 3.7 and 3.8.

$$x = V_x * LPF \tag{3.7}$$

$$y = V_y * LPF \tag{3.8}$$

Using trigonometric substitutions in equations 3.4 and 3.5 yield equations 3.9 and 3.10 respectively.

$$V_x = \frac{V_{sig} V_{ref}}{2} \left[\cos\big((\omega_s - \omega_r)t + (\theta_s - \theta_r)\big) - \cos\big((\omega_s + \omega_r)t + (\theta_s + \theta_r)\big) \right] \tag{3.9}$$

$$V_y = \frac{V_{sig}V_{ref}}{2}\left[\sin\left((\omega_s + \omega_r)t + (\theta_s + \theta_r)\right) + \sin\left((\omega_s - \omega_r)t + (\theta_s - \theta_r)\right)\right] \quad 3.10$$

The following substitutions are used for clarity.

$$V_g = \frac{V_{sig}V_{ref}}{2}, \Sigma\omega = \omega_s + \omega_r, \Delta\omega = \omega_s - \omega_r, \Sigma\theta = \theta_s + \theta_r, \Delta\theta = \theta_s - \theta_r$$

The substitutions result in equations 3.9 and 3.10 becoming 3.11 and 3.12, respectively.

$$V_x = V_g[\cos(\Delta\omega t + \Delta\theta) - \cos(\Sigma\omega t + \Sigma\theta)] \quad 3.11$$

$$V_y = V_g[\sin(\Sigma\omega t + \Sigma\theta) + \sin(\Delta\omega t + \Delta\theta)] \quad 3.12$$

Again, using trigonometric identities, equations 3.11 and 3.12 become 3.13 and 3.14 respectively.

$$V_x = V_g[\cos(\Delta\theta)\cos(\Delta\omega t) - \sin(\Delta\theta)\sin(\Delta\omega t) - \cos(\Sigma\theta)\cos(\Sigma\omega t) + \sin(\Sigma\theta)\sin(\Sigma\omega t)] \quad 3.13$$

$$V_y = V_g[\cos(\Delta\theta)\sin(\Delta\omega t) + \sin(\Delta\theta)\cos(\Delta\omega t) + \cos(\Sigma\theta)\sin(\Sigma\omega t) + \sin(\Sigma\theta)\cos(\Sigma\omega t)] \quad 3.14$$

The equations are now easily transformable to the frequency domain. Using a Laplace transform table equations 3.13 and 3.14 become 3.15 and 3.16 respectively.

$$f\{V_x\} = V_g\begin{bmatrix}\cos(\Delta\theta)\,\pi[\delta(\omega - \Delta\omega) + \delta(\omega + \Delta\omega)] - \sin(\Delta\theta)\frac{\pi}{j}[\delta(\omega - \Delta\omega) - \delta(\omega + \Delta\omega)] \\ + \sin(\Sigma\theta)\frac{\pi}{j}[\delta(\omega - \Sigma\omega) - \delta(\omega + \Sigma\omega)] - \cos(\Sigma\theta)\,\pi[\delta(\omega - \Sigma\omega) + \delta(\omega + \Sigma\omega)]\end{bmatrix} 3.15$$

$$f\{V_y\} = V_g\begin{bmatrix}\cos(\Delta\theta)\frac{\pi}{j}[\delta(\omega - \Delta\omega) - \delta(\omega + \Delta\omega)] + \sin(\Delta\theta)\,\pi[\delta(\omega - \Delta\omega) + \delta(\omega + \Delta\omega)] \\ + \cos(\Sigma\theta)\frac{\pi}{j}[\delta(\omega - \Sigma\omega) - \delta(\omega + \Sigma\omega)] + \sin(\Sigma\theta)\,\pi[\delta(\omega - \Sigma\omega) + \delta(\omega + \Sigma\omega)]\end{bmatrix} 3.16$$

Now the multiplied signals can be applied to a filter in the frequency domain, as seen in equations 3.17 and 3.18.

$$f\{x\} = X = f\{LPF\}f\{V_x\} \quad 3.17$$

$$f\{y\} = Y = f\{LPF\}f\{V_y\} \tag{3.18}$$

The ideal low pass filter in the frequency domain being a gain of 1 for frequencies below the cut-off and 0 after, as seen in equation 3.19.

$$f\{LPF\} = \begin{cases} 1, & |\omega| < W \\ 0, & |\omega| > W \end{cases} \tag{3.19}$$

The lowpass filter should be designed to remove the higher frequencies generated by the multiplication, Σω, and extract the lower frequencies generated by the multiplication, Δω, as seen by equation 3.20.

$$\varDelta\omega < W < \varSigma\omega \tag{3.20}$$

The filtered signal will result in the in-phase component x and quadrature component y, as seen in equations 3.21 and 3.22 respectively.

$$x = V_g[\cos(\varDelta\theta)\cos(\varDelta\omega t) - \sin(\varDelta\theta)\sin(\varDelta\omega t)] \tag{3.21}$$

$$y = V_g[\cos(\varDelta\theta)\sin(\varDelta\omega t) + \sin(\varDelta\theta)\cos(\varDelta\omega t)] \tag{3.22}$$

Ideally the reference signal will have the same frequency as the signal such that only a DC component is generated during multiplication, i.e. Δω is zero. This results in a simplification of equations 3.21 and 3.22, being equations 3.23 and 3.24 respectively.

$$x = V_g\cos(\varDelta\theta) \tag{3.23}$$

$$y = V_g\sin(\varDelta\theta) \tag{3.24}$$

Now the original signal can be determined from the x and y components. First by summing the squared components, as seen in equation 3.25, and then finding the root, as shown in equation 3.26, the math simplifies to equation 3.27.

$$x^2 + y^2 = V_g^2 \cos^2(\Delta\theta) + V_g^2 \sin^2(\Delta\theta) \tag{3.25}$$

$$\sqrt{x^2 + y^2} = V_g \tag{3.26}$$

$$V_{sig} = \frac{2}{V_{ref}}\sqrt{x^2 + y^2} \tag{3.27}$$

This provides a simple equation that obtains the original signal's amplitude from the results of the low pass filters. Additionally, the phase difference between the reference and the signal can be determined. To do this the x and y components are divided, as shown in equation 3.28, such that they equate to the tangent of the phase difference, as shown in equation 3.29, which simplifies to the difference in phase equation to the inverse tangent of the ratio between the x and y components as shown in equation 3.30.

$$\frac{y}{x} = \frac{V_g \sin(\Delta\theta)}{V_g \cos(\Delta\theta)} \tag{3.28}$$

$$\frac{y}{x} = \tan(\Delta\theta) \tag{3.29}$$

$$\Delta\theta = \tan^{-1}\left(\frac{y}{x}\right) \tag{3.30}$$

Summarily the important steps in lock-in amplification are listed. First is to have a reference with the same frequency as the measured signal. Next, multiply the input signal by an in-phase reference and out-of-phase reference. Followed by, filtering the multiplied signals with low pass filters to obtain ideally only the DC components. Lastly using equation 3.27 to obtain the original signal's amplitude and equation 3.30 to obtain any phase difference from the reference.

3.3 MATLAB lock-in simulation results

MATLAB is an excellent tool suited for developing signal processing algorithms. Before development of a lock-in amplifier on a microprocessor the proofing was done in MATLAB. The simulated captured signal had a sample frequency of 30 kHz and a frequency of 1 kHz. The array for this signal contained 5 seconds worth of data. The signal had an amplitude of 1 V. The reference signal also had the same properties. The simulated captured signal is given an arbitrary amount of simulated noise and a random phase. The simulated noise tests the lock-in's magnitude extraction abilities, where the random phase tests the lock-in's phase detection ability. The random phase is generated by using MATLABs 'rand' function, which returns a random value between and including 0 and 1. The result of 'rand' is multiplied by two pi and then pi is subtracted from that result; this will result in a phase between negative pi and pi. The random noise is similarly generated by using the same 'rand' function. The noise is generated by creating an array were each entry uses the 'rand' function, subtracted by a half to give it an offset, and multiplied by the desired noise amplitude. This results in a random waveform with a maximum noise at a desired level. One such simulated acquired signal is shown in Figure 3.2 (a), where in this example the desired noise amplitude is 10 V to the simulated 1 V of signal. The simulated acquired signal is then multiplied by both the in-phase and out-of-phase reference signal, producing the two mixed signals. In Figure 3.2 (b) and (c) the mixed signals are shown. The next step is to filter these signals to acquire the components necessary for the lock-in equations. In this MATLAB simulation two paths for filtering were explored; using MATLABs 'lowpass' function and using averaging. When using the function 'lowpass' the parameters used were a cut-off frequency of 100 Hz, Impulse response mode as IIR with a steepness of 0.5. The lowpass function of MATLAB uses a minimum order elliptical filter when given the 'iir' parameter. In Figure 3.2 (d) and (e) the filtered signals are shown. Alternatively, averaging the mixed signals acts like a lowpass filter and so this is also done in parallel. To be explicit, the averaging process implemented was the sum of the array entries of an individual mixed series divided by the number of entries. The signals using the 'lowpass' function still need to be averaged afterwards to obtain a single value for the lock-in equations. The MATLAB script concludes by performing equations 27 and 30 from the previous section. In Figure 3.2 (f), the results can be visualized as the expected signal, filter method result, and average method result.

The MATLAB script developed also performed the FFT at each stage and plotted the results. Looking at Figure 3.3 (a), the simulated signal's frequency domain can be observed. In Figure 3.3 (b) and (c) the frequency domain of the mixed signals can be observed. It is at this point in the lock-in that the acquisition of the main variables for the lock-in equations can be visualized. The results of the time domain multiplication of the reference waveform are shown in the frequency domain. The information required for the lock-in is the delta peaks which have super imposed at the 0 Hz position. This highlights the necessity for a good low pass filter (LPF) to extract only the DC component and reject all other frequencies. In Figure 3.3 (d) and (e) the extracted DC components are shown.

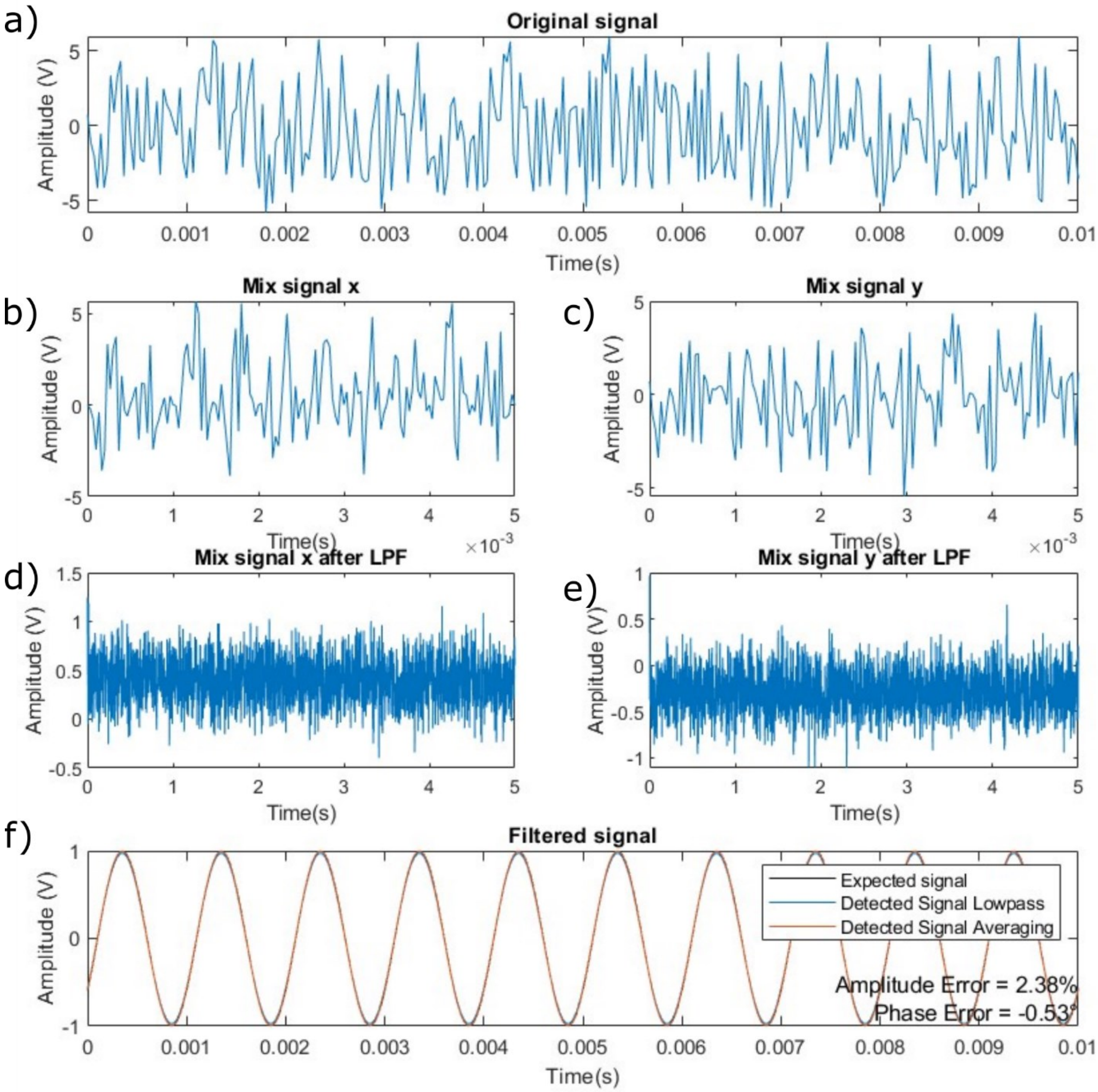

Figure 3.2: MATLAB simulation in the time domain. (a) MATLAB simulated sinusoidal signal of 1V amplitude with white noise of 10V amplitude. (b) Mixed signal of input from part (a) and the in-phase reference signal. (c) Mixed signal of input from part (a) and out-of-phase reference signal. (d) Signal from part (b) after lowpass filter is applied. (e) Signal from part (c) after lowpass filter is applied. (f) Recovered signal and original signal with amplitude and phase error listed.

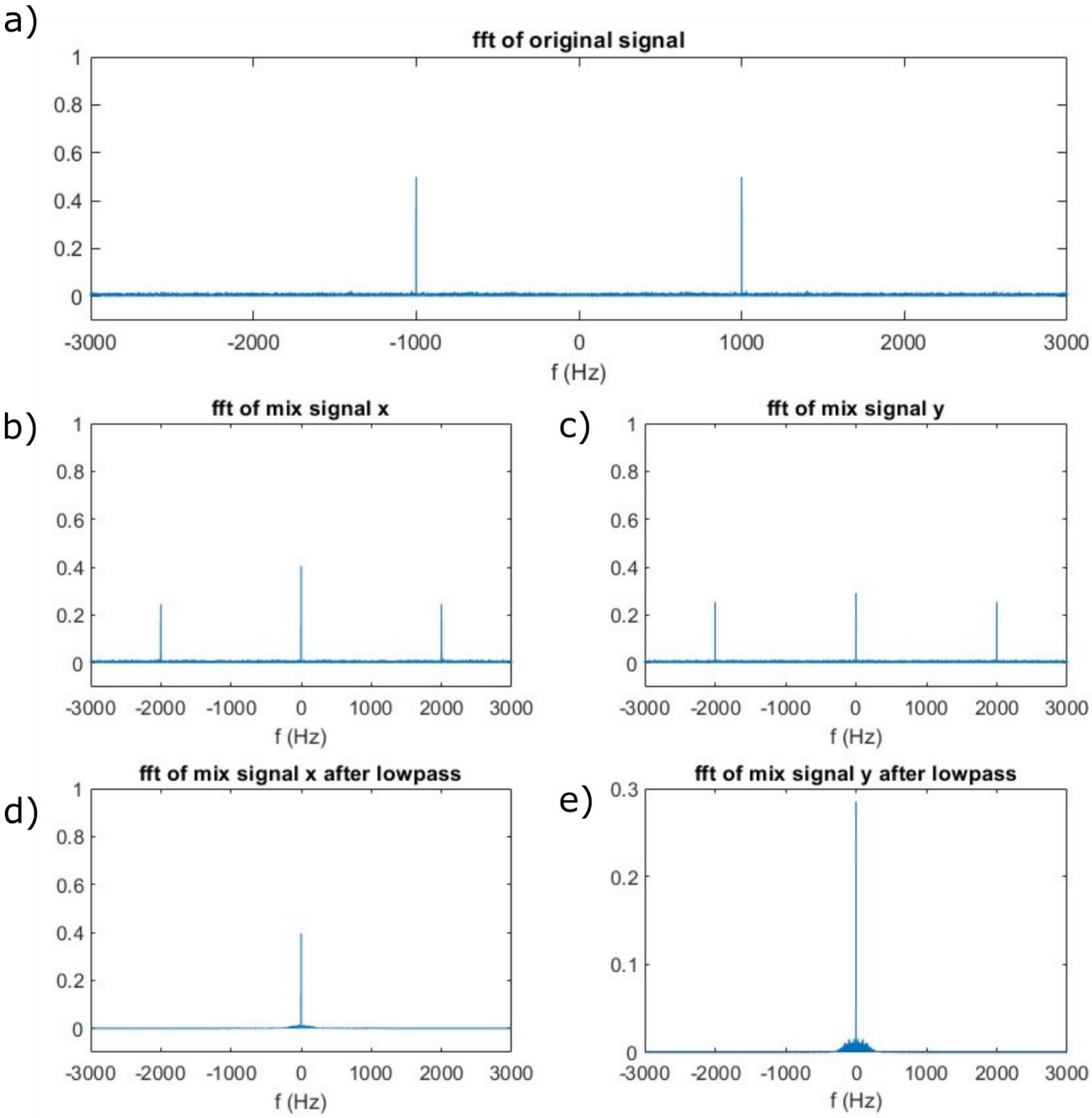

Figure 3.3: MATLAB lock-in simulation in the frequency domain. (a) MATLAB simulation of the FFT of a 1kHz signal in white noise. (b) FFT of the signal in part (a) mixed with the in-phase reference signal. (c) FFT of the signal in part (b) mixed with the out-of-phase reference signal. (d) Signal from part (b) after lowpass filter is applied. (e) Signal from part (c) after lowpass filter is applied.

An error comparison between a lowpass filter and simple averaging was performed. The lowpass used MATLAB’s lowpass function with the following parameters: ‘ImpulseResponse’, ‘iir’, with a ‘Steepness’ of 0.5. The simulation used a waveform with an amplitude of 1 V and a frequency of 1 kHz, which then was given white noise where the amplitude of the noise reached a maximum noise level. The simulation was performed five times per noise level, with noise levels of 1, 10, 100 and 1000. The results of the lock-in filter using each method was compared to the original signal by calculating the percent difference. The results of these simulations are tabulated in Table 3.1. It is shown in this table that both methods performed similarly, there seems to be a slight advantage for the lowpass filter in higher noise and a slight advantage for averaging in lower noise. Ultimately with the similar performance of the two methods, using averaging is justified as it is easier to implement on a microprocessor and is less computationally intensive.

Table 3.1 Comparison between using MATLABs lowpass function and averaging as a lowpass filter.

Noise Level	Lowpass % difference	Averaging % difference	Noise Level	Lowpass % difference	Averaging % difference
1	2.20	0.0847	100	8.84	11.3
1	2.34	0.0552	100	2.51	4.80
1	2.22	0.0611	100	9.24	12.0
1	2.29	0.0089	100	16.4	14.7
1	2.24	0.0416	100	2.16	4.79
10	2.14	0.157	1000	109	108
10	1.58	0.701	1000	12.8	13.4
10	2.62	0.381	1000	78.6	80.0
10	0.881	1.42	1000	195	203
10	1.58	0.732	1000	1.67	1.22

3.4 Lock-in Implementation

The lock-in amplifier implemented was done in software on a PIC24FJ128GC010 (Microchip Technology Inc., Chandler, AZ, USA), which is a 16-bit processor. The PIC has a 12-bit pipeline ADC, a 16-bit sigma-delta ADC, and a 10-bit DAC. Both ADC references were configured to use an external 3 V reference. The limiting factors for sampling rate are from the ADC and DAC data rates. The pipeline ADC has a maximum rate of 10 Msps where the sigma-delta only has 62.5ksps. The DAC has an effective 1 Msps. The DAC would be used regardless of ADC chosen and so even with the pipeline ADC the current maximum would be 1 Msps. The DAC's state was set via direct memory access (DMA), reducing CPU overhead. The lock-in algorithm that follows the data transmission and acquisition determines the frequency between measurements. The PIC has a single cycle 17-bit x 17-bit hardware multiplier which would benefit the multiplication stage of the lock-in algorithm; however, the multiplication stage of the algorithm uses 32-bit values and so this hardware multiplier may not be in effect.

For the final version of the software the reference signal frequency chosen was 100 Hz. A higher frequency would be preferable however would require more processing power and memory. The main loop of this program is signal transmission and acquisition, followed by the lock-in algorithm processing the acquired signal and lastly transmission of the results. This process approximately takes 366 μs and as such has a maximum overall fluorescence sampling rate of 2.7 Hz. The device was configured to 1 Hz for deployments. The main loop was controlled using timer2 of the PIC as an interrupt service routine (ISR) and as such the sample rate can be controlled predictably by adjusting how often this ISR is called. Similarly, the sample rate of the ADC is controlled using timer1. The DAC also used timer1 for data transmission. The DAC would be active prior to the ADC measurement due to set priority levels. The waveform produced by the

DAC had six periods of 100 Hz, each period containing 100 discrete steps. The resulting captured waveform would result in a 600-entry array in memory.

The core algorithm of the lock-in amplifier has a prefilter which removes the DC component which is inherent with an LED generated, and photodiode acquired signal. This filter simply takes the average of the acquired signal and subtracts the signal by this value. After this the normal algorithm discussed earlier is performed. First a multiplication of the in-phase and out-of-phase reference is done. This was done using the same reference used to generate the signal. Next the filtering was performed on each of these multiplied waveforms. This was done using an averaging filter to save on processing power and storage. First the waveforms are multiplied by an arbitrarily large value such that the maximum value would not overflow any registers, this multiplication is to minimize truncation errors. The averaging filter simply takes the average of the entire signal, like a moving average filter with the window size the size of the sample. This results in the X and Y components. These are then used in equations 4.27 and 4.30. The code in its entirety can be found in Appendix A.

3.5 Lock-in Implementation Results

First sub-unit tests were performed to validate the suitability for the eventual lock-in amplifier implementation. Two main modules were tested: the DAC-DMA for signal transmission and the ADC signal acquisition. There were two ADC tests: a best-case and worst-case scenario. In the best-case scenario a function generator was used to produce a clean input signal that was fed into the 16-bit sigma-delta ADC. In a worst-case scenario a digital signal from the 10-bit DAC was fed into the 12-bit pipeline ADC. Additionally, a max speed test was performed to determine the max fluorescence sampling rate. In this test the timer used to control the sample rate was not used, instead it was configured to immediately begin the next sample acquisition as soon as the last measurement was transmitted. A program was developed on windows to read the serial data being transmitted by the sensor and calculated the data per second: 366 µs.

For the DAC-DMA test the waveform transmitted was a 250 mVpp signal with a 125 mV offset. The output of the DAC was recorded on an oscilloscope (KEYSIGHT infiniVision DSOX2004A Digital Storage Oscilloscope). The signal acquired by the oscilloscope is shown in Figure 3.4 (a). Since an expected sinewave was produced the test can be considered successful. In Figure 3.4 (b) a zoomed in portion of the waveform is shown, highlighting the digital nature caused by a DAC.

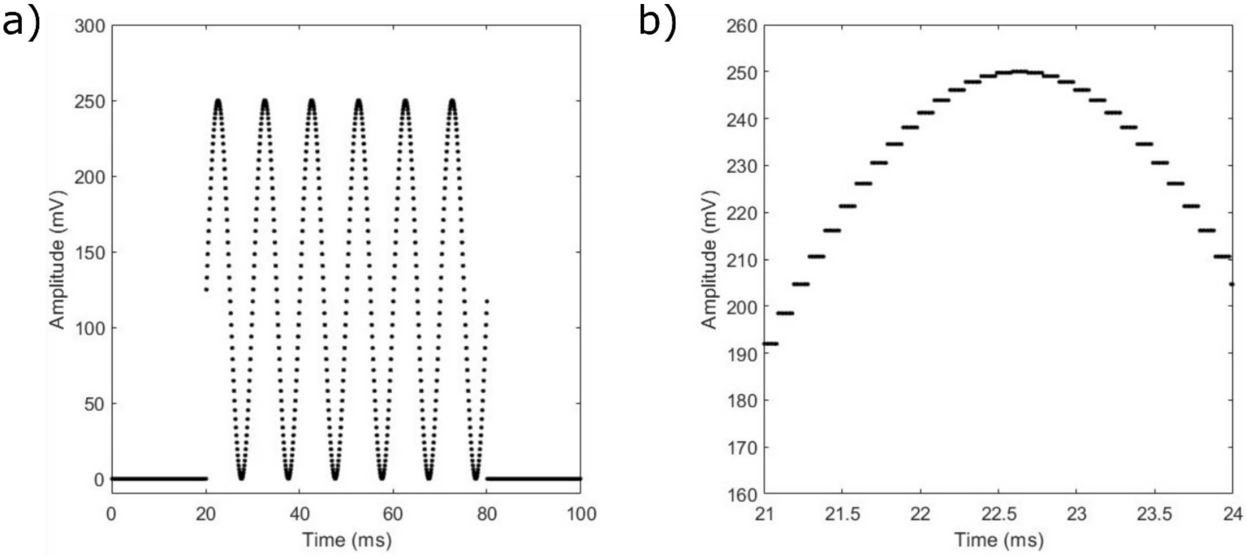

Figure 3.4: DAC output. (a) Oscilloscope date of the DAC output. (b) Data from the DAC output zoomed in to highlight the digital waveform produced.

In the worst-case scenario test a series of amplitudes were transmitted from the DAC to the pipeline ADC to measure. The peak-to-peak amplitudes transmitted were 1, 5, 10, 25, 50, 75, 100, 150, 200, 250, 500, 1000, 1500, 3000, and 3300 mV. For each amplitude a DAC sinewave was transmitted and measured three times. It was found that the resolution of the pipeline ADC was unable to measure 5 mV peak-to-peak and below, the results of the lock-in algorithm being 0 in these cases. An example of the recorded wave is shown in Figure 3.5 (a). The results of the lock-in performance using the pipeline ADC is shown in Figure 3.5 (b). Amplitudes of 75 mV and greater had error of 3% and below. The worst recorded error other than sub 5 mV was at 10 mV with 51 % error.

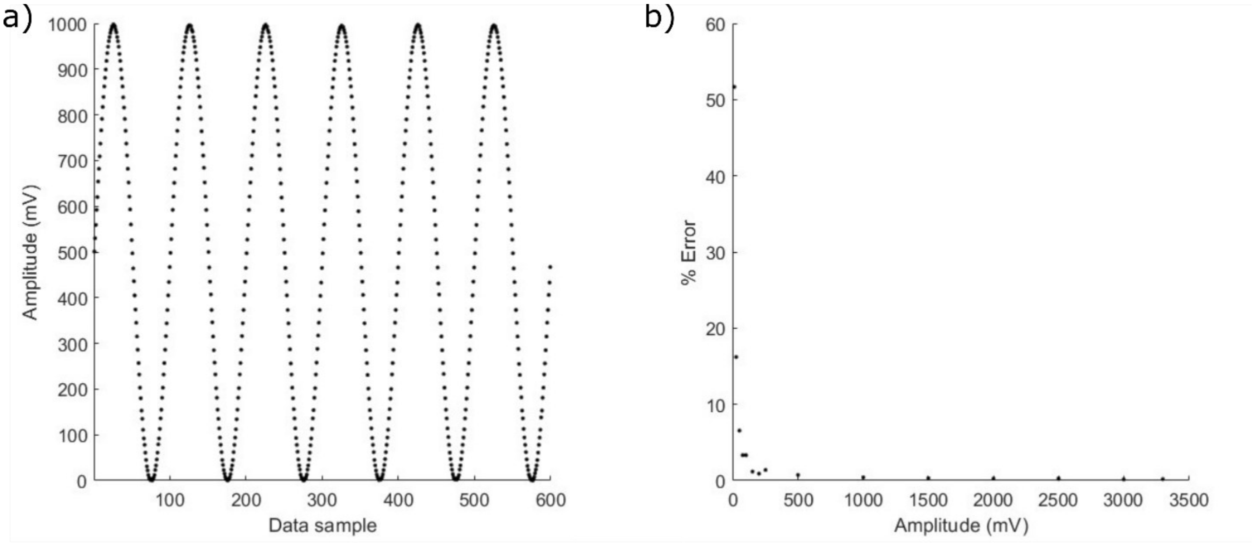

Figure 3.5: Pipeline ADC example date. (a) Data recorded by the PICs pipeline ADC which was generated using the DAC. (b) Error vs Amplitude curve of DAC to pipeline ADC data.

For the best-case scenario using the sigma-delta ADC tied to a waveform generator three measurements were taken per amplitude: the peak-to-peak amplitudes being 2, 5, 10, 100, 500, 1000, 1500, 2000, 2500, and 3000 mV. Using the sigma-delta ADC was successful in measuring lower amplitudes due to the high bit resolution. An example of the 1 Vpp measurement is shown in Figure 3.6 (a) and the results of the lock-in performance is shown in Figure 3.6 (b). Amplitudes of 5 mV and greater had error of 3% and below. The worst recorded error was at 2 mV with error reaching as high as 18%. Comparing the performance results of the two ADCs it is clear that the sigma-delta had less error and was able to detect lower voltages.

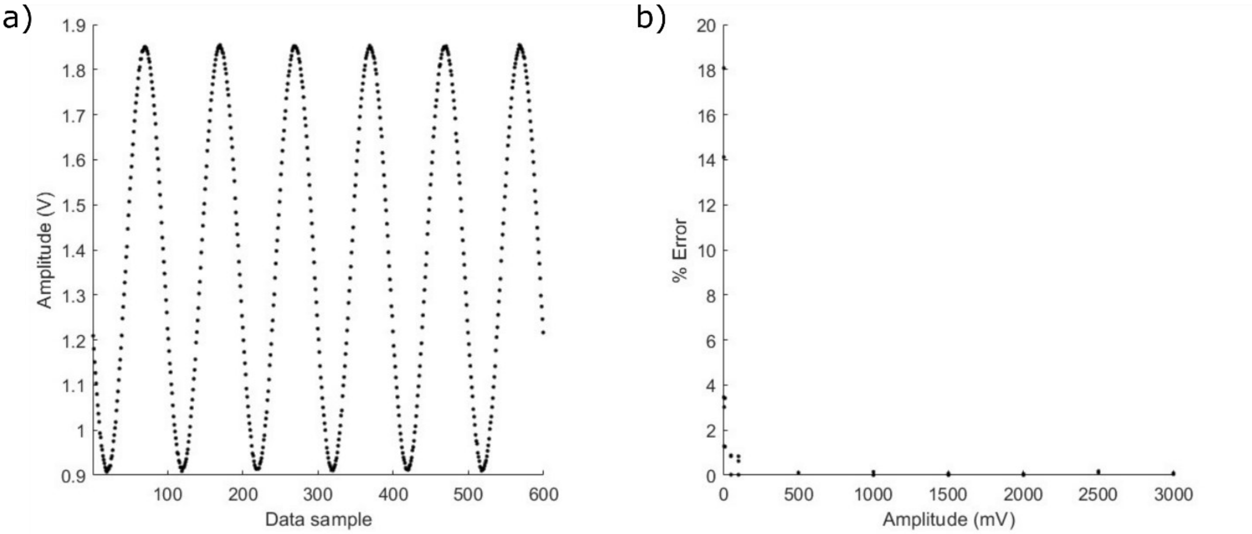

Figure 3.6: Sigma-delta ADC example data. (a) Data recorded by the PICs sigma-delta ADC which was generated by a waveform generator. (b) Error vs Amplitude curve of waveform generator to sigma-delta ADC data.

CHAPTER 4 OPTICAL LAYOUT

In this chapter, a new optical layout for a submersible fluorometer is presented, simulated, and implemented. Initially, the optical layout is designed and optimized for maximizing fluorescence stimulation and light collection. Optical ray tracing simulations of the entire fluorescence system were the basis for evaluating designs. I discuss the evolution of the design comparing optical power outputs for different configurations. Finally, the chapter concludes with a built and implemented physical setup along with preliminary calibrations. Ultimately, I show that the simulations match the experimental data well and the final fluorescence sensor is cost-effective, evidenced with a sub-component analysis and breakdown.

4.1 Design Process using Optic Studios Simulations

A series of simulations were performed to find an optimal design before implementing and building a fluorometer. The software used was Zemax's Optic Studios. Optic Studios is a raytracing software which is capable of simulating a variety of lenses in any shape with many material properties. The first iterations of simulations were based on a Turner Designs fluorometer [76] as shown in Figure 4.1. Initial simulations were to gain familiarity with Optic Studios simulating and to understand tolerances on part positioning. The sample being analyzed in all simulations presented in this thesis is Rhodamine B. The properties of the sample are based on spectral properties of Rhodamine B and are included with Optic Studios installation; however, slight configuration modifications are required to enable Optic Studios to accept them.

It will be important to understand some basics on Optic Studios' handling of rays for this chapter. Optic studios' rays come from light sources. Light sources have radiation intensity profiles which dictate the relative intensity of rays depending on the angle at which they transmit from the source. A light source will have a power associated with it. The power of a light source is distributed among the rays originating from the source. A light source will also have a set number of rays. The greater number of rays associated with a source means each individual ray will have less power but gives a greater resolution to a simulation. Rays are recorded on detectors. These detectors do not block rays, and so a ray can pass through multiple detectors, and each detector will record the ray as hitting them as the ray passes through them. Simulations with the same configuration may vary in results, especially if the source has a low ray count for a particular optical layout due to how rays are handled by Optic Studios; analogous to mesh resolution errors. Larger ray counts will take longer to simulate and require more memory from the computer.

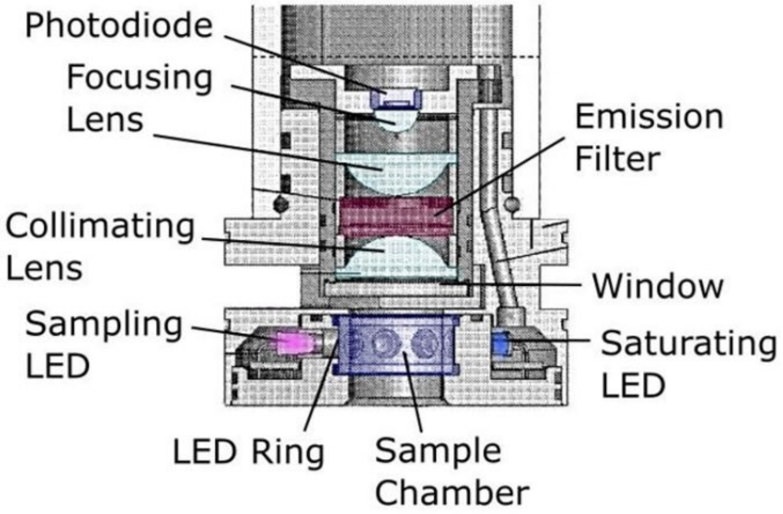

Figure 4.1: Cross-section of a Turner Designs fluorometer. Reprinted from reference [76].

The first simulated iteration of an optical assembly is shown in Figure 4.2. It consisted of a fluorescence sample (Rhodamine B), a collimating lens, a focusing lens, an aperture, an emission filter, a light source, and a series of detectors used for characterization. Like the Turner design in Figure 4.1, the light source in Figure 4.2 is perpendicular to the collection stack. Here I define the collection stack beginning with a glass interface followed by the aperture, the collimating lens, the filter, the focusing lens and the detector(s), respectively. The light source in this design had a radiation intensity profile based on the LXHL-BD01 LED. The spectrum of the light source was generated using a Gaussian curve centered at 521 nm and due to the simulation limitations had been truncated at 501 nm and 541 nm with 24 discrete points. The lenses used in this first simulation were both plano-convex. The collimating lens had a 12.7 mm diameter, a 15.0 mm focal length, a 11.35 mm back focal length, suitable for the visible and near-infrared spectra (VIS-NIR coated) (stock number #62-592, Edmund Optics Inc., New Jersey USA). The focusing lens had a 10 mm diameter, a 30 mm focal length, a 28.01 mm back focal length, and had a VIS-NIR coating (stock number #63-523, Edmund Optics Inc., New Jersey USA).

The first simulation had three detectors before the focusing lens. One just after the filter, one just before the filter and one within the aperture. The purpose of these detectors was to monitor the spectral properties at each stage. This was done to verify the functionality of the sample volume's ability to generate fluorescence and the functionality of the emission filter. The spectrum captured by the aperture detector is shown in Figure B.1 in Appendix B. The detector at the aperture had captured the spectrum of both the light source and generated fluorescence. This spectrum verified that the sample volume had generated fluorescence that matches the spectra measured in reality, as shown in Figure 1.3. The spectrum captured by the detector just before the filter is shown in Figure B.2 in Appendix B. The detector just before the filter had only captured the fluorescence spectrum, largely because of the orthogonal orientation of the LED light source and aperture, in combination. The spectrum captured by the detector just after the filter is shown in Figure B.3 in Appendix B. The detector just after the filter had captured a truncated version of the fluorescence spectrum. This truncation verifies that the implementation and functionality of the emission filter; however, more narrow and aggressive filters can be substituted and were when fabricating.

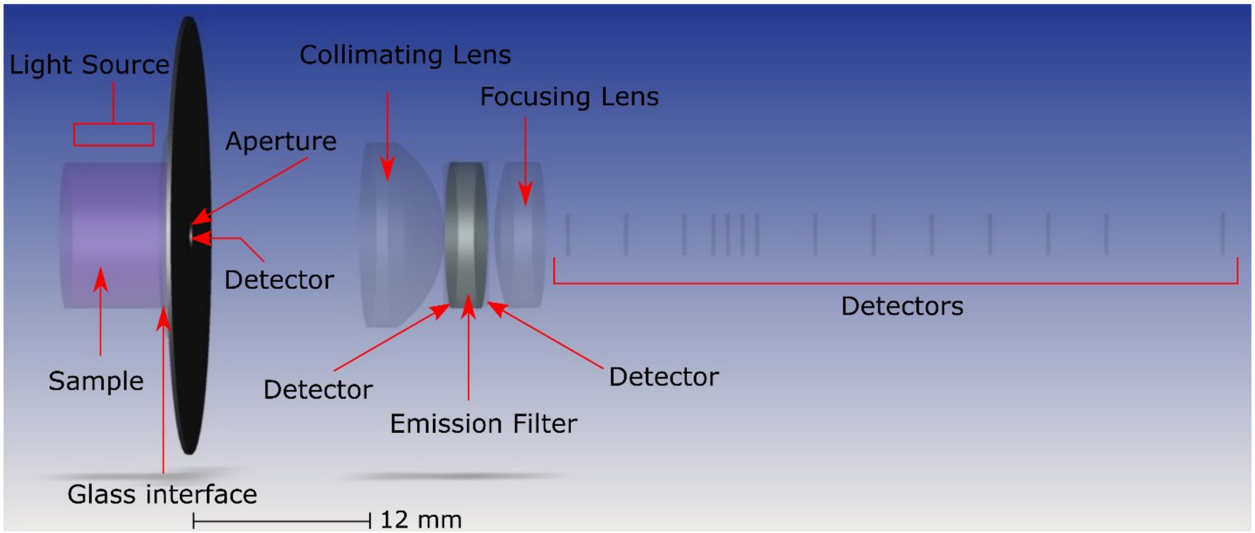

Figure 4.2: Optic Studios rendering of a fluorescence stack. This stack contains a light source aimed at the sample perpendicular to the collection optics; however, it is not visible in this figure.

The first simulation also had a series of detectors following the focusing lens. The purpose of these detectors was to capture the power generated by the rays at various distances behind the focusing lens. The results of three simulations using the configuration of Figure 4.2 are found in Figure B.4. It was found that the power was most intense at 14 mm beyond the focusing lens. Notably this is not at the claimed back focal point of 28.01 mm of the focusing lens.

The second set of simulations were targeted at tolerances in angular alignment. The setup was the same as the first simulations described above with the exception that only one detector was considered as shown in Figure 4.3. The detector that was considered was the detector deemed most ideal for maximum light collection, 14 mm behind the focusing. With this an angle sweep was performed with the light source to understand its tolerances. The convention of angle, as shown in Figure 4.3, is negative toward the interface and positive away from the interface. The results of this angle sweep are shown in Figure B.5 in Appendix B. It was found that the maximum intensity was when the light source was -10° to -20° with an increase of approximately 20 % power collected at the detector (~120 nW). At a 20° angle the intensity at the detector had degraded by half (51%) the intensity compared to the intensity at 0°, with an integrated power of (~50 nW).

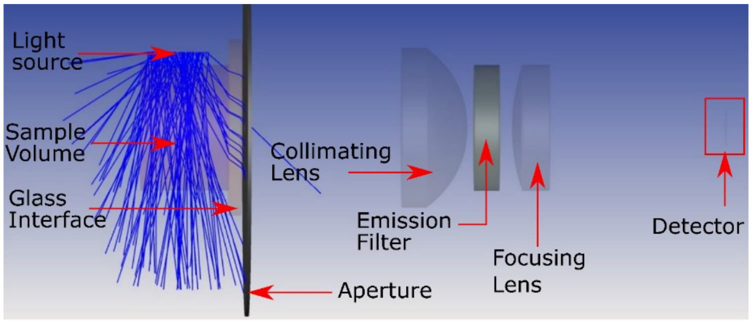

Negative orientation

Positive orientation

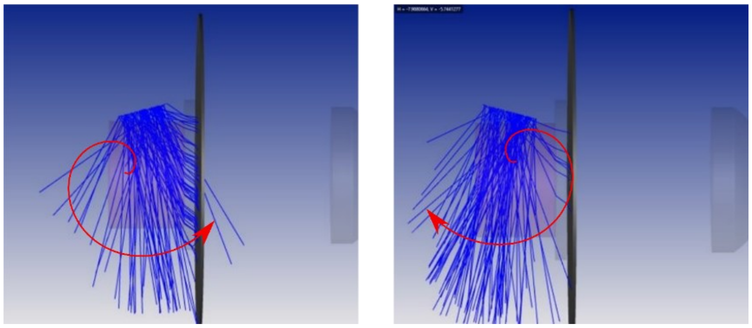

Figure 4.3: Angular tolerance study in Optic Studios. The bottom left image shows a negative angle orientation, the bottom right image shows a positive angle orientation. Design based on plano-convex lenses.

To confirm Optic Studios simulations and to investigate the discrepancy between the measured focal point of the focusing lens and the theoretical focal point, I also developed a custom MATLAB simulation from analytical first principles. In MATLAB a simple plano-convex and ball lens 2D ray tracer was developed using Snell’s law to provide rapid results on ray path information. Figure B.6 show the effects of slightly non-collimated light traveling through a lens. The effect shifts the focal point closer or further from the lens depending on whether the incident light (entering from top of graph) is divergent or convergent. The results of MATAB agreed well with the Optic Studios simulations. In fact, having explored the properties of plano-convex and ball-lenses in MATLAB, a new improved setup was created in Optic Studios based on ball-lenses for high light collection efficiency. This setup used two identical ball lenses with 10 mm diameters with N-BK7 substrate properties (stock number #45937, Edmund Optics Inc., New Jersey USA) for the collection and focusing of rays. The back focal length of each ball-lens was determined via MATLAB to be approximately 6 mm. The updated and proposed setup is shown in Figure 4.4.

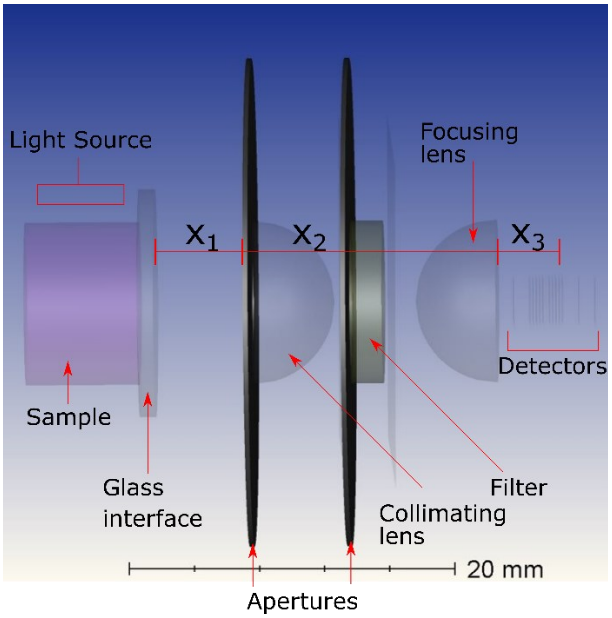

Figure 4.4: Optic Studios rendering of a fluorescence stack, improved from previous design. This stack includes a second aperture at the filter and moves the first aperture away from the sample and places it against the collimating lens. Design based on ball-lenses.

The third set of simulations was targeted at collimating the light from the sample chamber using the ball-lenses in the optical stack of Figure 4.4. Figure 4.5 (a) shows the simplified setup with only the sample volume and collimating lens. In this setup the distance between the lens and interface, X_1, was varied to identify beam divergence/convergence. Two detectors past the lens were used to determine the deviation from collimation of the collected light. Figure 4.5 is an example output from a detector. The diameter of the collected light from each detector is used to determine the angle of deviation from collimation. The distances of X_1 were 5, 6, and 7 mm. It was found that the ‘collimated’ beam was 5.7° divergent at 5 mm, 1.7° divergent at 6 mm and 1.1° convergent at 7 mm.

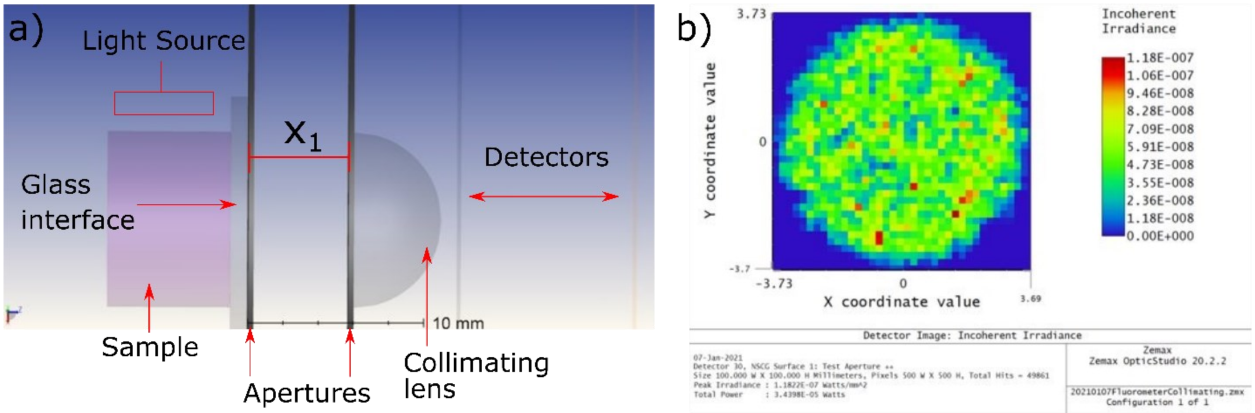

```
07-Jan-2021
Detector 30, NSCG Surface 1: Test Aperture ++
Size 100.000 W X 100.000 H Millimeters, Pixels 500 W X 500 H, Total Hits = 49861
Peak Irradiance : 1.1822E-07 Watts/mm^2
Total Power     : 3.4398E-05 Watts
```

Figure 4.5: Optic Studios rendering of a simple fluorescence stack. (a) Optic Studios rendering of the sample being collimated. (b) Example output from detector.

Given that the light is collimated between the two half-ball lenses, the setup was restored to what is shown in Figure 4.4. X_2 is selected primarily to accommodate the physical width of the emission filter. Here it was chosen to be 12 mm. The focusing lens was the last element to be optimized, or specifically, the distance X_3 between the lens and the eventual photodiode/detector. In Appendix B, Figure B.7 to Figure B.9 show the results of the different X_1 distances that were considered. Each figure plots the power distance profile X_3 for each X_1 distance to determine the maximum power output. For example, the 5 mm (X_1) simulation had a maximum power of 1100 nW on the detectors from 2.8 mm to 3.2 mm (X_3).

The fourth set of simulations was to determine the impact of rays off the central axis, as shown in Figure 4.6. In Figure 4.6 there are two lenses (gray) and three light sources; a light source in blue in the focal area of the collimating lens, and two other light sources in red and green that are not in the focal area (off-axis). It can be seen that the blue light source when passed through the two lenses is focused to a point through the center axis; however, the other two sources are appropriately mirrored and offset as expected. These simulations were used to determine the minimum photodiode surface area and dimensions required to capture beams off the central axis. At the focal point, it was determined that a photodiode dimension of ~2-3 mm diameter would be required for a similar offset in fluorophores in the sample chamber. Notably a third lens as shown in the Turner Design, Figure 4.1, would collect more off-axis rays increasing collection efficiency.

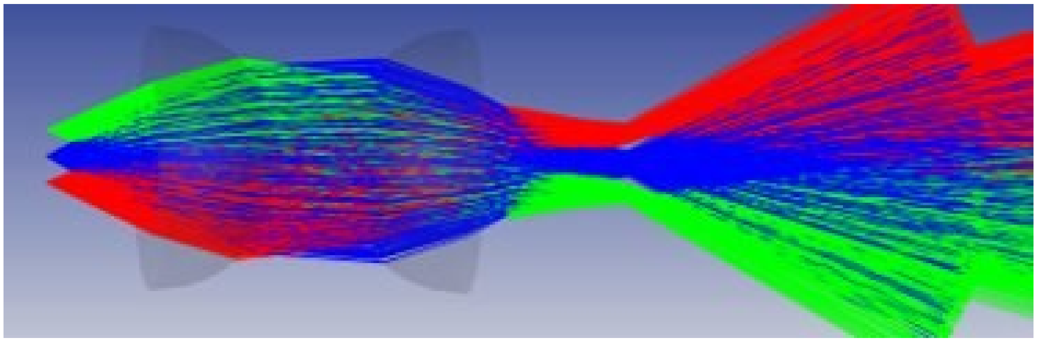

Figure 4.6: Optic Studios rendering of two lenses, one collimating and the other focusing. There are three light sources, one, green, one blue, and one red. The blue is in the center of the lenses while the other two are offset. This rendering demonstrates how light from multiple sources overlap the most at the flat face of the focusing lens, where the light source in the center is focused at the focal point.

Thus far, the simulations proved effective for stimulating a fluorescence dye, for implementing optical filters, for determining the light source angle sensitivity, and for placement of collection lenses/detector. However, the simple mock-designs presented thus far have the light source on the same side as the sample and has not made use of an excitation filter. This orthogonal interrogation angle is ideal for sample excitation but not for physical simplicity because the LED and excitation filters would protrude from the eventual sensor instrument as in the early Turner designs. A better design would have the optics resided on one side of the interface, which leads toward my final design resulting from simulation optimizations.

4.2 Final Optic Studios Simulation

Placing the optics entirely behind the end-cap or face plate presents numerous challenges. First, guiding light under the collimating lens is physically challenging to accommodate the filters and optics. It is ideal to have the collimating lens closest to the sample to collect maximum fluorescence; however, the closer the lens the more difficult it is to guide the excitation beam beneath it. Second, the acrylic interface refracts the excitation light and requires alignment to the focal length of the collimating lens. The acrylic faceplate also extends focal length of the collimating lens. These aspects are challenging to calculate analytically and are difficult to visualize; therefore, necessitate Optic Studios raytracing simulations. The finalized design that addressed these challenges is shown in Figure 4.7 (a).

4.2.1 Simulation Parameters

Figure 4.7 (a) shows the optical layout for the final set of simulations. A volume of rhodamine, left of figure, was created behind an acrylic plate. This acrylic plate serves as a barrier between the environment and sensor. This interface simulates the acrylic 3” series endcap from blueROV. On the sensor side of the interface there are two sets of optics: the emission optics and the excitation optics. The emission optics serve to collect the generated fluorescence. The emission optics consist of a collimating lens, emission filter, focusing lens and photodiode arranged in this order starting from nearest to the interface as shown in Figure 4.7 (a). The excitation optics serve to generate fluorescence centered at the emission optic’s focal point. The excitation optics consist of the excitation filter, a focusing lens and the LED in this order starting from nearest to the interface as shown in Figure 4.7 (a). The excitation optics are 65° from the interface’s normal line.

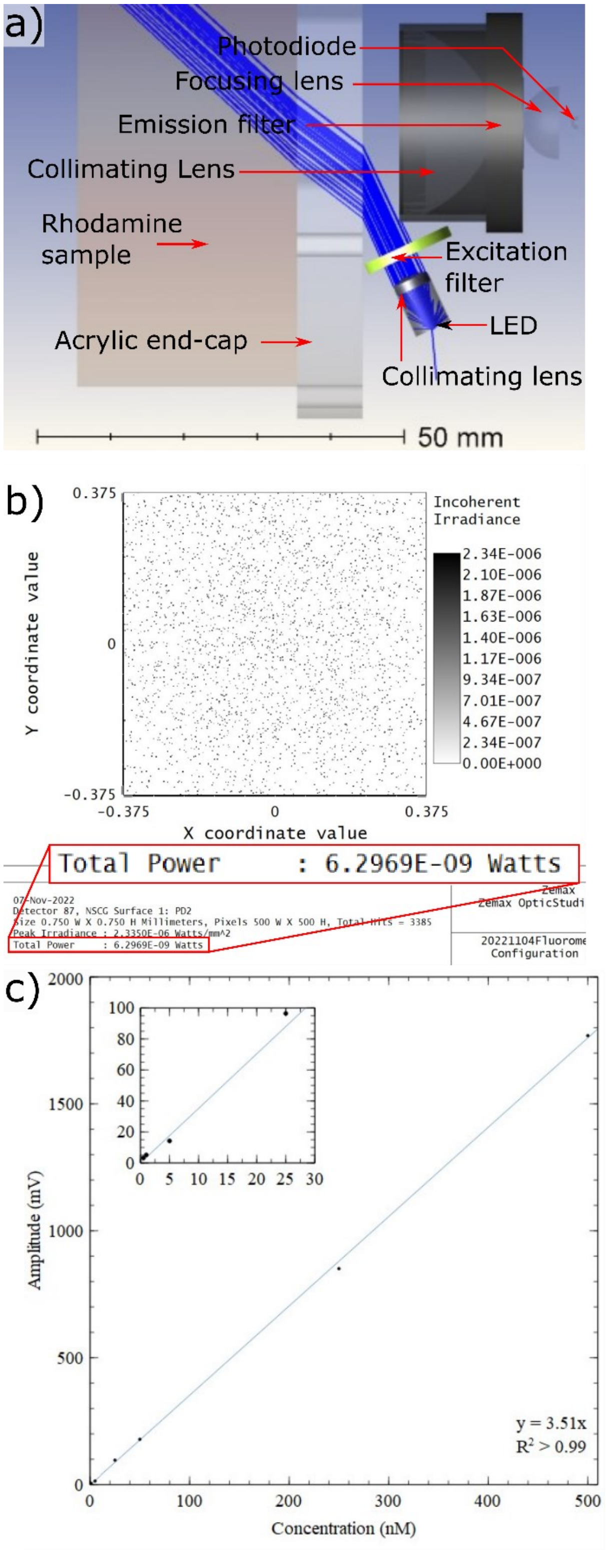

```
Total Power      : 6.2969E-09 Watts
```

```
07-Nov-2022
Detector 87, NSCG Surface 1: PD2
Size 0.750 W X 0.750 H Millimeters, Pixels 500 W X 500 H, Total Hits = 3385
Peak Irradiance : 2.3350E-06 Watts/mm^2
Total Power     : 6.2969E-09 Watts
```

Figure 4.7: Complete optical layout simulation. (a) An Optic Studios rendering of the optical setup used for simulating. (b) An example output of a simulation. An x-y radiation pattern plot of the detector is shown. The key data, the total power observed by the detector, is boxed and zoomed on in red. (c) Simulated calibration curve. The inset plot is the lower concentrations of 1 to 50 nM.

The LED in the simulation is mimicking the actual fluorometer's LED, a Roithner 525-33 LED, the peak wavelength is 525 nm with a full width half max (FWHM) of 28 nm. The area of emission for the LED was simulated as a circle with radius of 350 µm, as the specification sheet mentions a 350 x 350 µm InGaN source. The LED's spectral properties were based on the same LED however were truncated due to the simulator's limitations, and so 24 discrete points were chosen starting from 500 nm and ending at 541 nm. Similarly, the intensity output profile simulated was discretized into 91 points and was based on the datasheet. The power given to the source was 9 mW corresponding to the typical 20 mA power draw of this LED.

In Figure 4.7 (a) dark material can be seen surrounding a few optical components. This material blocks rays and holds optical components in alignment along the central axis. The LED and plano-convex lens in the excitation optics were encased in this material. This was done to prevent rays from the LED reaching the photodiode. Similarly, the collimating lens and emission filter were encased preventing unfiltered rays from reaching the photodiode.

The detector in the simulation approximates the realized device's photodiode (TSL257, Texas Instruments - TAOS, USA). The simulated design is comprised of four components, a square detector, an aperture, a lens and a cylindrical volume. This photodiode has an integrated ball lens with a radius of 0.9 mm, followed by 0.07 mm of plastic until the 0.75 mm in diameter photoreceptive area. This was simulated using a 0.9 mm ball lens in combination of a cylindrical volume with a radius of 0.9 mm and a height of 0.07 mm. The photodiode datasheet claims the clear plastic has an index of refraction of 1.55 and so polycarbonate was used as the simulated material having a similar simulated index of refractive of 1.5855. The square detector and aperture are combined to simulate a circle detector due to the simulator's limitations a square detector was used. The detector is a 0.75 mm x 0.75 mm square, and the aperture has an inner diameter of 0.75

mm and an arbitrarily larger diameter of 2.4 mm. The optical power was converted to current and to voltage using an integrated transimpedance amplifier with gain of 320 Mohm, used for Figure 4.7 (c) voltage calculations.

The sample chamber in the simulation was made by using a cylinder volume with an arbitrarily large depth and diameter such that a maximum fluorescence stimulation occurred. This volume was given the material properties of seawater, which in optic studios gives it a refractive index of 1.3395. The volume physics of the sample were modified such that it would mimic Rhodamine B fluorescence. Optic Studios has three files associated with fluorescent properties, a zas, zes and zqe file. The zas file contains the absorption spectra of the sample, the zes file contains the emission spectra of the sample and the zqe file contains the quantum efficiency of the sample. The absorption and emission files provided with optic studios were unaltered however the quantum efficiency was modified to 0.31 oppose to the default 0.70 as it was found that 0.31 for Rhodamine in water was a more reasonable quantum efficiency as found in literature [77]. There are three remaining variables that dictate the fluorescence properties, and they are the extinction coefficient, extinction wavelength and phosphor density. The extinction coefficient used in the simulation was the default 105,000 $(\mathrm{cm}\cdot\mathrm{M})^{-1}$, this is also supported by the literature [78]. The extinction wavelength used in the simulation was the default 0.55 μm. The phosphor density was varied to control the concentration of the sample, the conversion between the concentration in M and phosphor density in cm^{-3} is done by multiplying by Avogadro's number, and converting from litres to cm^3, as shown in equation 3.1.

$$concentration\ \frac{mol}{L}\frac{6.022x10^{23}}{mol}\frac{1L}{1000cm^{3}} = phosphor\ density\ cm^{-3} \qquad 3.1$$

The simulated filters make use of custom material properties. When modifying the material properties, a transmission profile can be created. The table has three categories, wavelength, transmission, and thickness and can hold up to 100 entries. The thickness of each filter is unchanging and so for this column of data the value remains unchanged. The wavelength and transmission values were obtained from spectra available on Edmund optics webpage. The excitation filter is a shortpass filter with a cut off at 550 nm (stock number #87-738, Edmund Optics Inc.). The emission filter is a bandpass filter with a central wavelength at 578 nm with a 16 nm window (stock number #84-695, Edmund Optics Inc.).

4.2.2 Simulation Results

When performing the simulations two variables would be altered between collecting data points: the number of rays produced by the light source and the phosphor density. As mentioned before the phosphor density variable controls what concentration the sample volume would have, and so for each simulation only one concentration would be measured. The number of rays assigned to the source had a trade off; the more rays the higher resolution of the simulation but the longer it would take. The time each simulation took was between 2 and 10 days on an Intel 8-core i9900k with 64 GB of Ram. The lower concentration simulations required more rays and as such took longer. An example of the output of a simulation is shown in Figure 4.7 (b). To obtain a value for the calibration curve, the total power is taken from the plot as shown in Figure 4.7 (b) and converted to a voltage using the photodiode’s responsivity (0.28 V/nW), which encompasses the photodiode’s optical-to-current response and transimpedance amplifier.

Figure 4.7 (c) shows the calibration curve of the processed results of the simulations. The simulations used the following concentrations: 0.5, 1, 5, 25, 50, 250, and 500 nM Rhodamine B.

The resulting curve was linear as expected with a slope of 3.5 mV/nM. The simulation predicts that it is possible to detect fluorescence at sub nano molar concentrations, the 0.5 nM prediction being 3.2 mV. The above simulations demonstrate that the final design will yield nM (ppb) limits of detection suitable for oceanographic applications.

4.3 Submersible Implementation

4.3.1 Physical Design

Figure 4.8 shows the final realized design. Figure 4.8 (a) shows a cross section of the sensor revealing the as-built optical layout. Beginning at the light source, a green 525 nm LED (LED525-33, Roithner Lasertechnik GmbH, Vienna Austria), is used for the excitation. The cone of light emitting from the LED is first collimated using a plano-convex lens (stock number #48-652, Edmund Optics Inc., New Jersey USA). The collimated light will then pass through the excitation filter (550 nm 12.5 mm Diameter, OD 4.0 Shortpass Filter, stock number #84-695, Edmund Optics Inc., New Jersey USA) perpendicularly. The collimated and filtered beam will next interact with a 9 mm thick acrylic interface. The beam passing this interface will refract such that when it meets the acrylic to environment interface it will be centered under the emission optics. The first component in the fluorescence collection stack is a relatively large aspheric lens 25 mm in diameter (Uncoated Molded Aspheric Condenser Lens, stock number #36-168, Edmund Optics Inc., New Jersey USA). The aspheric lens was used to collect maximum fluorescence and collimate it through the excitation filter (578 nm central wavelength, 16 nm Bandwidth, OD 6 Fluorescence Filter, stock number #87-738, Edmund Optics Inc., New Jersey USA). The collimated and filtered beam is then guided through a half ball focusing lens, 10.0 mm in diameter (N-BK7 Half-Ball Lens, stock number #45-937, Edmund Optics Inc., New Jersey USA). The ball lens directs the filtered fluorescence to the photodiode (TSL257, Texas Instruments, USA). This photodiode has a half ball lens integrated onto it as described above.

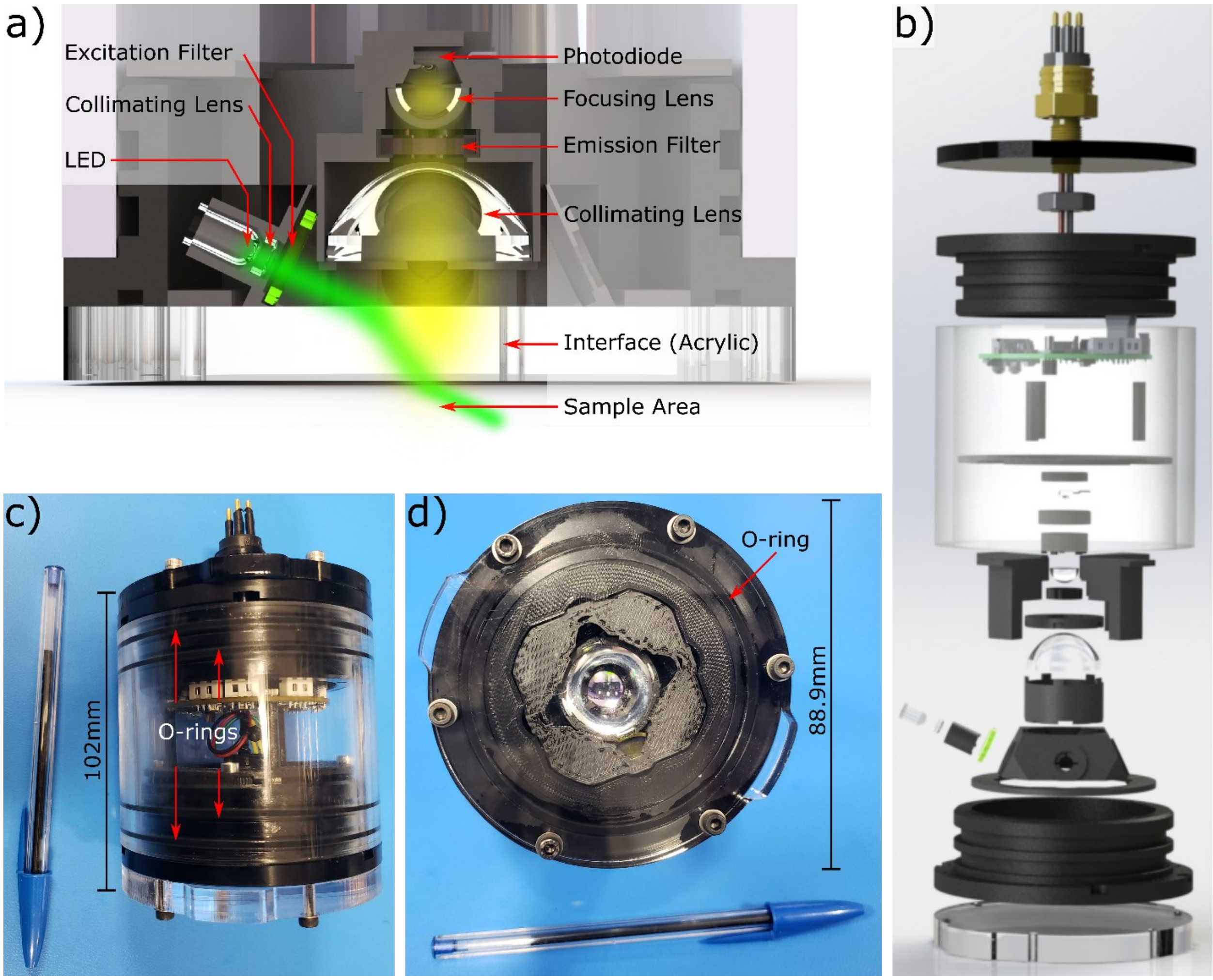

Figure 4.8: Submersible fluorometer build. (a) A cross-sectional view of a 3D rendering of the realized submersible fluorometer. The excitation beam in green can be seen exiting the LED where it then is guided by the collimating lens then transmitted through the excitation filter then is redirected by the acrylic interface where it then finally reaches the sample. The excited fluorescence in yellow travels through the interface where it is then collimated through the emission filter and finally focused on the photodiode for detection. (b) An exploded view of a 3D rendering of the realized submersible fluorometer. The complexity of the mechanical housing can be seen here. (c) A side view image of the prototype fluorometer developed with a pen for scale. (d) A bottom view image of the prototype fluorometer developed with a pen for scale.

A part of the low-cost theme of this design, OTS housing components from BlueRobotics were used in the design. The interface between optics and sample is a clear acrylic 9 mm plate

(Clear Acrylic End Cap (3” Series), BlueRobotics, California USA). The acrylic plate package comes with M3 hex screws and washers intended for flange mounting. There are a total of 6 equally spaced circularly symmetric holes along the edge of the acrylic for mounting. The main housing is an acrylic tube (Cast Acrylic Tube (3” Series), BlueRobotics, California USA), where the electronics, optics and 3D internal housing are contained. On either side of the tube are the endcaps, comprised of a plate and flange. Figure 4.8 (d) show the measurement end of the sensor which has a clear acrylic plate. Between the plate and flange is an o-ring, which is greased with silicone for proper sealing. Figure 4.8 (c) shows a side view of the sensor. Between each flange and the main tube there are two o-rings, also coated in silicone grease, these are most visible in Figure 4.8 (c). On the opposite side of the measurement end another plate was custom made using a tinted acrylic plate (9M001, Acrylite, Sanford USA) cut using an Epilog Mini24. The same o-ring configuration was used between the plate, flange, and tube as the other end cap. The tinted plate mounted to the flange in the same manner as the clear plate. This tinted plate additionally had a hole cut into the center to accommodate the subConn connector (Micro Circular 6M connector, MacArtney, Nova Scotia Canada). The subConn connector had an o-ring between it and the tinted plate on the outside, where on the inside it was fastened with a 7/16-20 Hex Nut and 7/16 washer. The final dimensions of the housing are 102 mm (height) x 90 mm (diameter).

Figure 4.8 (b) shows the many parts involved in an exploded view of the fluorometer. The internal housing components of the optics were created using 3D printing technology. The prints were designed to be mounted and to connect like puzzle pieces and be symmetrical circularly. The design allowed for up to four LEDs and four excitation filters however only one of each was used. Unused LED slots were plugged. The main function of the prints is to hold the optical stack together, additionally it blocks stray rays from reaching the detector.

The electronics used for this design are from a modified printed circuit board (PCB) from a previous project. The PCB was designed by an electrical engineer Merle Pittman contracted from Dartmouth Ocean Technologies Inc. This PCB was originally used for an *in situ* phosphate sensor which uses microfluidics and absorption spectroscopy. This PCB was based on a PCB designed during my senior year project working with the Sieben Lab. The electronics for absorption spectroscopy are the same for fluorescence however because this fluorometer does not incorporate flowthrough measurements it does not need the motor electronics found on the PCB. The active components of the PCB for fluorescence measurements includes: the PIC24FJ128GC010 as the microcontroller, a constant current driver to generate the signal, a photodiode circuit for receiving the signal, and an analog reference for precise measurements. Additionally, the fluorometer makes use of the PCB's RS-232 chip for communications. The PCB also includes a reverse polarity protection circuit and power monitor. The motor driving circuit is in a sleep mode when utilized with the fluorescence software. The modifications I made to the board were the removal of lowpass filters on the optics circuity because the lock-in algorithm, described in Chapter 3, operated at a higher frequency than the phosphate sensor.

Figure 4.9 is a schematic of the constant current driver on the PCB. The constant current circuit for the LED(s) is a circuit that our lab has used in many absorption spectroscopy projects. The LED's anode is connected to a high volt source, for the fluorometer that would be the voltage level fed to it, 12V, and its cathode connects to a transistor. Traditionally our lab had used BJTs however in this design, a MOSFET was used instead for power efficiency. The LED connects to the drain, the source then connects to a resistor, which connects to ground. The transistors gate is connected to an op amp through a resistor. The negative input of the op amp is connected to the source of the transistor. The positive node of the op amp is connected to the PIC's DAC output through a resistor. The photodiode circuit is simple, the photodiode used has three pins, two are for power and one is for the received signal. The signal pin is routed to the PIC's ADC via a resistor.

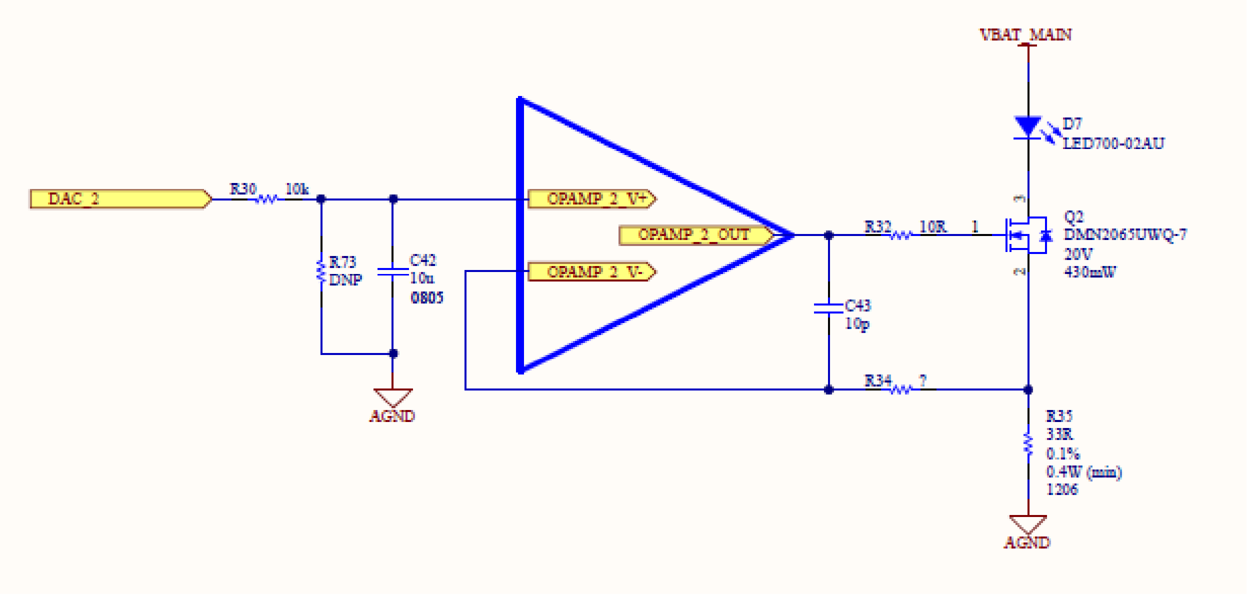

Figure 4.9: Circuit schematic of the constant current LED driver.

The TTL chip used was to establish the RS-232 communication the fluorometer now uses for streaming the data it generates. The device itself is not self logging and so the stream must be recorded externally. The connection from the fluorometer to the integration platform is a SubConn micro circular M6 connector. This connector has six pins, one of which was not used, two were for power, and three for the communications. The pins used were the minimum that RS-232 requires which is a ground pin, transmission pin and receiving pin. The configuration for communication was 9600 baud rate, 8 data bits, 1 stop bit and no parity. The data stream had the following format: an open parenthesis followed by the magnitude lock-in result, a comma delimiter, the phase lock-in result, a closed parenthesis, an endline character and ending with a return carriage character.

When fully implemented the sensor was found to have an average power draw of 19 mA at 12V (0.23 W), with a current range of 17 mA to 46 mA. Figure 4.10 shows the current/power profile of the fluorometer when operating. Highlighted in red is the transmission period, a period in which the LED is engaged and transmitting a sinusoid, and the ADC is receiving a signal via a photodiode. The device consumes the most power when the LED is engaged, at this time the current draw will reach 46 mA. In green is the period in which the signal processing, the lock-in algorithm, is taking place. In purple is the period in which the signal processing results are transmitted via RS-232. In yellow the device awaits idle until the next sample is taken. The power data was obtained using an oscilloscope (KEYSIGHT infiniVision DSOX2004A Digital Storage Oscilloscope) and sense resistor.

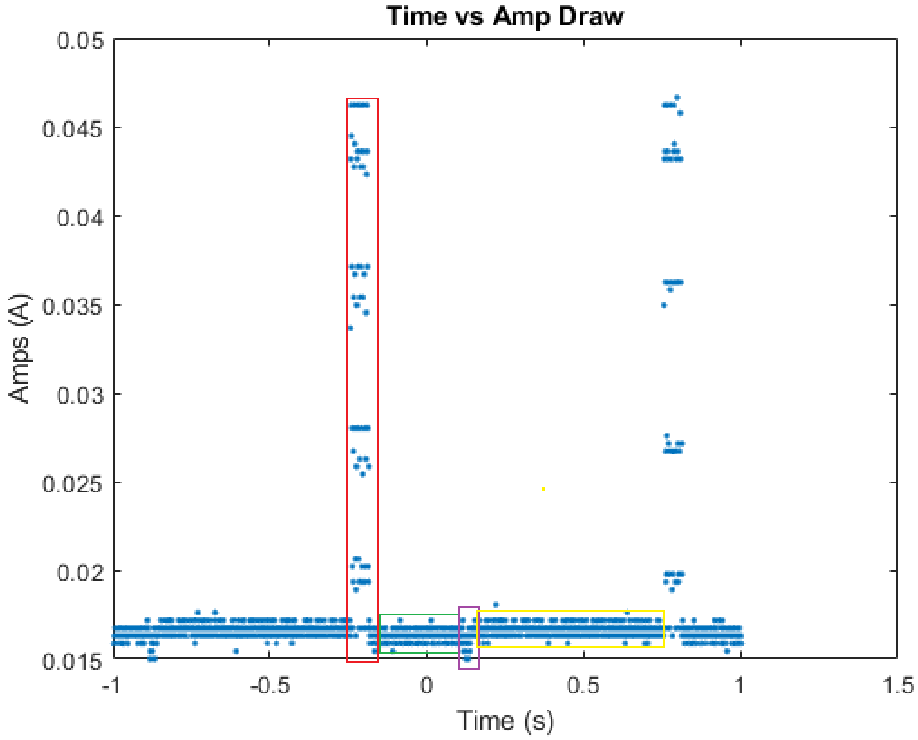

Figure 4.10: Current draw profile of the fluorometer. A current vs time plot, representing the power draw of the developed fluorometer when multiplied by the 12V supply. Boxed in red is the current draw during transmission using the LED. Boxed in green is the current draw during the lock-in algorithm. Boxed in purple is the current draw during transmission via serial port. Boxed in yellow is when the device is busy waiting for the next sample.

4.3.2 Component Price Breakdown

The price breakdown of the fluorometer is shown in Table 4.1. From the table the large price points can be identified. The largest prices being the optical filters, SubConn connector and the PCB. The optical filters are high optical density, the emission being fourth order and the collection being sixth order. The higher the optical density the greater the undesired wavelengths are filtered out. The trade off is that higher quality filter cost more but are better at removing wavelengths outside of the targeted spectral ranges. SubConn connectors are a robust mating electrical interfaces for underwater instruments and are the typical standard for commercial devices; e.g. the Turner Series Cyclops. Using the industry standard to prevent leakage justifies the price. For example, our lab has experience with using lower cost methods; a project in my undergrad and early masters we had used cat cables with epoxy as a seal for a nitrite/phosphate sensor, and we found that after prolonged use leakage into the device was found. The custom PCB has a price which can be reduced in the future; it was designed for an earlier project and has numerous unused components for the fluorometer. The PCB was used to decrease development time of the project. Overall, the project was still a success as it had a sub thousand-dollar price in the end.

Table 4.1 Bill of materials for the developed fluorometer.

Part	Company	Price $ (CAD)
Clear Acrylic End Cap (3” Series)	BlueRobotics	12.10
Cast Acrylic Tube (3” Series)	BlueRobotics	18.15
O-Ring Flange (3” Series) x2	BlueRobotics	58.08
Custom tinted acrylic end cap	9M001, Acrylite, Sanford USA	3.75
SubConn connector	MacArtney	182.63
Custom PCB[1]	Dartmouth Ocean Technologies Inc.	153.03
LED	Roithner	4.25
LED Focusing lens	Edmund optics	40.50
Collimating lens	Edmund optics	32.20
Focusing lens	Edmund optics	56.03
Excitation filter	Edmund optics	178.20
Emission filter	Edmund optics	232.20
Misc[2]		7.05
Total		978.17

1: Custom PCB was from another project and has many extraneous parts adding to the price.

2: Misc includes PLA material for 3D prints, screws, washers, and jumper wire.

4.4 Benchtop Testing

Before a fully submersible device was realised, a benchtop version of the sensor was created. This prototype has the same optics, however the hardware driving it is slightly different. The hardware used was a development board using the same PIC processor and a breadboard with a constant current driver on the DAC output. This constant current driver had used BJTs instead of the MOSFETs that were implemented on the PCB. This bench calibration used Rhodamine B in petri dishes. The device was suspended using 9 mm acrylic rings such that each measurement was looking at the same depth of sample. In Figure 4.11 (a) the constructed optical stack is shown, encased in 3D print. In Figure 4.11 (b) the collimation stack is removed displaying the excitation optics; this demonstrates that the LED is focused along the center of the optical layout. Notably the LED used in this figure was not the final LED used, as this is an orange LED which would not be used for Rhodamine excitation. In Figure 4.11 (c) the electronic setup is shown attached to the optics. In Figure 4.11 (d) the samples and acrylic ring is shown. The calibration used five concentrations, 1, 10, 50, 500 and 1000 nM. Calibrating was done similarly to the microfluidic calibration in Chapter 2. Calibration would begin by taking a measurement in a blank (0 nM sample), followed by a measurement in a sample. The device would then be rinsed between measurements. This would be repeated until all samples have been measured. Measurements were done in triplicate. The results of this calibration are shown in Figure 4.11 (e). The calibration had a strong linear relationship as expected.

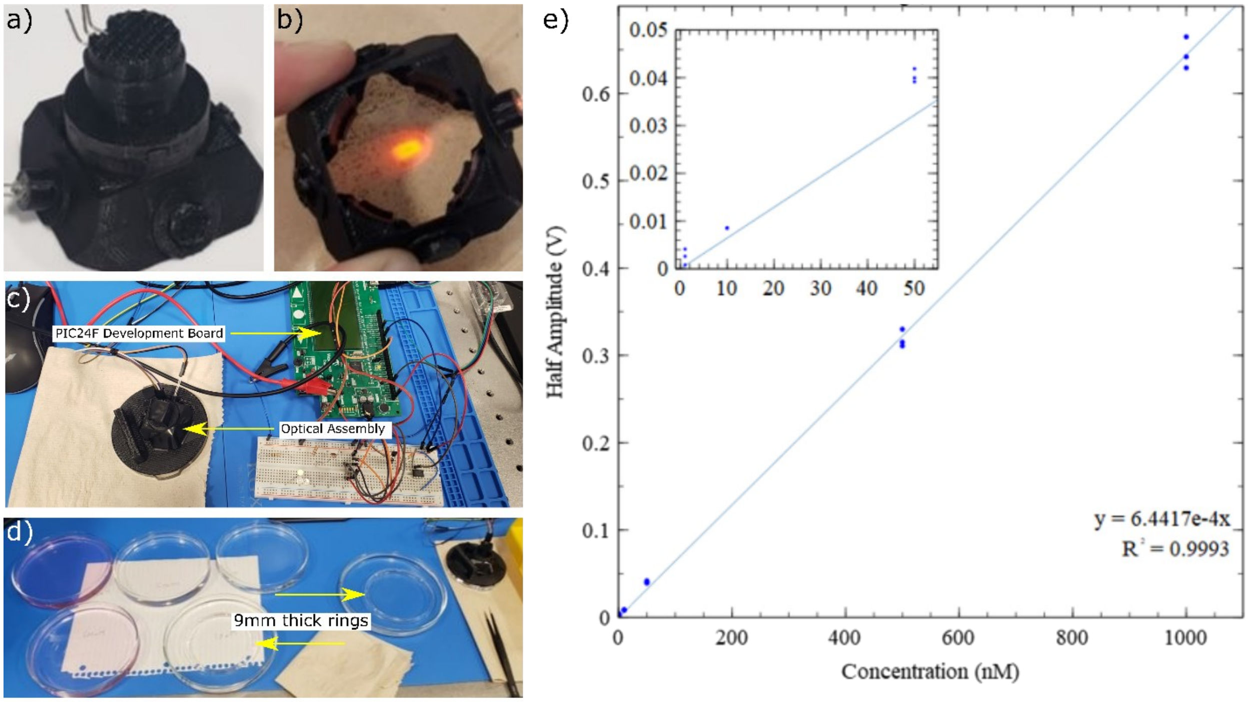

Figure 4.11: Preliminary benchtop testing of the optical layout using a development board. (a) Isometric view of a photo of the 3D print housing the optics. (b) Top-down photo of optical stack base without collimating components. This view exposes the LED path. It can be seen that the LED's rays are centered after passing through the acrylic plate. Notably the LED in this photo is not the one used when implemented, as it is the wrong wavelength. (c) Electrical setup for development board benchtop testing. (d) Petri dishes of various Rhodamine concentrations. (e) Calibration curve of Rhodamine concentrations vs amplitude. Inset plot displays lower concentrations.

This test was then repeated with the fully constructed device, which had its own electronics (the PCB) driving the device. In Figure 4.12 (a) the raw data of the output is shown; unlike the previous calibration this device was continuously taking measurements. The plateaus seen in Figure 4.12 (a) are the results of the sensor measuring a sample. The spikes on the sides of the plateaus are a result of moving the device and cleaning it. Notably, there are plateaus which do not make sense for the ladder pattern observed, this is the result of the blank becoming contaminated due to cleaning being insufficient. These anomalies were detected during testing and the blank sample would be replaced before resuming calibration. The results are shown in Figure 4.12 (b).

Again, a strong linearity is present. The slope of the curve is different than that of the previous calibration because of different LED intensities from the different hardware used; i.e. the BJT LED-driver versus the FET-driver described above.

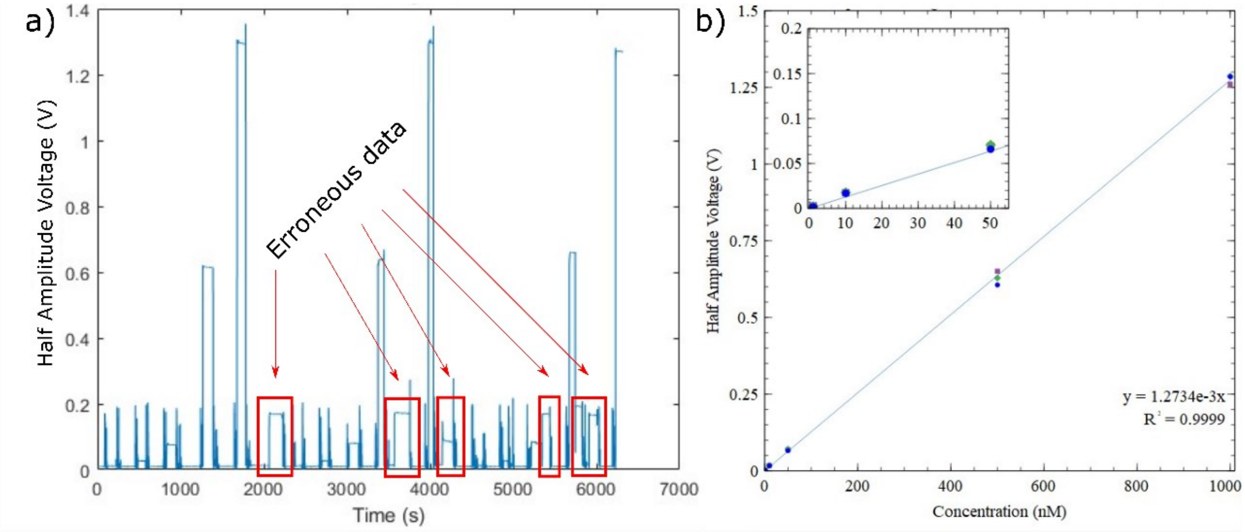

Figure 4.12: Benchtop initial calibration data. (a) Raw data from bench top calibration. (b) Processed calibration curve of amplitude vs concentration Rhodamine. Inset plot is of the lower concentrations.

Summarily, Chapter 4 has demonstrated that raytracing simulations permitted the design and realization of a sensitive fluorometer for nanomolar concentrations.

CHAPTER 5 CALIBRATION & FIELD TRIALS

The signal processing from Chapter 3 and the optical simulation from Chapter 4 have yielded a sensitive fluorometer. In this chapter, the novel prototype and two commercial fluorometers are calibrated across a wide range of temperatures. The chapter compares the performance of the developed sensor against the other two commercial fluorometers. Once calibrated, the developed sensor along with a commercial sensor were integrated with an ROV and a system integration test was done in Dalhousie's Aquatron. Lastly, field trials were performed in the Gulf of Saint Lawrence as part of the TReX project. Calibration and field testing was done in collaboration with Allison Chua and it was her ROV used for deployments.

5.1 Calibration

5.1.1 Temperature Calibration

Rhodamine WT 400ppb (Turner Designs, San Jose, CA, USA) was diluted to 0.5 ppb, 2 ppb, 10 ppb, 30 ppb, and 60 ppb using seawater from Dalhousie's Aquatron. Additionally, a sample of just seawater was used, 0 ppb. These concentrations were chosen because in past field deployments the observable range of Rhodamine WT was between 0.5 and 60 ppb.

These Rhodamine WT standards were measured using three sensors: the prototype sensor, a Turner Cyclops-7F (Turner Designs, San Jose, CA, USA), and an AML X2Change powered by Turner Designs (AML oceanographic, Dartmouth, NS, Canada). Figure 5.1 shows the setup used to calibrate. The prototype and AML fluorometers stream digital data, where the Turner fluorometer was analog and was measured with a multimeter (Model number 34460A, Keysight Technologies, Ontario Canada). The commercial sensors had 3 modes of sensitivity, x1, x10, and x100. For these calibrations, and later deployments, they were set to the x10 mode. Each standard, including the 0 ppb, was thermally cycled using a Lauda Eco Gold immersion thermostat (Lauda, Delran, NJ, USA) such that 5, 8, 11, 14, 17, and 20 °C was achieved. At each of these temperatures the thermal controller held the temperature such that each sensor could get five minutes of data at the held temperature. The temperature regulated bath was connected to a custom bath chamber which sufficiently suppressed ambient light as shown in Figure 5.1. The Rhodamine WT was contained in a 2L beaker, which was placed inside of the custom bath. The probe for monitoring the temperature was suspended in the 2L beaker. Each sensor was mounted such that they were submerged into the beaker, with the optical sensing portion facing the bottom of the beaker. It took approximately one hour for each temperature the be reached and settled. The measurements were talking serially, each time a sensor was switched out at a held temperature, some time was needed for the temperature to return to the desired temperature.

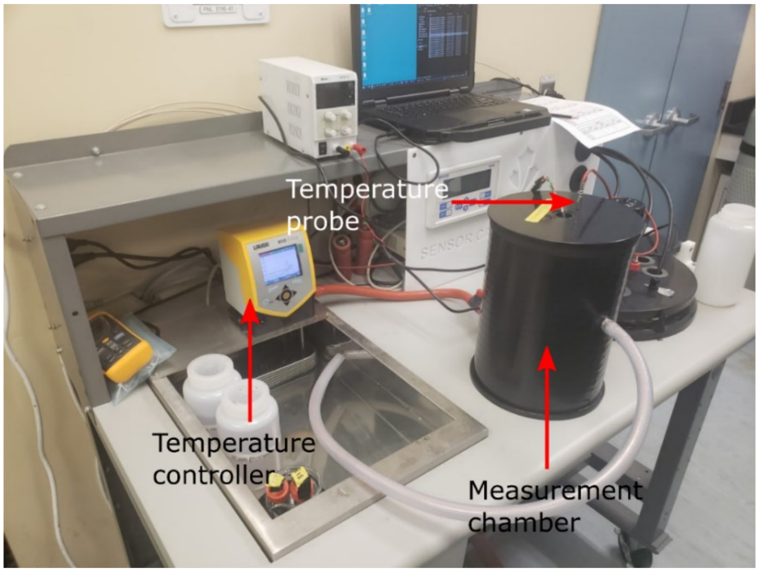

Figure 5.1: Temperature calibration setup.

The results of these calibrations are shown in Figure 5.2. Figure 5.2 (a) is a calibration curve of the prototype sensor, where each dataset is at a different temperature. The slopes of the linear fits from Figure 5.2 (a) were plotted in Figure 5.2 (b) and a linear fit to the slopes are used to temperature compensate. Figure 5.2 (c) is a plot of the linear fits' offset from Figure 5.2 (a). Similarly, Figure 5.2 (d – f) are of the AML fluorometer's calibration curves, slope curve and offset curve respectively and Figure 5.2 (g – i) are of the Turner fluorometer's calibration curves, slope curve and offset curve respectively.

Notably, the results of the prototype sensor do not match the simulations. For instance, at 30 ppb, simulations anticipated a voltage reading of 190 mV, whereas the experiment showed 62 mV at 20 °C. The results in Figure 5.2 use units of half amplitude (half peak-to-peak amplitude), while the simulations used DC measurements and full amplitude (peak-to-peak amplitude). Even when double, it does not account for the difference. However, the effects of seawater on rhodamine dye are known to decrease fluorescent yield over time [79]. The salinity, more specifically sodium and potassium chloride molar concentrations degrade the dye. Seawater is approximately 0.6 nM sodium chloride and so this would give an effective yield of 8.3% after 46 hours. Applying the effects of the seawater to the simulation data a new anticipated value of 16 mV for 30 ppb is found. To match simulation and experiment more exactingly, calibrations on Rhodamine in seawater could be conducted immediately after mixing, but the results are sufficient.

The results were then used to form temperature compensating equations for each fluorometer, the generic equation for each is described by equation 5.1.

$$V_T = \frac{V_{raw}}{\left(m_{slopes}T + b_{slopes}\right)} - \bar{x} \tag{5.1}$$

The result, V_T, is the temperature compensated voltage. The raw voltage from the fluorometer is V_{raw}. The slope of the slope plot of the respective fluorometer is m_{slopes}, were b_{slopes} is the offset for the same plot. The temperature is T. The average of the respective offset plot is $\bar{x}$. This equation is what is used when processing deployment data.

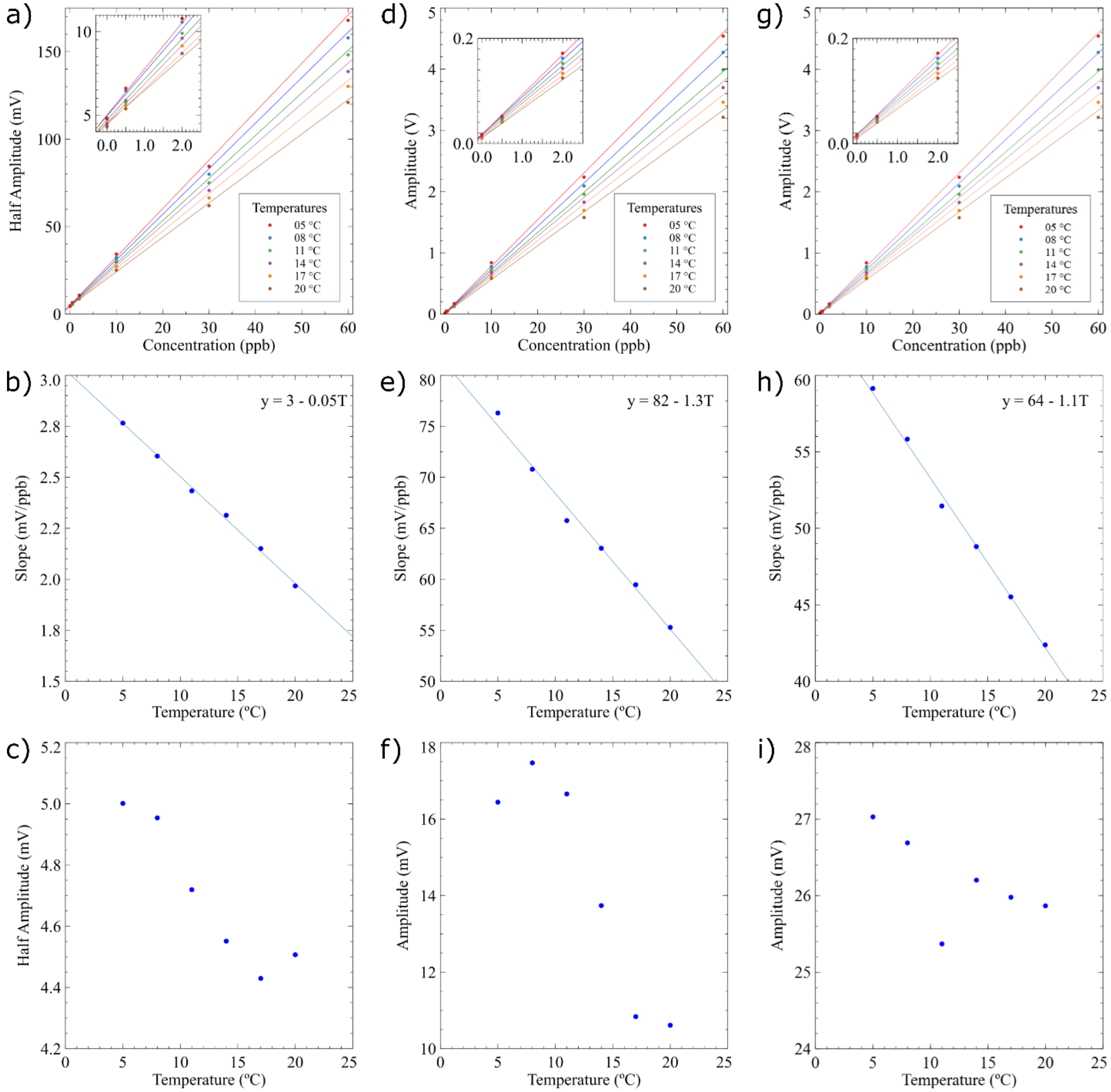

Figure 5.2: Temperature calibration curves for novel prototype, AML and Turner sensors. (a) Developed fluorometer calibration curves at various temperatures as indicated by the legend. Inset plot is of the lower concentrations. (b) Slopes from part a plotted. (c) Offsets from part a plotted. (d) AML fluorometer calibration curves at various temperatures as indicated by the legend. Inset plot is of lower concentrations. (e) Slopes from part d plotted. (f) Offsets from part d plotted. (g) Turner fluorometer calibration curves at various temperatures as indicated by the legend. Inset plot is of lower concentrations. (h) Slopes from part g plotted. (i) Offsets from part g plotted.

5.1.2 Precision

The relative standard deviation (RSD) from the data presented in Figure 5.2 (a) can be found in Table 5.1, similarly for the data presented in Figure 5.2 (d) in Table 5.2 and for the data presented in Figure 5.2 (g) in Table 5.3. A general trend can be observed, at lower temperatures and higher concentrations the RSD is lower, which is as expected because the fluorescence readings are stronger.

Table 5.1 Relative standard deviations on the prototype's calibration data.

	5 °C	8 °C	11 °C	14 °C	17 °C	20 °C
0 ppb	2.39	2.38	2.38	2.61	2.88	3.16
0.5 ppb	1.98	1.96	2.11	1.90	2.04	2.20
2 ppb	1.14	1.18	1.20	1.28	1.35	1.42
10 ppb	0.401	0.392	1.20	0.452	0.494	0.565
30 ppb	0.158	2.73	2.86	0.191	0.197	0.196
60 ppb	0.073	0.0773	0.0787	0.0848	0.0995	0.101

Table 5.2 Relative standard deviations on the AML's calibration data.

	5 °C	8 °C	11 °C	14 °C	17 °C	20 °C
0 ppb	6.90	7.17	6.11	7.58	9.58	10.2
0.5 ppb	2.02	2.11	2.30	2.22	2.48	2.89
2 ppb	0.635	0.688	0.731	0.740	0.794	0.861
10 ppb	0.133	0.141	0.150	0.159	0.171	0.207
30 ppb	0.0774	0.0724	0.0633	0.0771	0.0740	0.0728
60 ppb	0.0320	0.0852	0.0581	0.0821	0.0465	0.128

Table 5.3 Relative standard deviations on the Turner's calibration data.

	5 °C	8 °C	11 °C	14 °C	17 °C	20 °C
0 ppb	1.00	1.053	0.978	1.035	1.09	1.049
0.5 ppb	0.567	0.557	0.649	0.573	0.588	0.648
2 ppb	0.174	0.200	0.208	0.206	0.218	0.237
10 ppb	0.0501	0.0838	0.0829	0.168	0.193	0.126
30 ppb	0.0187	0.119	0.0406	0.0313	0.0390	0.142
60 ppb	0.0262	0.0166	0.0247	0.0256	0.0237	0.0136

Standard deviations were converted from volts to ppb by using equation 5.1; however, $\bar{x}$ is set to zero as the standard deviations would not have an offset. The lowest standard deviation of the prototype sensor was found to be 0.0488 ppb at 0.5 ppb and 14 °C, and its highest SD to be 0.837 ppb at 30.0 ppb and 8 °C. The lowest standard deviation of the AML sensor was found to be 0.0161 ppb at 0.5 ppb and 14 °C, and its highest SD to be 0.0749 ppb at 60.0 ppb and 20 °C. The lowest SD of the Turner sensor was found to be 0.00443 ppb at 2.0 ppb and 5 °C, and its highest SD to be 0.0368 ppb at 30.0 ppb and 8 °C.

5.1.3 Limits of Detection

LODs for each sensor at each temperature was determined using the SD of the 0 ppb measurements. The prototype had LODs ranging from 0.125 – 0.215 ppb. The AML device had LODs ranging from 0.046 – 0.0542 ppb. The Turner device had LODs ranging from 0.014 – 0.198 ppb. The LODs at each temperature can be found in Table 5.4. However, the limit of quantification (LOQ), which is ten times the SD as opposed to three times the SD (LOD), is often used to determine the lower limit of devices and can be found in Table 5.5. Notably the Turner device has the lowest LOQ, and the prototype has the highest. Although the prototype has the highest LOQ it is still on-par with the typical noise observed on previous deployments, ±0.5 ppb.

Table 5.4 Limit of detection of each sensor at each temperature.

LOD (ppb)	5 °C	8 °C	11 °C	14 °C	17 °C	20 °C
Prototype	0.125	0.130	0.148	0.149	0.174	0.215
AML	0.0460	0.0542	0.0473	0.0493	0.0519	0.0581
Turner	0.0140	0.0154	0.0152	0.0169	0.0192	0.0198

Table 5.5 Limit of quantification of each sensor at each temperature.

LOQ (ppb)	5 °C	8 °C	11 °C	14 °C	17 °C	20 °C
Prototype	0.416	0.434	0.462	0.496	0.579	0.718
AML	0.153	0.181	0.158	0.164	0.173	0.194
Turner	0.0466	0.0514	0.0507	0.0565	0.0639	0.0661

5.2 Aquatron Testing

Prior to field deployments a systems integration test was performed in Dalhousie's Aquatron. The prototype fluorometer was mounted to a blueROV as shown in Figure 5.3 (a), along with the AML fluorometer (photo courtesy: Allison Chua). Both fluorometers are facing in the downwards direction in reference to the ROV's orientation. The ROV was deployed in Dalhousie's Aquatron, a 285 m^3 tank of seawater. While the ROV was in the tank approximately 7 mL of 20% Rhodamine WT dye (Turner Designs, San Jose, CA, USA) was injected into the tank. The ROV was then arbitrarily driven through the plume.

The results of this test are shown in Figure 5.3 (b). A comparison between the sensors for this test is shown in Figure 5.3 (c), where a unity curve of the two can be found. The ROV was then removed from the tank and the tank was cycled such that the Rhodamine WT concentrations became uniform throughout the tank. The ROV was then reintroduced to the tank and a second doping of Rhodamine WT was introduced. Similarly, the ROV was driven through the plume and the data from the fluorometers can be found in Figure 5.3 (d). A unity curve of the fluorometers after the second doping is shown in Figure 5.3 (e).

Looking at the data a trend can be observed. While the ROV is driving through the plume the sensor readings vary significantly; however, in relatively homogenous solution the sensors agree. This is occurring most likely because the sensors are approximately 11.5 cm apart and the viscous plume can have high concentration gradients, meaning that each sensor would be measuring a different concentration. However, during low concentration gradients the sensors have a high correlation because they would be measuring similar, if not the same concentration.

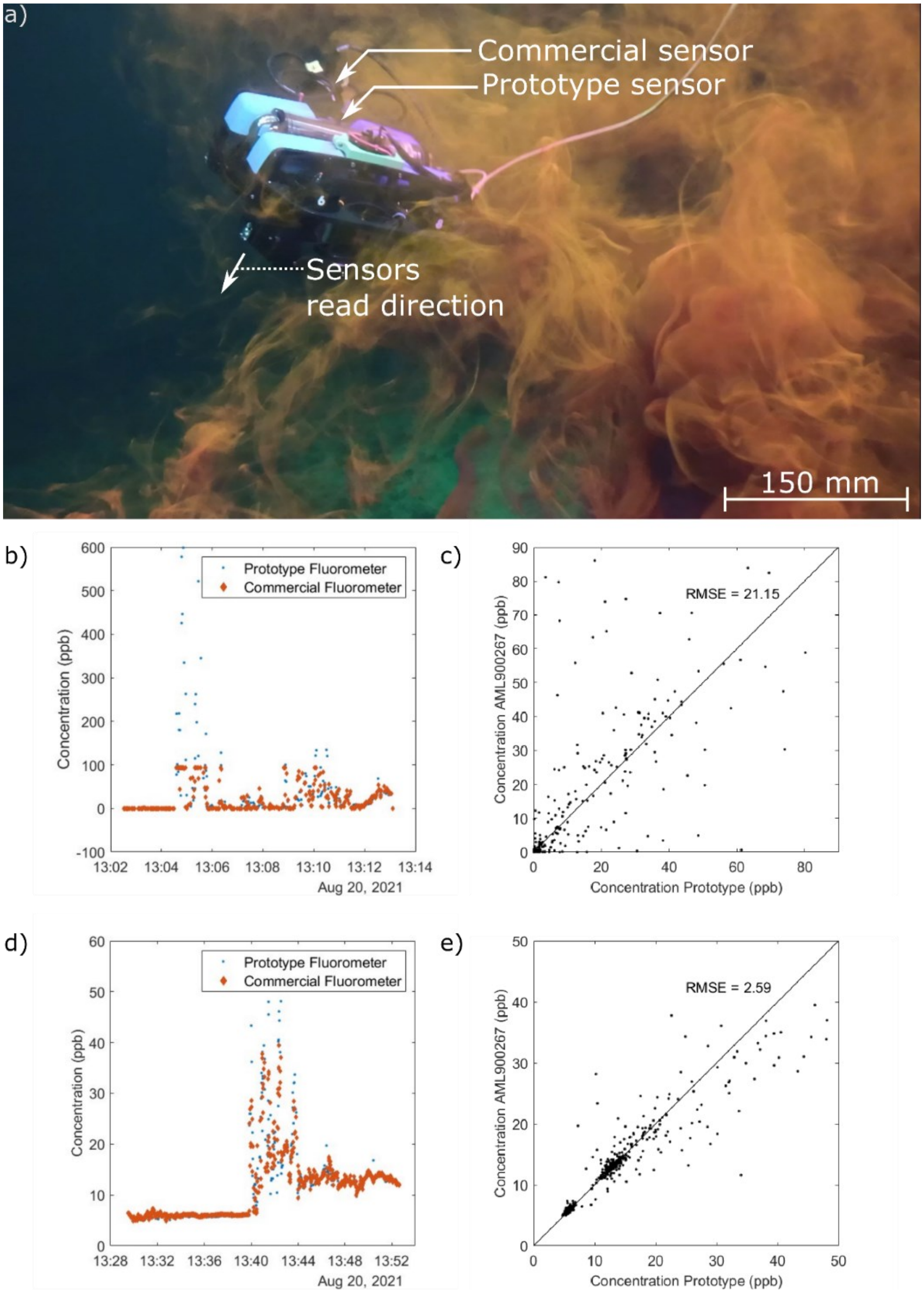

Figure 5.3: ROV testing in Dalhousie's Aquatron. (a) Picture of the ROV with both the prototype and commercial sensors being piloted through a Rhodamine plume in Dalhousie's Aquatron. Image taken by Allison Chua. (b) Concentration of Rhodamine vs time for both sensors after the first Rhodamine doping. (c) A unity curve of the commercial sensor vs the prototype from part (b). (d) Concentration of Rhodamine vs time for both sensors after the second Rhodamine doping. (e) A unity curve of the commercial sensor vs the prototype from part (d).

5.3 TReX Field Data

The Tracer Release Experiment (TReX) is a field and modelling experiment focused on dispersion observation and forecasting abilities. The TReX project is co-funded by MEOPAR and RQM and is a multi-group effort ranging from government to academia to communities. My part of the project was to develop and demonstrate a low-cost fluorometer suitable for Rhodamine tracer experiments in the Gulf of Saint Lawrence. The TReX deployments occurred on the 5th – 9th of September 2021. Each day 300L of 1% Rhodamine WT was dispensed over approximately 4 minutes into the Gulf of Saint Lawrence, just north of Rimouski, 48°35’01.0”N 68°31’08.8”W around noon. With an exception on the 9th where 900L of 0.44% Rhodamine WT was dispensed over approximately 6 minutes. Data was collected on the same ROV used in the Aquatron testing. The prototype fluorometer was used along with a Turner Series Cyclops F7 analog fluorometer. Data was collected on each day except for the 7th due to weather.

Figure 5.4 presents data acquired on the 5th day of September 2021. Figure 5.4 (a) plots 3 sets of data, the prototype sensor’s fluorescence, the Turner Cyclops’ fluorescence, and the ROV’s temperature log. There are also images inset onto the plot from the ROV’s front facing camera. When comparing the fluorometer data to the camera images a trend can be observed. During high peaks the images show visible Rhodamine plumes and during low reported concentrations the seawater is a grey/green color which indicates a lack of Rhodamine. When comparing the two sensors, both datasets follow the same pattern, although they do not perfectly match. This may be due to the physical distance between the sensors, as observed in the Aquatron testing in the preceding section. In Figure 5.4 (b) the depth of the ROV can be found, along with an inset map of where the deployment was performed. Ultimately, this field test displays the success in this project, validating the design efforts that yielded a sensitive fluorometer for marine environments.

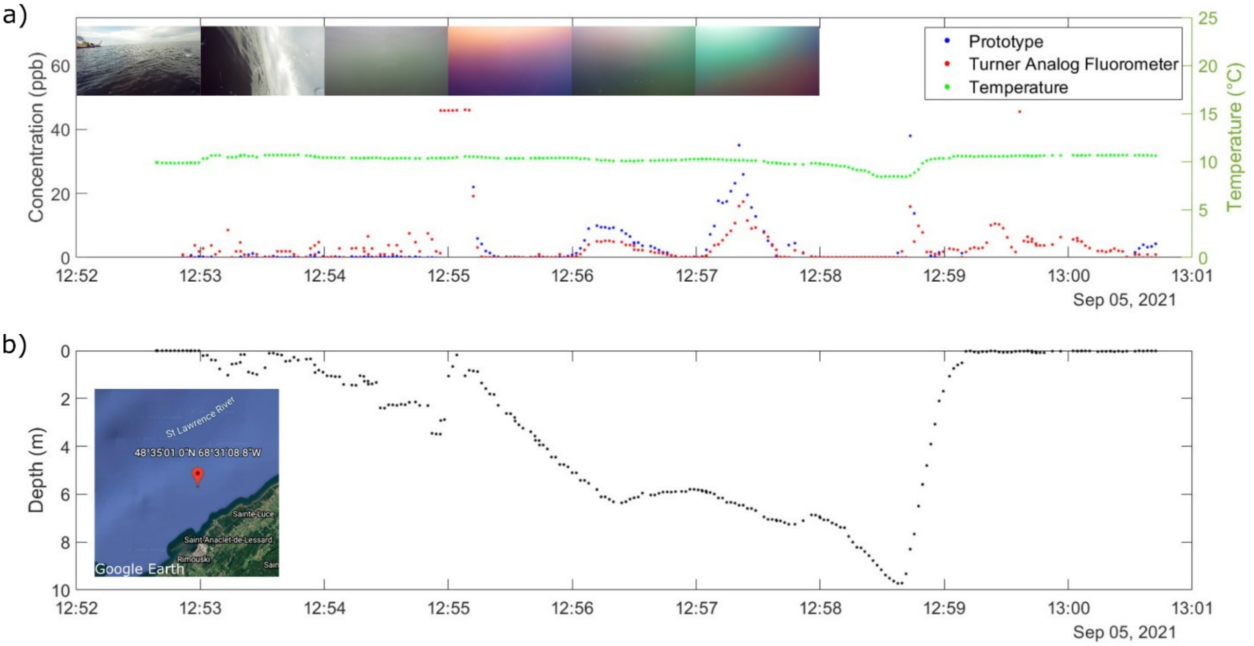

Figure 5.4: TReX deployment data 5-Sept-2021. (a) Plot of concentration Rhodamine vs time and temperature vs time. Both fluorometer's data are presented, the blue series for the prototype and red for the commercial sensor. The temperature is plotted in green. Inset are images from the ROV's front facing camera in 1-minute intervals. (b) A depth vs time plot of the ROV. Inset is a map with the coordinates for where the ROV was deployed.

CHAPETER 6 CONCLUSION

6.1 Summary

The purpose of this thesis was to develop a microfluidic fluorescence spectroscopy approach that can be integrated with other lab-on-chip technologies for performing a variety of measurements underwater that are reagent efficient. In Chapter 2 the development of a novel microfluidic inlaid approach for performing fluorescence measurements on-chip was discussed. The limit of detection of this chip, 47 nM (27 ppb) Rhodamine, required improvement for many applications, so a deep-dive into the sub-systems comprised the remainder of this thesis. In Chapter 3 signal processing aimed to achieve a better limit of detection discusses the digital lock-in amplifier that was simulated and developed. In Chapter 4 ray tracing simulations which optimized an optical layout are discussed followed by the construction and preliminary benchtop testing of the fluorometer. In Chapter 5 the developed low-cost and high performance fluorometer is compared to commercial sensors. The developed sensor was temperature calibrated along with the commercial sensors and was found to have a limit of detection of 0.39 nM (0.22 ppb) at 20 °C, an improvement of 120-fold compared to the microfluidic approach. Lastly, the developed fluorometer discussed in Chapter 5 was deployed along side the commercial sensor, Turner Designs Cyclops 7, on a ROV in the Gulf of Saint Lawrence for the TReX project. Ultimately, the developed sensor had been validated as a low-cost and sensitive fluorometer for marine environments.

6.2 Future Directions

The submersible fluorometer was a great success and should be integrated with an LOC design. The signal processing and optical technology developed can be applied to a microfluidic approach. An advantage of the LOC approach is that it can be integrated into a larger microfluidic system, for example, an eDNA sampler. An eDNA sampler filters water from the environment and collects genetic material on filter membranes. It would be advantageous to integrate a fluorometer on the front end of this sampler to perform active filtration. A fluorometer could detect the fluorescent pigments of microbes and use this information to determine if it is worth filtering from the environment. For example if no fluorescence is detected the sampler could determine not to sample saving power and reducing any waste products.

Even without LOC technology there are several avenues to take. Other commercial fluorometers, for example the Turner Designs C3 and C6 can have multiple channels for measuring multiple fluorescent species. Multiple channels can be useful in differentiating species that may have similar spectra and or is useful to have a single sensor analyzing multiple species. Other sensors using fluorescence technology can measure pH, CO_2 and O_2 given phaser information which the lock-in amplifier provides and an optode. These measurements are increasingly important as they are important to understanding climate change. I anticipate the work that this thesis presents will enable numerous future projects.

REFERENCES

[1] U. Noomnarm and R. M. Clegg, “Fluorescence lifetimes: fundamentals and interpretations,” *Photosynth. Res.*, vol. 101, no. 2–3, pp. 181–194, Sep. 2009, doi: 10.1007/s11120-009-9457-8.

[2] P. P. Mondal and A. Diaspro, “Molecular Physics of Fluorescent Markers,” 2014.

[3] N. Shanker and S. Bane, “Basic Aspects of Absorption and Fluorescence Spectroscopy and Resonance Energy Transfer Methods,” *Methods Cell Biol.*, vol. 84, pp. 213–42, Feb. 2008, doi: 10.1016/S0091-679X(07)84008-8.

[4] D. E. Wolf, “Fundamentals of fluorescence and fluorescence microscopy,” *Methods Cell Biol.*, vol. 114, pp. 69–97, 2013, doi: 10.1016/B978-0-12-407761-4.00004-X.

[5] T. K. CHRISTOPOULOS and E. P. DIAMANDIS, “14 - FLUORESCENCE IMMUNOASSAYS,” in *Immunoassay*, E. P. Diamandis and T. K. Christopoulos, Eds. San Diego: Academic Press, 1996, pp. 309–335. doi: 10.1016/B978-012214730-2/50015-7.

[6] J. Prakash and A. K. Mishra, “White light excitation fluorescence (WLEF) : Part I. Exploring the use in analytical fluorimetry,” *Anal Methods*, vol. 3, no. 2, pp. 362–367, 2011, doi: 10.1039/C0AY00703J.

[7] “Selecting Optical Filters for Fluorescence Microscopy—Note 23.2 - CA.” https://www.thermofisher.com/ca/en/home/references/molecular-probes-the-handbook/technical-notes-and-product-highlights/selecting-optical-filters-for-fluorescence-microscopy.html (accessed Dec. 07, 2020).

[8] J. J. Creelman, E. A. Luy, G. C. H. Beland, C. Sonnichsen, and V. J. Sieben, “Simultaneous Absorbance and Fluorescence Measurements Using an Inlaid Microfluidic Approach,” *Sensors*, vol. 21, no. 18, 2021, doi: 10.3390/s21186250.

[9] S. A. Jaywant and K. M. Arif, “A Comprehensive Review of Microfluidic Water Quality Monitoring Sensors,” *Sensors*, vol. 19, no. 21, 2019, doi: 10.3390/s19214781.

[10] M. F. Khanfar, W. Al-Faqheri, and A. Al-Halhouli, “Low Cost Lab on Chip for the Colorimetric Detection of Nitrate in Mineral Water Products,” *Sensors*, vol. 17, no. 10, Oct. 2017, doi: 10.3390/s17102345.

[11] A. D. Beaton *et al.*, “Lab-on-Chip Measurement of Nitrate and Nitrite for In Situ Analysis of Natural Waters,” *Environ. Sci. Technol.*, vol. 46, no. 17, pp. 9548–9556, Sep. 2012, doi: 10.1021/es300419u.

[12] M. M. Grand *et al.*, “A Lab-On-Chip Phosphate Analyzer for Long-term In Situ Monitoring at Fixed Observatories: Optimization and Performance Evaluation in Estuarine and Oligotrophic Coastal Waters,” *Front. Mar. Sci.*, vol. 4, 2017, doi: 10.3389/fmars.2017.00255.

[13] F.-E. Legiret *et al.*, “A high performance microfluidic analyser for phosphate measurements in marine waters using the vanadomolybdate method,” *Talanta*, vol. 116, pp. 382–387, Nov. 2013, doi: 10.1016/j.talanta.2013.05.004.

[14] G. S. Clinton-Bailey *et al.*, “A Lab-on-Chip Analyzer for in Situ Measurement of Soluble Reactive Phosphate: Improved Phosphate Blue Assay and Application to Fluvial Monitoring,” *Environ. Sci. Technol.*, vol. 51, no. 17, pp. 9989–9995, Sep. 2017, doi: 10.1021/acs.est.7b01581.

[15] O. Tokel *et al.*, “Portable Microfluidic Integrated Plasmonic Platform for Pathogen Detection,” *Sci. Rep.*, vol. 5, no. 1, p. 9152, Mar. 2015, doi: 10.1038/srep09152.

[16] H. Wang, Y. Li, J. Wei, J. Xu, Y. Wang, and G. Zheng, “Paper-based three-dimensional microfluidic device for monitoring of heavy metals with a camera cell phone,” *Anal. Bioanal. Chem.*, vol. 406, no. 12, pp. 2799–2807, May 2014, doi: 10.1007/s00216-014-7715-x.

[17] W. Chen, X. Fang, H. Li, H. Cao, and J. Kong, “A Simple Paper-Based Colorimetric Device for Rapid Mercury(II) Assay,” *Sci. Rep.*, vol. 6, no. 1, p. 31948, Aug. 2016, doi: 10.1038/srep31948.

[18] C. Fan, S. He, G. Liu, L. Wang, and S. Song, "A portable and power-free microfluidic device for rapid and sensitive lead (Pb2+) detection," *Sensors*, vol. 12, no. 7, pp. 9467–9475, 2012, doi: 10.3390/s120709467.

[19] A. Gencoglu and A. R. Minerick, "Electrochemical detection techniques in micro- and nanofluidic devices," *Microfluid. Nanofluidics*, vol. 17, no. 5, pp. 781–807, Nov. 2014, doi: 10.1007/s10404-014-1385-z.

[20] I. B. Obot, I. B. Onyeachu, A. Zeino, and S. A. Umoren, "Electrochemical noise (EN) technique: review of recent practical applications to corrosion electrochemistry research," *J. Adhes. Sci. Technol.*, vol. 33, no. 13, pp. 1453–1496, Jul. 2019, doi: 10.1080/01694243.2019.1587224.

[21] B. Kuswandi, Nuriman, J. Huskens, and W. Verboom, "Optical sensing systems for microfluidic devices: A review," *Anal. Chim. Acta*, vol. 601, no. 2, pp. 141–155, Oct. 2007, doi: 10.1016/j.aca.2007.08.046.

[22] M. A. Borowitzka, "Chapter 3 - biology of microalgae," in *Microalgae in health and disease prevention*, I. A. Levine and J. Fleurence, Eds. Academic Press, 2018, pp. 23–72. doi: https://doi.org/10.1016/B978-0-12-811405-6.00003-7.

[23] J. Fleurence and I. A. Levine, "Chapter 14 - Antiallergic and Allergic Properties," in *Microalgae in Health and Disease Prevention*, I. A. Levine and J. Fleurence, Eds. Academic Press, 2018, pp. 307–315. doi: 10.1016/B978-0-12-811405-6.00014-1.

[24] R. Beck *et al.*, "Comparison of Satellite Reflectance Algorithms for Estimating Phycocyanin Values and Cyanobacterial Total Biovolume in a Temperate Reservoir Using Coincident Hyperspectral Aircraft Imagery and Dense Coincident Surface Observations," *Remote Sens.*, vol. 9, p. 538, May 2017, doi: 10.3390/rs9060538.

[25] R. P. Stumpf *et al.*, "Challenges for mapping cyanotoxin patterns from remote sensing of cyanobacteria," *Harmful Algae*, vol. 54, pp. 160–173, Apr. 2016, doi: 10.1016/j.hal.2016.01.005.

[26] J. M. Clark *et al.*, "Satellite monitoring of cyanobacterial harmful algal bloom frequency in recreational waters and drinking source waters," *Ecol. Indic.*, vol. 80, pp. 84–95, Sep. 2017, doi: 10.1016/j.ecolind.2017.04.046.

[27] M. Morançais, J.-L. Mouget, and J. Dumay, "Chapter 7 - Proteins and Pigments," in *Microalgae in Health and Disease Prevention*, I. A. Levine and J. Fleurence, Eds. Academic Press, 2018, pp. 145–175. doi: 10.1016/B978-0-12-811405-6.00007-4.

[28] W. W. Carmichael, "Cyanobacteria secondary metabolites—the cyanotoxins," *J. Appl. Bacteriol.*, vol. 72, no. 6, pp. 445–459, Jun. 1992, doi: 10.1111/j.1365-2672.1992.tb01858.x.

[29] H. W. Paerl and T. G. Otten, "Harmful Cyanobacterial Blooms: Causes, Consequences, and Controls," *Microb. Ecol.*, vol. 65, no. 4, pp. 995–1010, May 2013, doi: 10.1007/s00248-012-0159-y.

[30] S. Bhattacharjee and T. Dutta, "Chapter 1 - An overview of oil pollution and oil-spilling incidents," in *Advances in Oil-Water Separation*, P. Das, S. Manna, and J. K. Pandey, Eds. Elsevier, 2022, pp. 3–15. doi: 10.1016/B978-0-323-89978-9.00014-8.

[31] R. N. Conmy *et al.*, "Submersible Optical Sensors Exposed to Chemically Dispersed Crude Oil: Wave Tank Simulations for Improved Oil Spill Monitoring," *Environ. Sci. Technol.*, vol. 48, no. 3, pp. 1803–1810, Feb. 2014, doi: 10.1021/es404206y.

[32] A. Vasilijevic, N. Stilinovic, D. Nad, F. Mandic, N. Miskovic, and Z. Vukic, "AUV based mobile fluorometers: System for underwater oil-spill detection and quantification," in *2015 IEEE Sensors Applications Symposium (SAS)*, Apr. 2015, pp. 1–6. doi: 10.1109/SAS.2015.7133650.

[33] E. A. Luy, S. C. Morgan, J. J. Creelman, B. J. Murphy, and V. J. Sieben, "Inlaid microfluidic optics: absorbance cells in clear devices applied to nitrite and phosphate detection," *J. Micromechanics Microengineering*, vol. 30, no. 9, p. 095001, Jun. 2020, doi: 10.1088/1361-6439/ab9202.

[34] C. M. Preston *et al.*, "Underwater Application of Quantitative PCR on an Ocean Mooring," *PLOS ONE*, vol. 6, no. 8, p. e22522, Aug. 2011, doi: 10.1371/journal.pone.0022522.

[35] H. Macintyre, E. Lawrenz, and T. Richardson, “Taxonomic Discrimination of Phytoplankton by Spectral Fluorescence,” in *Chlorophyll a Fluorescence in Aquatic Sciences: Methods and Applications*, 1970, pp. 129–169. doi: 10.1007/978-90-481-9268-7_7.

[36] H. L. MacIntyre, J. J. Cullen, T. J. Whitsitt, and B. Petri, “Enumerating viable phytoplankton using a culture-based Most Probable Number assay following ultraviolet-C treatment,” *J. Appl. Phycol.*, vol. 30, no. 2, pp. 1073–1094, Apr. 2018, doi: 10.1007/s10811-017-1254-8.

[37] H. Macintyre and J. Cullen, “Classification of phytoplankton cells as live or dead using the vital stains fluorescein diacetate and 5-chloromethylfluorescein diacetate (FDA and CMFDA),” *J. Phycol.*, vol. 52, p. n/a-n/a, Mar. 2016, doi: 10.1111/jpy.12415.

[38] M. Morançais, J.-L. Mouget, and J. Dumay, “Chapter 7 - Proteins and Pigments,” in *Microalgae in Health and Disease Prevention*, I. A. Levine and J. Fleurence, Eds. Academic Press, 2018, pp. 145–175. doi: 10.1016/B978-0-12-811405-6.00007-4.

[39] J. W. K. Kok, D. C. J. Yeo, and S. C. Y. Leong, “Growth, pigment, and chromophoric dissolved organic matter responses of tropical Chattonella subsalsa (Raphidophyceae) to nitrogen enrichment,” *Phycol. Res.*, vol. 67, no. 2, pp. 134–144, Apr. 2019, doi: 10.1111/pre.12360.

[40] J. Para, P. G. Coble, B. Charrière, M. Tedetti, C. Fontana, and R. Sempéré, “Fluorescence and absorption properties of chromophoric dissolved organic matter (CDOM) in coastal surface waters of the northwestern Mediterranean Sea, influence of the Rhône River,” *Biogeosciences*, vol. 7, no. 12, pp. 4083–4103, 2010, doi: 10.5194/bg-7-4083-2010.

[41] N. B. Nelson and J. M. Gauglitz, “Optical Signatures of Dissolved Organic Matter Transformation in the Global Ocean,” *Front. Mar. Sci.*, vol. 2, p. 118, 2016, doi: 10.3389/fmars.2015.00118.

[42] J. E. Birdwell and A. S. Engel, “Characterization of dissolved organic matter in cave and spring waters using UV–Vis absorbance and fluorescence spectroscopy,” *Org. Geochem.*, vol. 41, no. 3, pp. 270–280, Mar. 2010, doi: 10.1016/j.orggeochem.2009.11.002.

[43] Z. Xiaoling, Y. Gaofang, Z. Nanjing, Y. Ruifang, L. Jianguo, and L. Wenqing, “Chromophoric dissolved organic matter influence correction of algal concentration measurements using three-dimensional fluorescence spectra,” *Spectrochim. Acta. A. Mol. Biomol. Spectrosc.*, vol. 210, pp. 405–411, Mar. 2019, doi: 10.1016/j.saa.2018.10.050.

[44] P. D. Ohlsson, O. Ordeig, K. B. Mogensen, and J. P. Kutter, “Electrophoresis microchip with integrated waveguides for simultaneous native UV fluorescence and absorbance detection,” *ELECTROPHORESIS*, vol. 30, no. 24, pp. 4172–4178, 2009, doi: https://doi.org/10.1002/elps.200900393.

[45] S. Hengoju *et al.*, “Optofluidic detection setup for multi-parametric analysis of microbiological samples in droplets,” *Biomicrofluidics*, vol. 14, no. 2, p. 024109, Mar. 2020, doi: 10.1063/1.5139603.

[46] T. Yang, S. Stavrakis, and A. deMello, “A High-Sensitivity, Integrated Absorbance and Fluorescence Detection Scheme for Probing Picoliter-Volume Droplets in Segmented Flows,” *Anal. Chem.*, vol. 89, no. 23, pp. 12880–12887, Dec. 2017, doi: 10.1021/acs.analchem.7b03526.

[47] Y. Yamada, F. Hanawa, T. Kitoh, and T. Maruno, “Low-loss and stable fiber-to-waveguide connection utilizing UV curable adhesive,” *IEEE Photonics Technol. Lett.*, vol. 4, no. 8, pp. 906–908, Aug. 1992, doi: 10.1109/68.149904.

[48] C. F. A. Floquet *et al.*, “Nanomolar detection with high sensitivity microfluidic absorption cells manufactured in tinted PMMA for chemical analysis,” *Talanta*, vol. 84, no. 1, pp. 235–239, Mar. 2011, doi: 10.1016/j.talanta.2010.12.026.

[49] A. Milani, P. Statham, M. Mowlem, and D. Connelly, “Development and application of a microfluidic in-situ analyzer for dissolved Fe and Mn in natural waters,” *Talanta*, vol. 136, pp. 15–22, Jan. 2015, doi: 10.1016/j.talanta.2014.12.045.

[50] E. A. Luy, S. C. Morgan, J. J. Creelman, B. J. Murphy, and V. J. Sieben, “Inlaid microfluidic optics: absorbance cells in clear devices applied to nitrite and phosphate detection,” *J. Micromechanics Microengineering*, vol. 30, no. 9, p. 15, 2020, doi: 10.1088/1361-6439/ab9202.

[51] V. J. Sieben, C. F. A. Floquet, I. R. G. Ogilvie, M. C. Mowlem, and H. Morgan, “Microfluidic colourimetric chemical analysis system: Application to nitrite detection,” *Anal. Methods*, vol. 2, no. 5, pp. 484–491, 2010, doi: 10.1039/C002672G.

[52] C. M. Rushworth, G. Jones, M. Fischlechner, E. Walton, and H. Morgan, “On-chip cavity-enhanced absorption spectroscopy using a white light-emitting diode and polymer mirrors,” *Lab. Chip*, vol. 15, no. 3, pp. 711–717, 2015, doi: 10.1039/C4LC01264J.

[53] I. R. G. Ogilvie, V. J. Sieben, C. F. A. Floquet, R. Zmijan, M. C. Mowlem, and H. Morgan, “Solvent processing of PMMA and COC chips for bonding devices with optical quality surfaces,” 2010.

[54] H. Becker and C. Gärtner, “Polymer microfabrication methods for microfluidic analytical applications,” *ELECTROPHORESIS*, vol. 21, no. 1, pp. 12–26, Jan. 2000, doi: 10.1002/(SICI)1522-2683(20000101)21:1<12::AID-ELPS12>3.0.CO;2-7.

[55] V. J. Sieben, C. F. A. Floquet, I. R. G. Ogilvie, M. C. Mowlem, and H. Morgan, “Microfluidic colourimetric chemical analysis system: Application to nitrite detection,” *Anal. Methods*, vol. 2, no. 5, p. 484, 2010, doi: 10.1039/c002672g.

[56] M. Grumann *et al.*, *Optical beam guidance in monolithic polymer chips for miniaturized colorimetric assays*. 2005, p. 111. doi: 10.1109/MEMSYS.2005.1453879.

[57] L. Yuan, W. Lin, Y. Yang, and H. Chen, “A Unique Class of Near-Infrared Functional Fluorescent Dyes with Carboxylic-Acid-Modulated Fluorescence ON/OFF Switching: Rational Design, Synthesis, Optical Properties, Theoretical Calculations, and Applications for Fluorescence Imaging in Living Animals,” *J. Am. Chem. Soc.*, vol. 134, no. 2, pp. 1200–1211, Jan. 2012, doi: 10.1021/ja209292b.

[58] M. Taniguchi and J. Lindsey, “Database of Absorption and Fluorescence Spectra of >300 Common Compounds for use in PhotochemCAD,” *Photochem. Photobiol.*, vol. 94, Nov. 2017, doi: 10.1111/php.12860.

[59] A. Shrivastava, “Methods for the determination of limit of detection and limit of quantitation of the analytical methods,” *Chron. Young Sci.*, vol. 2, pp. 21–25, Jun. 2011, doi: 10.4103/2229-5186.79345.

[60] B. Murphy, E. Luy, K. Panzica, G. Johnson, and V. Sieben, “An Energy Efficient Thermally Regulated Optical Spectroscopy Cell for Lab-on-Chip Devices: Applied to Nitrate Detection,” *Micromachines*, vol. 12, p. 861, Jul. 2021, doi: 10.3390/mi12080861.

[61] P. R. Jonsson, H. Pavia, and G. Toth, “Formation of harmful algal blooms cannot be explained by allelopathic interactions,” *Proc. Natl. Acad. Sci.*, vol. 106, no. 27, pp. 11177–11182, Jul. 2009, doi: 10.1073/pnas.0900964106.

[62] A. Banerjee, Y. Shuai, R. Dixit, I. Papautsky, and D. Klotzkin, “Concentration dependence of fluorescence signal in a microfluidic fluorescence detector,” *J. Lumin.*, vol. 130, no. 6, pp. 1095–1100, Jun. 2010, doi: 10.1016/j.jlumin.2010.02.002.

[63] A. Pais, A. Banerjee, D. Klotzkin, and I. Papautsky, “High-sensitivity, disposable lab-on-a-chip with thin-film organic electronics for fluorescence detection,” *Lab. Chip*, vol. 8, no. 5, pp. 794–800, 2008, doi: 10.1039/B715143H.

[64] J. W. Dewdney, Ed., “Lock-in Amplifiers,” *Am. J. Phys.*, vol. 32, no. 6, pp. vii–viii, Jun. 1964, doi: 10.1119/1.1970754.

[65] K. W. Lamers, “‘Do-it-yourself’ lock-in amplifiers - radio and audio frequencies,” *Nucl. Instrum. Methods*, vol. 49, no. 1, pp. 165–169, Mar. 1967, doi: 10.1016/0029-554X(67)90679-9.

[66] Gary. Horlick and K. R. Betty, “Inexpensive lock-in amplifiers based on integrated circuit phase-locked loops,” *Anal. Chem.*, vol. 47, no. 2, pp. 363–366, Feb. 1975, doi: 10.1021/ac60352a001.

[67] D. C. Dening, “Simulation of a digital lock-in amplifier,” *J. Magn. Reson. 1969*, vol. 23, no. 3, pp. 461–463, Sep. 1976, doi: 10.1016/0022-2364(76)90279-1.

[68] A. Gökmen, A. Ulgen, and Ş. Yalçin, “A photon counting dynamic digital lock-in amplifier for background suppression in glow discharge atomic emission spectrometry,” *Spectrochim. Acta Part B At. Spectrosc.*, vol. 51, no. 1, pp. 97–108, Jan. 1996, doi: 10.1016/0584-8547(95)01407-1.

[69] J. Gaspar, S. F. Chen, A. Gordillo, M. Hepp, P. Ferreyra, and C. Marqués, “Digital lock in amplifier: study, design and development with a digital signal processor,” *Microprocess. Microsyst.*, vol. 28, no. 4, pp. 157–162, May 2004, doi: 10.1016/j.micpro.2003.12.002.

[70] M. O. Sonnaillon, R. Urteaga, F. J. Bonetto, and M. Ordonez, “Implementation of a high-frequency digital lock-in amplifier,” in *Canadian Conference on Electrical and Computer Engineering, 2005.*, May 2005, pp. 1229–1232. doi: 10.1109/CCECE.2005.1557199.

[71] S. Bhattacharyya, Ragib Nasir Ahmed, B. B. Purkayastha, and K. Bhattacharyya, “Implementation of Digital Lock-in Amplifier,” *J. Phys. Conf. Ser.*, vol. 759, no. 1, Oct. 2016, doi: 10.1088/1742-6596/759/1/012096.

[72] J. Sinlapanuntakul, P. Kijamnajsuk, C. Jetjamnong, and S. Chotikaprakhan, “Digital lock-in amplifier based on soundcard interface for physics laboratory,” *J. Phys. Conf. Ser.*, vol. 901, no. 1, Sep. 2017, doi: 10.1088/1742-6596/901/1/012065.

[73] G. L. Jiang, H. Yang, R. Li, and P. Kong, “A new algorithm for a high-modulation frequency and high-speed digital lock-in amplifier,” *Meas. Sci. Technol.*, vol. 27, no. 1, p. 015701, Jan. 2016, doi: 10.1088/0957-0233/27/1/015701.

[74] A. De Marcellis, E. Palange, N. Liberatore, and S. Mengali, “Low-Cost Portable 1MHz Lock-In Amplifier for Fast Measurements of Pulsed Signals in Sensing Applications,” *IEEE Sens. Lett.*, vol. PP, Jun. 2017, doi: 10.1109/LSENS.2017.2713449.

[75] G. Gervasoni, M. Carminati, and G. Ferrari, “FPGA-based lock-in amplifier with sub-ppm resolution working up to 6 MHz,” in *2016 IEEE International Conference on Electronics, Circuits and Systems (ICECS)*, Dec. 2016, pp. 117–120. doi: 10.1109/ICECS.2016.7841146.

[76] S. Hoang, J. Crawford, D. Doting, S. Florea, and F. S. Monsef, “Submersible apparatus for measuring active fluorescence,” 7470917 [Online]. Available: https://patents.justia.com/patent/7470917

[77] D. Magde, G. E. Rojas, and P. G. Seybold, “Solvent Dependence of the Fluorescence Lifetimes of Xanthene Dyes,” *Photochem. Photobiol.*, vol. 70, 1999.

[78] L. Yuan, W. Lin, Y. Yang, and H. Chen, “A Unique Class of Near-Infrared Functional Fluorescent Dyes with Carboxylic-Acid-Modulated Fluorescence ON/OFF Switching: Rational Design, Synthesis, Optical Properties, Theoretical Calculations, and Applications for Fluorescence Imaging in Living Animals,” *J. Am. Chem. Soc.*, vol. 134, no. 2, pp. 1200–1211, Jan. 2012, doi: 10.1021/ja209292b.

[79] P. L. Smart and I. M. S. Laidlaw, “An evaluation of some fluorescent dyes for water tracing,” *Water Resour. Res.*, vol. 13, no. 1, pp. 15–33, Feb. 1977, doi: 10.1029/WR013i001p00015.

Appendix A Fluorometer Code

```
/*
 * File:   main.c
 * Author: Joshua J. Creelman
 *
 * Created on March 22, 2021, 1:03 PM
 */

#define FCY 4000000UL
//#define DEBUG
#define Hz_1

#include "xc.h"
#include <libpic30.h>
#include "waveparam.h"
#include "timer1.h"
#include "DAC.h"
#include "DMA0.h"
#include "sine.h"
#include "UART1.h"
#include "pipeADC.h"
#include "lock_in.h"
#include "sdADC.h"
#include <stdio.h>
#include "timer2.h"
#include "motor_ctrl.h"
#include "conf_bits.h"
//#pragma config ALTADREF = AVREF_RA    //External 12-Bit A/D Reference Location Select bit->AVREF+/AVREF- are mapped to RA9/RA10
//#pragma config ALTCVREF = CVREF_RA    //External Comparator Reference Location Select bit->CVREF+/CVREF- are mapped to RA9/RA10

//#define PIPE//Not correct pins for for PhosBoard
#define SD
//#define TESTING

//default i/o as read
//read: TRISx = 1

//default analog as enabled
//enabled: ANSx = 1

//following i/o pins must be input
//unless using LCD screen
//LCD pins
/* RA<15:14>,<10>,<6:0>
 * RB<15:14>,<12:7>
 * RC2
 * RD<15:13>,<11:6>
 * RE<8>,<4:0>
 * RF<13:12>,<8>,<3:0>
 * RG<15:12>,<1:0>
 */
//SW1 (RD0)
//following i.o pins must be analog in
/* RG8 potentiometer
 * RA7 phototransistor
 */
#ifdef DEBUG
void init_Debug_LED(void)
{
    //LED1 = RE7, silk screen is incorrect
    ANSE &= ~(1<<7);//RE7 as digital pin
    TRISE &= ~(1<<7);//RE7 as digital output pin
}

#define LEDon() PORTE |= (1<<7);
#define LEDoff() PORTE &= ~(1<<7);

void tx_adc_buff(void);

#endif
#ifdef TESTING
void pipe_ex(void);
void sd_ex(void);
```

```c
#endif

void LEDtest(void)
{
    char str[25];
    init_UART1();
    init_DAC1();
    init_DAC2();
    //RG9 & RB13
    //ANSG &= ~(1<<9);
    //TRISG &= ~(1<<9);
    //PORTG &= ~(1<<9);
    //ANSB &= ~(1<<13);
    //TRISB &= ~(1<<13);
    //PORTB &= ~(1<<13);
    init_sdADC();
    enable_DAC1();
    enable_DAC2();
    while(1){

        //PORTG &= ~(1<<9);
        //PORTB &= ~(1<<13);
        printUART1("low:  ");
        sprintf(str,"%d",read_sdADC());
        printUART1(str);
        printUART1("\n\r");
        DAC1DAT = 1023;
        DAC2DAT = 1023;
        __delay_ms(1000);

        //PORTG |= (1<<9);
        //PORTB |= (1<<13);
        printUART1("high: ");
        sprintf(str,"%d",read_sdADC());
        printUART1(str);
        printUART1("\n\r");
        DAC1DAT=0;
        DAC2DAT=0;
        __delay_ms(1000);
    }
    while(1);
}

void OPA1_Initialize(void)
{
    ANSG |= (1<<6);//RG6 as analog pin
    TRISG |= (1<<6);//RG6 as analog pin
    ANSB |= (1<<4)|(1<<5);//RB4&5 as analog pin
    TRISB |= (1<<4)|(1<<5);//RB4&5 as analog pin
    //Disable the module
    AMP1CONbits.AMPEN = 0;

    // CMOUT disabled; AMPOE enabled; CMPSEL Op-Amp; NINSEL OA1N0; AMPEN enabled; PINSEL OA1P1; SPDSEL Higher power and bandwidth; INTPOL Disabled; AMPSIDL disabled; AMPSLP disabled;
    AMP1CON = 0x80CA;

}

void OPA2_Initialize (void)
{
    ANSG |= (1<<8);//RG8 as analog pin
    TRISG |= (1<<8);//RG8 as analog pin
    ANSD |= (1<<6);//RD6 as analog pin
    TRISD |= (1<<6);//RD6 as analog pin
    ANSB |= (1<<3);//RB3 as analog pin
    TRISB |= (1<<3);//RB3 as analog pin
    //Disable the module
    AMP2CONbits.AMPEN = 0;

    // CMOUT disabled; AMPOE enabled; CMPSEL Op-Amp; NINSEL OA2N2; AMPEN enabled; PINSEL OA2P2; SPDSEL Higher power and bandwidth; INTPOL Disabled; AMPSIDL disabled; AMPSLP disabled;
    AMP2CON = 0x80DB;

}
```

```
short buff[1800];
void LEDtest2(void)
{
    char str[25];
    int i = 0;
    int j = 0;

    init_UART1();
    init_DAC1();
    init_DAC2();
    //RG9 & RB13
    //ANSG &= ~(1<<9);
    //TRISG &= ~(1<<9);
    //PORTG &= ~(1<<9);
    //ANSB &= ~(1<<13);
    //TRISB &= ~(1<<13);
    //PORTB &= ~(1<<13);
    init_sdADC();
    enable_DAC1();
    enable_DAC2();
    DAC1DAT = 0;
    DAC2DAT = 0;
    for(j=0;j<1800;j++){
        DAC1DAT = (i%500);
        DAC2DAT = (i++%500);
        __delay_ms(10);
        buff[j] = read_sdADC();
    }
    for(j=0;j<1800;j++){
        sprintf(str,"%d",buff[j]);
        printUART1(str);
        printUART1("\n\r");
    }
    while(1);
}
void LEDtest3(void)
{
    char str[25];
    int i = 0;
    int j = 0;

    init_UART1();
    init_DAC1();
    init_DAC2();
    //RG9 & RB13
    //ANSG &= ~(1<<9);
    //TRISG &= ~(1<<9);
    //PORTG &= ~(1<<9);
    //ANSB &= ~(1<<13);
    //TRISB &= ~(1<<13);
    //PORTB &= ~(1<<13);
    init_sdADC();
    enable_DAC1();
    enable_DAC2();
    DAC1DAT = 0;
    DAC2DAT = 0;
    __delay_ms(1000);
    for(j=0;j<900;j++){
        __delay_ms(1);
        buff[j] = read_sdADC();
    }
    DAC1DAT = 700;
    DAC2DAT = 700;
    for(j=900;j<1800;j++){
        __delay_ms(1);
        buff[j] = read_sdADC();
    }
    for(j=0;j<1800;j++){
        sprintf(str,"%d",buff[j]);
        printUART1(str);
        printUART1("\n\r");
    }
    while(1);
}
```

```

int main(void) {
#ifndef Hz_1
    int A;
    float P;
#endif
    CLKDIVbits.RCDIV = 0;//CPU no post scaler, therefor Fosc = 8MHz

    init_motors();//disables motor drivers
    OPA1_Initialize();
    OPA2_Initialize();
    //LEDtest();
    //LEDtest2();
    //LEDtest3();
    init_UART1();
#ifdef DEBUG
    writeUART1("Booting...\n\r",12);
#endif
    if((sine = gen_sine(FREQUENCY,FREQUENCY_STEP,AMP,DC_OFF,REF_DAC))==(void*)0){
        printUART1("Unable to allocate sine wave memory\n\r");
        while(1);
    }
#ifdef DEBUG
    writeUART1("Sine wave memory allocated\n\r",28);
#endif
    init_sine(sine);
#ifdef DEBUG
    writeUART1("Associated sine wave generating hardware initialized\n\r",54);
#endif
#ifdef SD
    init_sdADC();
    //sd_ex();
#endif
#ifdef PIPE
    init_pipeADC();
    //pipe_ex();
#endif
#ifdef DEBUG
#ifdef PIPE
    writeUART1("Pipeline ADC initialized\n\r",26);
#endif
#ifdef SD
    printUART1("Sigma-Delta ADC initialized\n\r");
#endif
#endif
#ifdef DEBUG
    writeUART1("Device initialized\n\r",20);
#endif
#ifdef Hz_1
#ifdef DEBUG
    printUART1("init timer 2\n\r");
#endif
    init_TIMER2();
#ifdef DEBUG
    printUART1("enable timer 2\n\r");
#endif
    enable_TIMER2();
#else
    //enable_sine();
    while(1){
#ifdef DEBUG
        writeUART1("Tx sine wave\n\r",14);
#endif
        enable_sine();
        sampling = 1;
        while(sampling);
        disable_sine();
#ifdef DEBUG
        writeUART1("Data collected\n\r",16);
        //tx_adc_buff();
        writeUART1("Beginning lock-in\n\r",19);
#endif
        tx_adc_buff();
        A = lock_in(adc_buff,ADC_BUFF_SIZE,&P);
```

```
        tx_results(A,P);
    }
#endif
    while(1);

    return 0;
}

void tx_adc_buff(void)
{
    int i;
#ifdef PIPE
    char buff[6] = "0000\n\r";
    float factor = REF*1000/4096;
    for(i=0;i<ADC_BUFF_SIZE;i++){
        buff[0] = (char)(adc_buff[i]*factor/1000)|'0';
        buff[1] = (char)((int)(adc_buff[i]*factor/100)%10)|'0';
        buff[2] = (char)((int)(adc_buff[i]*factor/10)%10)|'0';
        buff[3] = (char)((int)(adc_buff[i]*factor)%10)|'0';
        writeUART1(buff,6);
    }
#endif
#ifdef SD
    char buff[25];
    float val;
    for(i=0;i<ADC_BUFF_SIZE;i++){
        val = (adc_buff[i]*REF)/32767;
        sprintf(buff,"%f\n\r",val);
        printUART1(buff);
    }
#endif
}

#ifdef TESTING
void pipe_ex(void)
{
    char buff[7] = "0000mV\r";
    unsigned int data;

    init_pipeADC();

    while(1)
    {
        data = read_pipeADC();
        data = (data*REF*1000)/4096;
        buff[0] = (data/1000)|'0';
        buff[1] = ((data/100)%10)|'0';
        buff[2] = ((data/10)%10)|'0';
        buff[3] = (data%10)|'0';
        writeUART1(buff,7);
        __delay_ms(500);
    }
}

void sd_ex(void)
{
    char buff[25];
    signed short data;
    float val;

    init_sdADC();

    while(1)
    {
        data = read_sdADC();
        val = (data*REF)/32767;
        sprintf(buff,"%fV\n\r",val);
        printUART1(buff);
        __delay_ms(500);
    }
}
#endif
```

```
#ifndef CONF_BITS_H_
#define CONF_BITS_H_

// CONFIG4
//#pragma config DSWDTPS = DSWDTPS1F    //Deep Sleep Watchdog Timer Postscale Select bits->1:68719476736 (25.7 Days)
//#pragma config DSWDTOSC = LPRC    //DSWDT Reference Clock Select->DSWDT uses LPRC as reference clock
//#pragma config DSBOREN = ON    //Deep Sleep BOR Enable bit->DSBOR Enabled
//#pragma config DSWDTEN = ON    //Deep Sleep Watchdog Timer Enable->DSWDT Enabled
//#pragma config DSSWEN = ON    //DSEN Bit Enable->Deep Sleep is controlled by the register bit DSEN
//#pragma config RTCBAT = ON    //RTC Battery Operation Enable->RTC operation is continued through VBAT
//#pragma config PLLDIV = DIS    //PLL Input Prescaler Select bits->PLL is disabled
#pragma config I2C2SEL = PRI    //Alternate I2C2 Location Select bit->I2C2 is multiplexed to SDA2/RA3 and SCL2/RA2
//#pragma config IOL1WAY = ON    //PPS IOLOCK Set Only Once Enable bit->Once set, the IOLOCK bit cannot be cleared

// CONFIG3
//#pragma config WPFP = WPFP127    //Write Protection Flash Page Segment Boundary->Page 127 (0x1FC00)
//#pragma config SOSCSEL = ON    //SOSC Selection bits->SOSC circuit selected
//#pragma config WDTWIN = PS25_0    //Window Mode Watchdog Timer Window Width Select->Watch Dog Timer Window Width is 25 percent
//#pragma config BOREN = ON    //Brown-out Reset Enable->Brown-out Reset Enable
//#pragma config WPDIS = WPDIS    //Segment Write Protection Disable->Disabled
//#pragma config WPCFG = WPCFGDIS    //Write Protect Configuration Page Select->Disabled
//#pragma config WPEND = WPENDMEM    //Segment Write Protection End Page Select->Write Protect from WPFP to the last page of memory

// CONFIG2
//#pragma config POSCMD = HS    //Primary Oscillator Select->HS Oscillator Enabled
//#pragma config WDTCLK = SOSC    //WDT Clock Source Select bits->WDT uses SOSC input
#pragma config OSCIOFCN = ON    //OSCO Pin Configuration->OSCO/CLKO/RC15 functions as port I/O (RC15)
//#pragma config FCKSM = CSDCMD    //Clock Switching and Fail-Safe Clock Monitor Configuration bits->Clock switching and Fail-Safe Clock Monitor are disabled
//#pragma config FNOSC = PRI    //Initial Oscillator Select->Primary Oscillator (XT, HS, EC)
#pragma config ALTADREF = AVREF_RA    //External 12-Bit A/D Reference Location Select bit->AVREF+/AVREF- are mapped to RA9/RA10
#pragma config ALTCVREF = CVREF_RA    //External Comparator Reference Location Select bit->CVREF+/CVREF- are mapped to RA9/RA10
//#pragma config WDTCMX = WDTCLK    //WDT Clock Source Select bits->WDT clock source is determined by the WDTCLK Configuration bits
//#pragma config IESO = OFF    //Internal External Switchover->Disabled

// CONFIG1
//#pragma config WDTPS = PS32768    //Watchdog Timer Postscaler Select->1:32768
//#pragma config FWPSA = PR128    //WDT Prescaler Ratio Select->1:128
//#pragma config WINDIS = OFF    //Windowed WDT Disable->Standard Watchdog Timer
//#pragma config FWDTEN = WDT_ACT    //Watchdog Timer Enable->WDT enabled only while device active and disabled in Sleep
#pragma config ICS = PGx2    //Emulator Pin Placement Select bits->Emulator functions are shared with PGEC2/PGED2
//#pragma config LPCFG = OFF    //Low power regulator control->Disabled - regardless of RETEN
//#pragma config GWRP = OFF    //General Segment Write Protect->Disabled
//#pragma config GCP = OFF    //General Segment Code Protect->Code protection is disabled
#pragma config JTAGEN = OFF    //JTAG Port Enable->Disabled


#endif
```

```
/*
 * File:   DAC.c
 * Author: Joshua J. Creelman
 *
 * Created on March 30, 2021, 2:40 PM
 */

#include "DAC.h"
#include "xc.h"

/*
 * Initializes the DAC
 * to output when written to
 */
void init_DAC1(void)
{
    ANSG |= (1<<9);//RG9 as analog pin
    TRISG |= (1<<9);//RG9 as analog pin
    DAC1CON = 0x0082;//Analog Vdd as ref, 3.3V
    DAC1DAT = 0;//start low
}

/*
 * Initializes the DAC
 * to output when written to
 */
void init_DAC2(void)
{
    ANSG |= (1<<13);//RG13 as analog pin
    TRISG |= (1<<13);//RG13 as analog pin
    DAC2CON = 0x0082;//Analog Vdd as ref, 3.3V
    DAC2DAT = 0;//start low
}
```

```
/*
 * ADC.h
 *
 * Created on March 30, 2021, 2:40 PM
 * Author: Joshua J. Creelman
 */

#ifndef DAC_H_
#define DAC_H_

#define REF_DAC (float)3.3

#define enable_DAC1() DAC1CON |= 0x8000;
#define disable_DAC1() DAC1CON &= ~0x8000;

#define enable_DAC2() DAC2CON |= 0x8000;
#define disable_DAC2() DAC2CON &= ~0x8000;

/* PROTOTYPES */
extern void init_DAC1(void);
extern void init_DAC2(void);

#endif
```

```c
/*
 * File:   DMA0.c
 * Author: Joshua J. Creelman
 *
 * Created on March 30, 2021, 2:43 PM
 */

#include "DMA0.h"
#include "xc.h"
#include "sine.h"

void _ISR _DMA0Interrupt(void)
{
    IFS0 &= ~(1<<4);//clear flag, needed!
    if(DMAINT0&(1<<5)){
        DMASRC0 = sine;//data block
        DMAINT0 &= ~(1<<5);
    }
}

/*
 * Sets up DMA for transferring
 * sinewave data block to DAC
 */
void init_DMA0(int addr, int size)
{
    DMACON = 0x8000;//Enable DMA, fixed priority
    DMAL = RAM_START;
    DMAH = RAM_END;
    DMACH0 = 0x0044;//Channel disabled, increment through src, repeat one-shot, 16 bit
    DMASRC0 = addr;//data block
    DMADST0 = &DAC1DAT;
    DMACNT0 = size;
    DMAINT0 = 0x3900;//TIMER1 as interrupt src
}

void init_DMA0_isr(void)
{
    disable_DMA0_isr();
    IPC1 |= 0x0007;//highest priority
}
```

```c
/*
 * DMA0.h
 *
 * Created on March 30, 2021, 2:43 PM
 * Author: Joshua J. Creelman
 */

#ifndef DMA0_H_
#define DMA0_H_

#define RAM_START 0x0800
#define RAM_END 0x2800

#define enable_DMA0() DMACH0 |= 0x0001;
#define disable_DMA0() DMACH0 &= ~0x0001;

#define enable_DMA0_isr() IEC0 |= (1<<4);
#define disable_DMA0_isr() IEC0 &= ~(1<<4);


/* PROTOTYPES */
extern void init_DMA0(int addr, int size);
extern void init_DMA0_isr(void);

#endif
```

```
/*
 * File:   lock_in.c
 * Author: Joshua J Creelman
 *
 * Created on March 31, 2021, 6:44 PM
 */

#include <stdlib.h>
#include "lock_in.h"
#include "waveparam.h"
#include "xc.h"
#include "sine.h"
#include <math.h>
#include "UART1.h"
#include "pipeADC.h"

//#define DEBUG

#define ss 6
signed long Y[600/ss];
signed long X[600/ss];

signed long average(signed long *buff, int size)
{
    signed long long ave = 0;
    int i;
    //char str[25];
    //printUART1("summing\n\r");
    for(i = 0;i<size;i++){
        ave += buff[i];
        //sprintf(str,"%ld",ave);
        //printUART1(str);
        //printUART1("\n\r");
    }
    /*
    sprintf(str,"%ld",ave);
    printUART1(str);
    printUART1("/");
    sprintf(str,"%d",size);
    printUART1(str);
    printUART1("=");
    sprintf(str,"%ld",ave/size);
    printUART1(str);
    printUART1("\n\r");
    */
    return ave/size;
}

void removeDCoffset(signed long *buff, int size)
{
    int i,ave;
    ave = average(buff,size);
    for(i=0;i<size;i++){
        buff[i] -= ave;
    }
}

void multiplyREF(signed long *buff, signed long *result, int size, char p)
{
    int i,j,seg,off_set,phase;
    phase = (p)? (sine_size>>2):0;
    seg = size/sine_size;
    for(j=0;j<seg;j++){
        off_set = j*sine_size;
        for(i=0;i<sine_size;i++){
            result[i+off_set] = buff[i+off_set] * (sine[(i + phase)%sine_size] -
            ((AMP/REF)*1024));//adjusted ref
        }
    }
}
/*
void lowpass(signed long *buff, int size)
{
    //AVERAGING IS BEST
```

```c
}

#ifdef DEBUG
#include <stdio.h>
#endif
int lock_in(signed long *raw, int size, float *phase)
{
    signed long long x, y;
    signed long result;
    char str[25];
    removeDCoffset(raw,size);
    multiplyREF(raw,X,size,0);//in phase
    multiplyREF(raw,Y,size,1);//out of phase
    //lowpass(X,size);//AVERAGING IS BEST
    //lowpass(Y,size);//AVERAGING IS BEST
    x = average(X,size);
    y = average(Y,size);
#ifdef DEBUG
    sprintf(str,"%ld",(signed long)x);
    printUART1("x=");
    printUART1(str);
    printUART1("\n\r");
    sprintf(str,"%ld",(signed long)y);
    printUART1("y=");
    printUART1(str);
    printUART1("\n\r");
#endif
    *phase = atan2(y,x);
    result = (2/((AMP/REF)*1024))*sqrt(x*x+y*y);
    return result;
}
*/

//optimized for size
signed long *multiply(signed long *buff, int size, short val)
{
    int i;
    for(i=0;i<size;i++){
        buff[i] = buff[i]*val;
    }
    return buff;
}

int lock_in(signed long *raw, int size, float *phase)
{
    int i;
    signed long long x[ss], y[ss];
    signed long result;
    removeDCoffset(raw,size);
    for(i=0;i<ss;i++){
        multiplyREF(raw+i*(size/ss),X,size/ss,0);//in phase
        multiplyREF(raw+i*(size/ss),Y,size/ss,1);//out of phase
        x[i] = average(multiply(X,size/ss,60),size/ss);
        y[i] = average(multiply(Y,size/ss,60),size/ss);
    }
    for(i=1;i<ss;i++){
        x[0] += x[i];
        y[0] += y[i];
    }
    x[0] = x[0]/(ss*60);
    y[0] = y[0]/(ss*60);
    *phase = atan2(y[0],x[0]);
    result = (2/((AMP/REF)*1024))*sqrt(x[0]*x[0]+y[0]*y[0]);
    return result;
}
```

```c
/*
 * lock_in.h
 *
 * Created on March 31, 2021, 6:44 PM
 * Author: Joshua J Creelman
 */

#ifndef LOCK_IN_H_
#define LOCK_IN_H_

/* PROTOTYPES */
extern int lock_in(signed long *raw, int size, float *phase);

#endif
```

```c
/*
 * File:   motor_ctrl.c
 * Author: Joshua J Creelman
 *
 * Created on May 3, 2021, 10:46 AM
 * Disable all motors
 */

//MTR_A_EN on pin RE0  High for disable
//MTR_A_SL on pin RG14 Low for sleep
//MTR_B_EN on pin RF2
//MTR_B_SL on pin RG13
//MTR_C_EN on pin RG0
//MTR_C_SP on pin RF1

#include "motor_ctrl.h"
#include "xc.h"

void init_motors(void)
{
    //RE0 as digital output
    TRISE &= ~(1<<0);
    ANSE &= ~(1<<0);
    //RG14, RG13 and RG0 as digital output
    TRISG &= ~((1<<14)|(1<<13)|(1<<0));
    ANSG &= ~((1<<14)|(1<<13)|(1<<0));
    //RF2 and RF1 as digital output
    TRISF &= ~((1<<2)|(1<<1));
    ANSF &= ~((1<<2)|(1<<1));

    PORTE |= (1<<0);//MTR_A_EN disable
    PORTG &= ~(1<<0);//MTR_A_SP sleep
    PORTF |= (1<<2);//MTR_B_EN disable
    PORTG &= (1<<13);//MTR_B_SP sleep
    PORTG |= (1<<0);//MTR_C_EN disable
    PORTF &= (1<<1);//MTR_C_SP sleep
}
```

```c
/*
 * File:   motor_ctrl.h
 * Author: Joshua J Creelman
 *
 * Created on May 3, 2021, 11:07 AM
 */

#ifndef MOTOR_CTRL_H_
#define MOTOR_CTRL_H_

/* PROTOTYPES */
extern void init_motors(void);

#endif
```

```c
/*
 * File:   pipeADC.c
 * Author: Joshua J. Creelman
 *
 * Created on March 30, 2021, 2:17 PM
 */

#include "pipeADC.h"
#include "xc.h"

short read_pipeADC(void)
{
    IFS0bits.AD1IF = 0;
    ADL0CONLbits.SAMP = 0;
    while(IFS0bits.AD1IF == 0);
    ADL0CONLbits.SAMP = 1;
    return ADRES0;
}

void init_pipeADC(void)
{
    //RD5 -> AN48
    ANSD |= (1<<5);//RD5 as analog pin
    TRISD |= (1<<5);//RD5 as analog pin
    //Clear registers
    ADCON1 = 0;
    ADCON2 = 0;
    ADCON3 = 0;
    //Set references
    ADCON2bits.PVCFG = 0;//Vp -> AVdd
    ADCON2bits.NVCFG = 0;//Vn -> AVss

    ADCON3bits.ADRC = 0;//System clock as source
    ADCON3bits.ADCS = 1;

    ADCON1bits.FORM = 0;
    ADCON2bits.BUFORG = 1;

    ADCON2 |= 0x0300;//normal operation

    ADCON1bits.PWRLVL = 1;

    ADL0CONL = 0;
    ADL0CONH = 0;
    ADL0CONLbits.SLSIZE = 1-1;

    ADL0CONHbits.ASEN = 1;
    ADL0CONHbits.SLINT = 1;
    ADL0CONHbits.SAMC = 15;
    ADL0CONLbits.SLTSRC = 0;
    ADL0PTR = 0;

    ADL0CONHbits.CM = 0;

    ADTBL0bits.ADCH = 48;

    ADCON1bits.ADON = 1;
    while(ADSTATHbits.ADREADY == 0);
    ADCON1bits.ADCAL = 1;
    while(ADSTATHbits.ADREADY == 0);
    ADL0CONLbits.SAMP = 1;
    ADL0CONLbits.SLEN = 1;

    read_pipeADC();//ignore first conversion
}

```

```
/*
 * pipeADC.h
 *
 * Created on March 30, 2021, 2:17 PM
 * Author: Joshua J. Creelman
 */

#ifndef PIPEADC_H_
#define PIPEADC_H_

#define ADC_BUFF_SIZE 600

extern signed long adc_buff[];

/* PROTOTYPES */
extern void init_pipeADC(void);
extern short read_pipeADC(void);

#endif
```

```
/*
 * File:   sdADC.c
 * Author: Joshua J. Creelman
 *
 * Created on April 16, 2021, 2:01 PM
 */

#include "sdADC.h"
#include "xc.h"

short read_sdADC(void)
{
    //Clear interrupt flag.
    IFS6bits.SDA1IF = 0;
    //Wait for the result ready.
    while(IFS6bits.SDA1IF == 0);
    return SD1RESH;
}

void init_sdADC(void)
{
    int i;

    // Configure the SD A/D module
    SD1CON1bits.PWRLVL = 0; // Low power, normal bandwidth
    SD1CON1bits.SDREFP = 0; // Positive Voltage Reference is SVDD
    SD1CON1bits.SDREFN = 0; // Negative Voltage Reference is SVSS
    SD1CON1bits.VOSCAL = 0; // Internal Offset Measurement is disabled
    SD1CON1bits.DITHER = 1; // Low Dither
    SD1CON1bits.SDGAIN = 0; // Gain is 1:1

    SD1CON2bits.RNDRES = 2; // Round result to 16-bit
    SD1CON2bits.SDWM = 1; // SDxRESH/SDxRESL updated on every Interrupt
    SD1CON2bits.CHOP = 3; // Chopping should be enabled

    SD1CON3bits.SDCH = 0; // Diff CH0 (diff channel 1 = 1))
    SD1CON3bits.SDCS = 1; // Clock Source is a 8 MHz FRC
    SD1CON3bits.SDOSR = 5; // 6 fastest, lowest quality : 0 slowest best quality
    SD1CON3bits.SDDIV = 1; // Input Clock Divider is 2 (SD ADC clock is 4MHz)

    // Configure SD A/D interrupt
    SD1CON2bits.SDINT = 3; // Interrupt on every data output
    IFS6bits.SDA1IF = 0; // Clear interrupt flag

    // Turn on the SD A/D module
    SD1CON1bits.SDON = 1;

    // Wait for a minimum of five interrupts to be generated. Need to throw at least
    // the first four away when using interrupt every period option, since the
    // low pass SINC filter needs to be flushed with new data when we change
    // ADC channel or initialize the ADC.
    for(i=0; i<8; i++)
    {
        read_sdADC();
    }
}
```

```c
/*
 * File:   sdADC.h
 * Author: Joshua J. Creelman
 *
 * Created on April 16, 2021, 2:01 PM
 */

#ifndef SDADC_H_
#define SDADC_H_

/* PROTOTYPES */
extern short read_sdADC(void);
extern void init_sdADC(void);

#endif
```

```c
/*
 * File:   sine.c
 * Author: Joshua J. Creelman
 *
 * Created on March 30, 2021, 2:47 PM
 */

#include "sine.h"
#include "xc.h"
#include <stdlib.h>
#include <math.h>
#include "waveparam.h"
#include "timer1.h"
#include "DMA0.h"
#include "DAC.h"

short *sine;
int sine_size;

/*
 * Generates memory block for a
 * sinewave. Returns start address
 * and size.
 * df max = 1000000
 * Higher df results in more space taken
 */
short *gen_sine(float f, float df, float A, float off_set, float ref)
{
    short *data;
    int i;

    sine_size = (int)df/f;
    data = (short *)malloc((sine_size)*sizeof(short));//REMEMBER TO ALLOCATE HEAP SIZE!!!

    if(data != (void*)0){
        for(i = 0; i < sine_size; i++){
            *(data + i) = (short)((A*1024*sin(2*pi*f*i/df) + off_set*1024)/ref);
            *(data + i) =(*(data+i)>1023)?1023:*(data+i);
        }
    }

    return data;
}

/*
 * Initializes associated
 * peripherals for sine wave
 * generation.
 */
void init_sine(short *data)
{
    init_DAC1();
    init_DMA0(data, sine_size);
    init_DMA0_isr();
    init_TIMER1();
    enable_DAC1();
    enable_DMA0();
    enable_DMA0_isr();
}

/*
 * Disabling sine wave may
 * require reinitialization.
 */
/*
void disable_sine()
{
    disable_TIMER1();
    disable_DAC1();
    disable_DMA0();
}
*/

void disable_sine(void)
```

```c
{
    disable_TIMER1();
    DAC1DAT = 0;
}
```

```c
/*
 * sine.h
 *
 * Created on March 30, 2021, 2:47 PM
 * Author: Joshua J. Creelman
 */

#ifndef SINE_H_
#define SINE_H_

#define pi 3.14159265359

#define enable_sine() enable_TIMER1()
//#define disable_sine() disable_TIMER1()

extern short *sine;
extern int sine_size;

/* PROTOTYPES */
extern short *gen_sine(float f, float df, float A, float off_set, float ref);
extern void init_sine(short *data);
extern void disable_sine(void);

#endif
```

```
/*
 * File:   timer1.c
 * Author: Joshua J. Creelman
 *
 * Created on March 30, 2021, 2:35 PM
 */

#include "timer1.h"
#include "xc.h"
#include "waveparam.h"
#include "pipeADC.h"
#include "sine.h"
#include "sdADC.h"

#include "UART1.h"

unsigned char sampling;
signed long adc_buff[ADC_BUFF_SIZE];
int adc_idx;

/*
 * Sets timer1 up for DAC and DMA
 * sine wave generation.
 */
void init_TIMER1(void)
{
    PR1 = 4000000/FREQUENCY_STEP;
    T1CON = 0x0000;//timer1 off with internal oscillator no pre-scaler
    IFS0bits.T1IF = 0;//clear flag
    IPC0bits.T1IP = 5;//higher priority than timer 2/3
    adc_idx = 0;
    IEC0bits.T1IE = 1;//enable timer 1 interrupt
}

void _ISR _T1Interrupt(void)
{
    IFS0bits.T1IF = 0;//clear flag
    //adc_buff[adc_idx] = read_pipeADC();
    //adc_buff[adc_idx] += read_pipeADC();
    //adc_buff[adc_idx] += read_pipeADC();
    //adc_buff[adc_idx] = adc_buff[adc_idx]/2;
    adc_buff[adc_idx] = read_sdADC();
    //if(adc_buff[adc_idx]>30000){
        //printUART1("sat\n\r");
    //}
    if(adc_idx >= (ADC_BUFF_SIZE-1)){
        sampling = 0;
        adc_idx = 0;
        disable_sine();
    }else{
        adc_idx++;
    }
}

/*
//Uses timer 1 and the internal timer for x*1ms delay
//timer uses Fosc/2
void msDelay(int x)
{
    //poll T1IF flag method
    int i;
    PR1 = 4000;//period of 1ms
    T1CON = 0x8000;//timer1 on with internal oscillator no pre-scaler
    for(i = 0; i < x; i++){
        while(!(IFS0&0x0008));//poll T1IF
        IFS0 &= ~0x0008;//clear T1IF
    }
    T1CON = 0x0000;//timer1 off
    return;
}
*/
```

```c
/*
 * timer1.h
 *
 * Created on March 30, 2021, 2:35 PM
 * Author: Joshua J. Creelman
 */

//Internal Oscillator 8MHz
//default post scaler of 2!!! Therefore Fosc = 4MHz and Fosc/2 = 2MHz

//SOSC
/* Secondary timer for Timer 1 or RTC
 * 32.768kHz
 */

#ifndef TIMER1_H_
#define TIMER1_H_

#define enable_TIMER1() T1CON |= 0x8000;
#define disable_TIMER1() T1CON &= ~0x8000;

extern unsigned char sampling;

/* PROTOTYPES */
extern void init_TIMER1(void);

#endif
```

```c
/*
 * File:   timer2.c
 * Author: Joshua J. Creelman
 *
 * Created on April 27, 2021, 12:56 PM
 */

#include "timer2.h"
#include "xc.h"
#include "sine.h"
#include "pipeADC.h"
#include "lock_in.h"
#include "timer1.h"
#include "UART1.h"

#include "DAC.h"

//#define DEBUG

// 1 Second interrupts
void init_TIMER2(void)
{
    PR3 = (0xffff)&(4000000>>16);
    PR2 = 0xffff&4000000;
    T2CON = 0x0000;//timer2 off with internal oscillator no pre-scaler
    T2CONbits.T32 = 1;
    IFS0bits.T3IF = 0;//clear flag
    IPC2bits.T3IP = 3;//lower priority than timer 1.
    IEC0bits.T3IE = 1;//enable timer 3 interrupt
}

void _ISR _T3Interrupt(void)
{
    int A;
    float P;
    IFS0bits.T3IF = 0;//clear flag
#ifdef DEBUG
        writeUART1("Tx sine wave\n\r",14);
#endif
    enable_sine();
    sampling = 1;
    while(sampling);
    /*
    int i;
    char buff[25];
    float val;
    for(i=0;i<ADC_BUFF_SIZE;i++){
        val = (adc_buff[i]*3.0)/32767;
        sprintf(buff,"%f\n\r",val);
        printUART1(buff);
    }
    */
    A = lock_in(adc_buff,ADC_BUFF_SIZE,&P);
    tx_results(A,P);
}
```

```c
/*
 * timer2.h
 *
 * Created on April 27, 2021, 12:56 PM
 * Author: Joshua J. Creelman
 */

//Internal Oscillator 8MHz
//default post scaler of 2!!! Therefore Fosc = 4MHz and Fosc/2 = 2MHz

//SOSC
/* Secondary timer for Timer 1 or RTC
 * 32.768kHz
 */

#ifndef TIMER2_H_
#define TIMER2_H_

#define enable_TIMER2() T2CON |= 0x8000;
#define disable_TIMER2() T2CON &= ~0x8000;


/* PROTOTYPES */
extern void init_TIMER2(void);

#endif
```

```
/*
 * File:   UART1.c
 * Author: Joshua J. Creelman
 *
 * Created on March 30, 2021, 2:27 PM
 */

#include "UART1.h"
#include "xc.h"
#include <stdio.h>

void _ISR _U1TXInterrupt(void)
{
    IFS0 &= ~(1<<12);
}

void init_UART1(void)
{
#ifdef PINRC1asRx
    ANSC &= ~(1<<1);//RC1 as digital pin
    TRISC |= (1<<1);//RC1 as digital input pin
#endif
#ifdef PINRC3asRx
    ANSC &= ~(1<<3);//RC3 as digital pin
    TRISC |= (1<<3);//RC3 as digital input pin
#endif
#ifdef PINRB6asTx
    ANSB &= ~(1<<6);//RB6 as digital pin
    TRISB &= ~(1<<6);//RB6 as digital output pin
    LATB |= (1<<6);//LAT pin corresponding to Tx as high
#endif
#ifdef PINRD5asTx
    ANSD &= ~(1<<5);//RD5 as digital pin
    TRISD &= ~(1<<5);//RD5 as digital output pin
    LATD |= (1<<5);//LAT pin corresponding to Tx as high
#endif
#ifdef PINRC1asRx
    RPINR18bits.U1RXR = 0x0026;//RC1 -> UART1:U1RX
#endif
#ifdef PINRC3asRx
    RPINR18bits.U1RXR = 0x0028;//RC3 -> UART1:U1RX
#endif
#ifdef PINRB6asTx
    RPOR3bits.RP6R = 0x0003;// RB6 -> UART1:U1TX
#endif
#ifdef PINRD5asTx
    RPOR10bits.RP20R = 0x0003;//RD5 - > UART1:U1TX
#endif
    U1MODE = 0x8800;//enable UART, simplex mode
    U1BRG = 25;// 9600 BAUDRATE, 0.2% error
    U1STA = (1<<10);// enable Tx, interrupt when char shifted into TSR

    //IEC0 |= (1<<12);//ISR enabled
}

void writeUART1(char *buff, int size)
{
    int i;
    for(i = 0; i < size; i++){
        while((U1STA & (1<<8)) == 0);
        U1TXREG = *(buff + i);
    }
}
/*
void tx_val(int val)
{
    char buff[7] = "00000\n\r";
    buff[0] = (val/10000)|'0';
    buff[1] = ((val/1000)%10)|'0';
    buff[2] = ((val/100)%10)|'0';
    buff[3] = ((val/10)%10)|'0';
    buff[4] = (val%10)|'0';
    writeUART1(buff,7);
}
```

```
*/
void printUART1(char *str)
{
    int i = 0;
    while(*(str + i)!='\0'){
        while((U1STA & (1<<8)) == 0);
        U1TXREG = *(str + i);
        i++;
    }
}

void tx_results(int mag, float delay)
{
    char str[25];
    sprintf(str,"(%f,%f)\n\r",(float)(mag*3.3/32767),delay);
    printUART1(str);
}
```

```
/*
 * UART1.h
 *
 * Created on March 30, 2021, 2:27 PM
 * Author: Joshua J. Creelman
 */

#ifndef UART1_H_
#define UART1_H_

//#define PINRC3asRx
#define PINRC1asRx

//#define PINRB6asTx
#define PINRD5asTx

/* PROTOTYPES */
extern void init_UART1(void);
extern void writeUART1(char *buff, int size);
extern void printUART1(char *buff);
extern void tx_val(int val);
extern void tx_results(int mag, float delay);

#endif
```

```
/*
 * waveparam.h
 *
 * Created on April 8, 2021, 2:03 PM
 * Author: Joshua J Creelman
 */

#ifndef WACEPARAM_H_
#define WAVEPARAM_H_

#define REF (float)3.0

#define FREQUENCY 100
#define AMPpp 1.0
#define AMP AMPpp/2
#define DC_OFF AMP

#define FREQUENCY_STEP 10000//***Not sure after bug fix***//seems 30000 is max, imperically measured

#endif
```

Appendix B Early Optic Studios Simulation Results

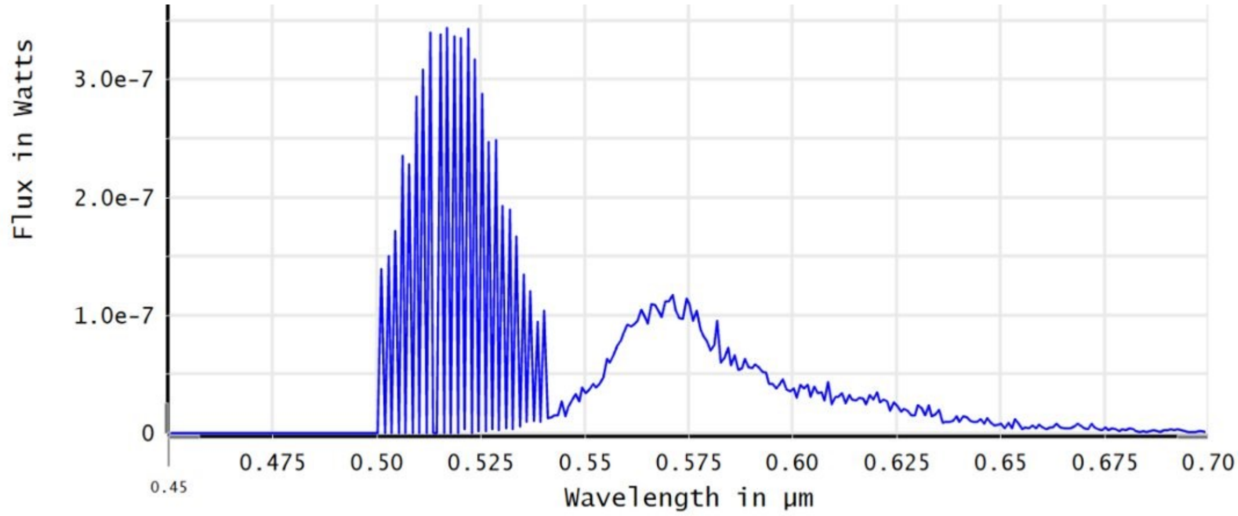

Figure B.1: Spectral curve of detector at the aperture using the setup from figure 4.2.

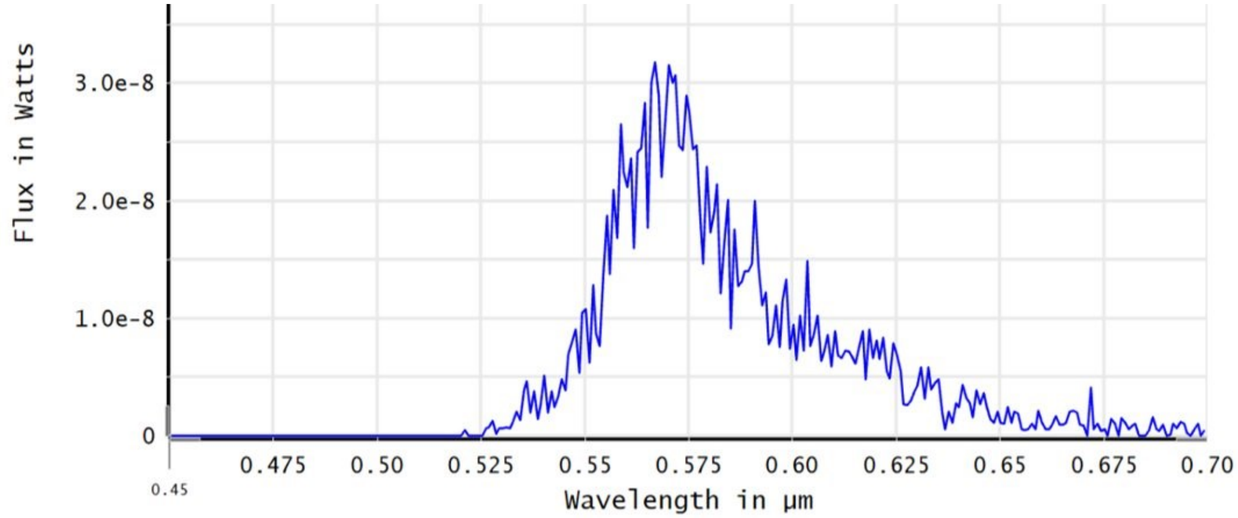

Figure B.2: Spectral curve of detector just before the filter using the setup from figure 4.2.

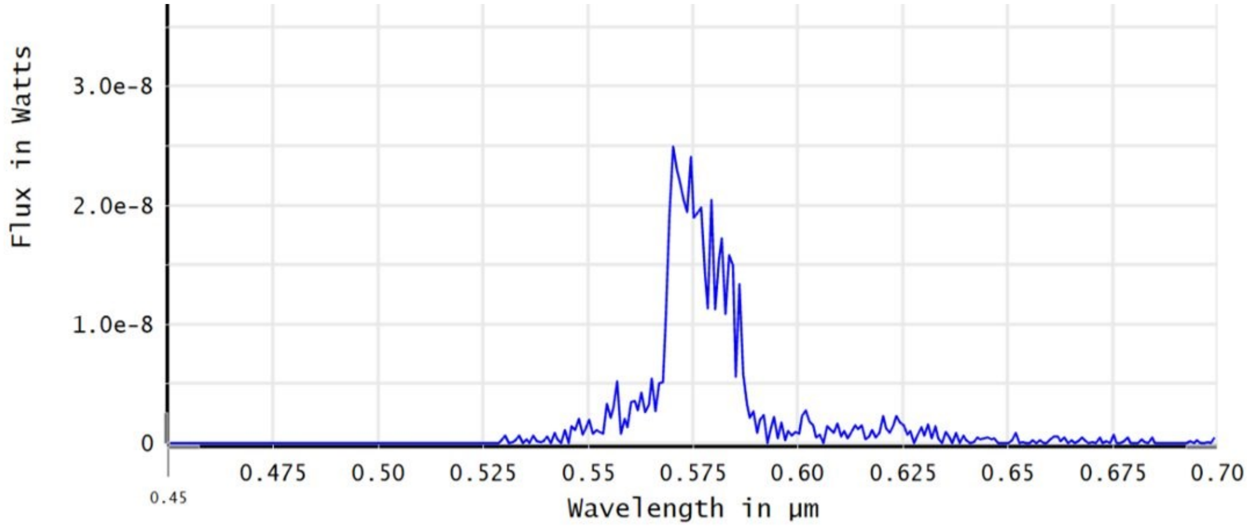

Figure B.3: Spectral curve of detector just after filter using the setup from figure 4.2.

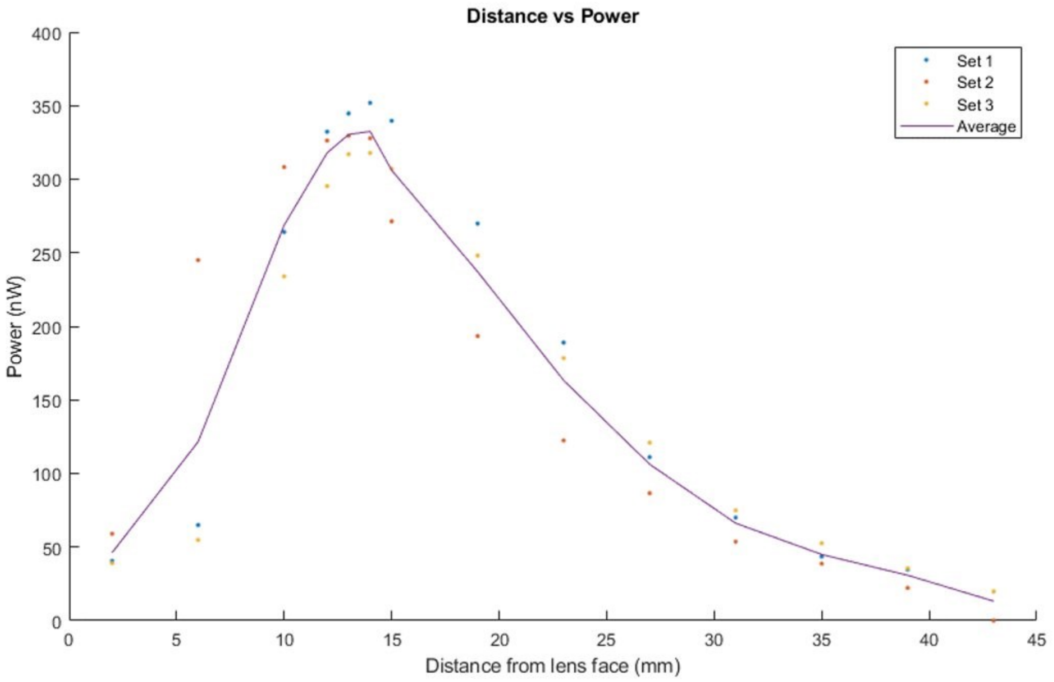

Figure B.4: Distance vs power curve using the setup from figure 4.2.

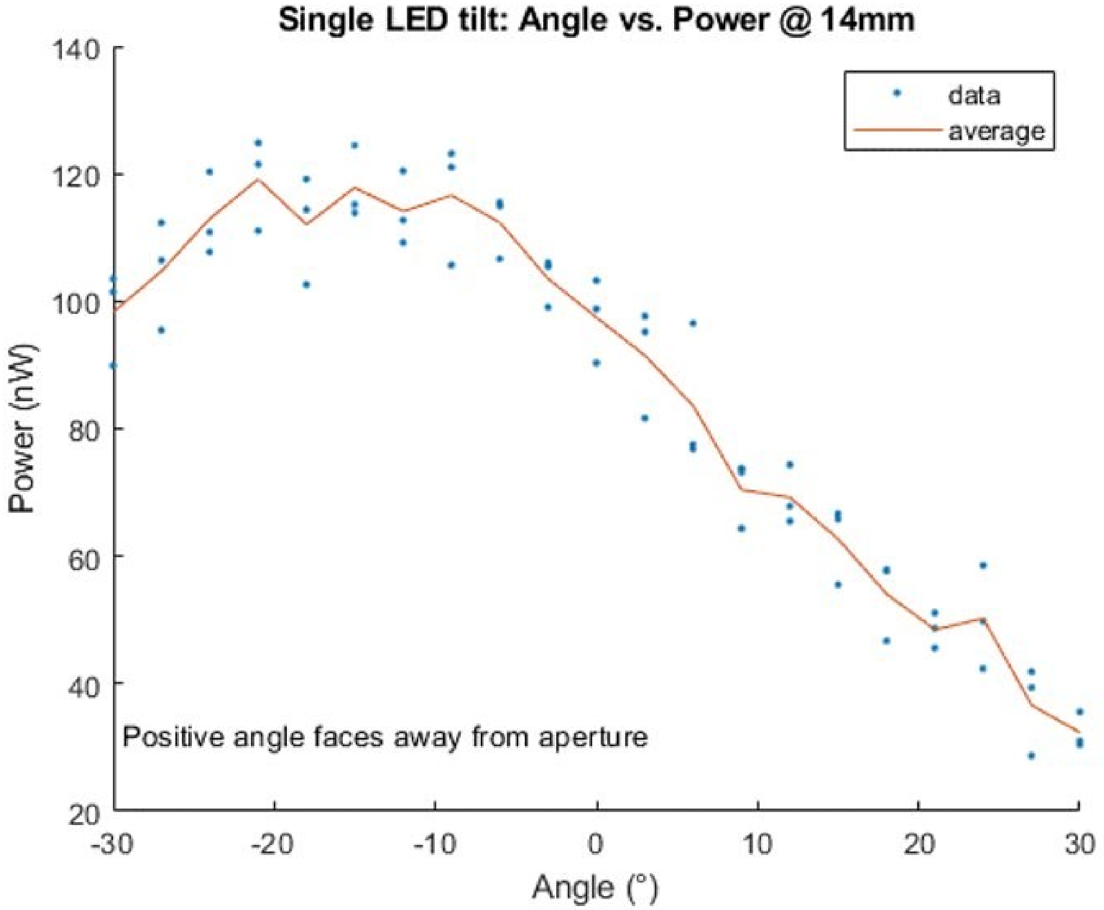

Figure B.5: Result of an angle sweep using the setup from figure 4.3.

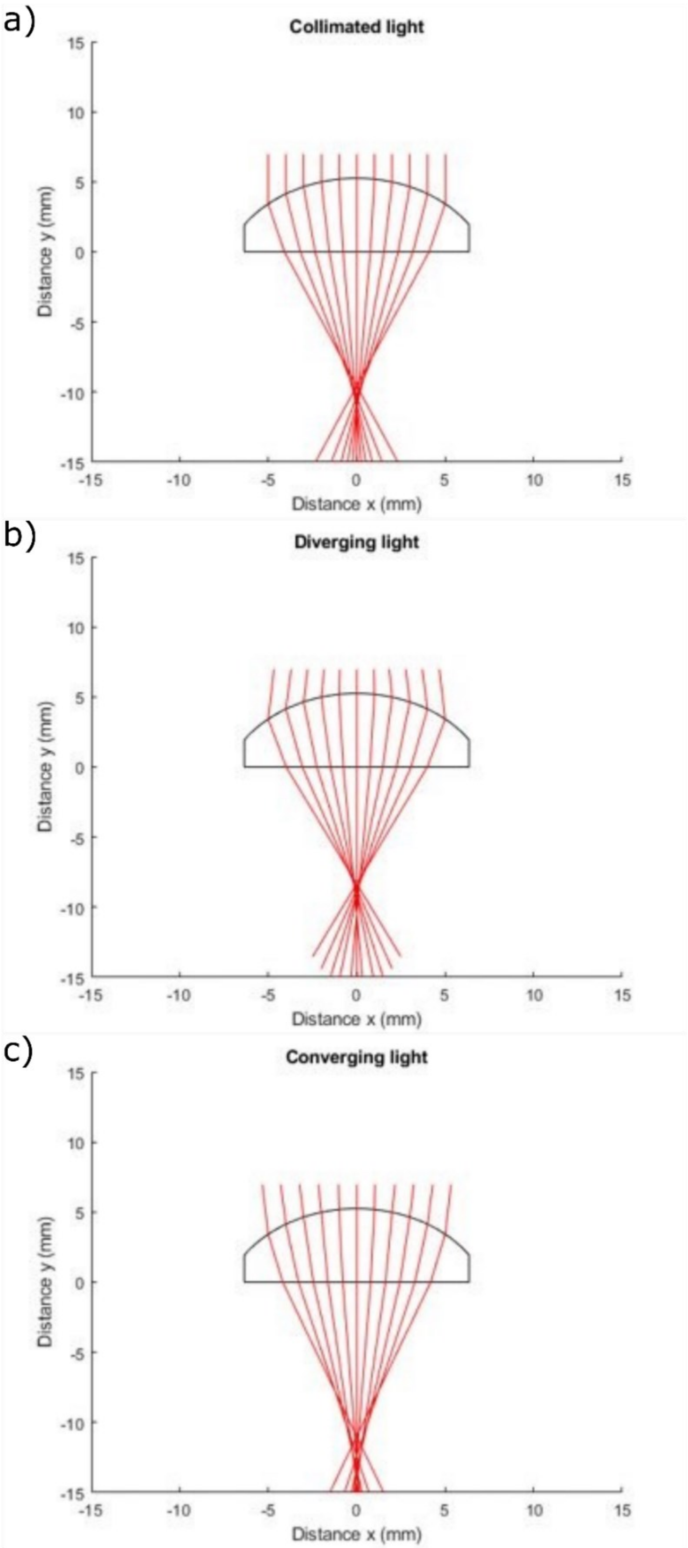

Figure B.6: MATLAB ray tracing simulation. (a) MATLAB graphical representation of collimated light passing through a plano-convex lens. (b) MATLAB graphical representation of slightly divergent light passing through a plano-convex lens. (c) MATLAB graphical representation of slightly convergent light passing through a plano-convex lens.

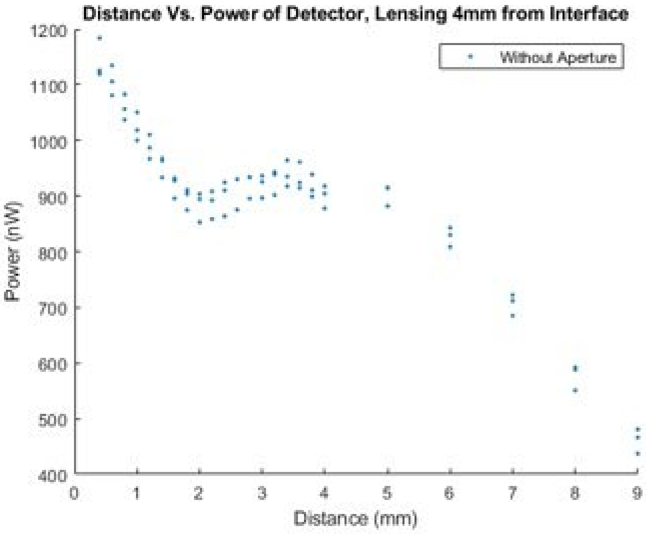

Figure B.7: Distance sweep using the setup of Figure 4.5; lenses 4 mm from interface.

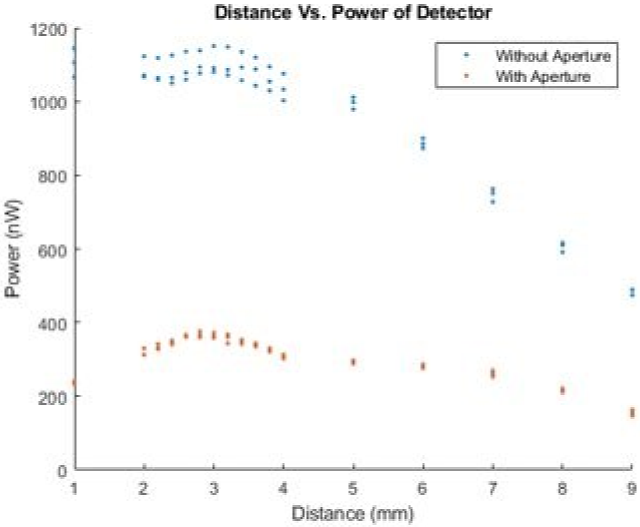

Figure B.8: Distance sweep using the setup of Figure 4.5; lenses 5 mm from interface.

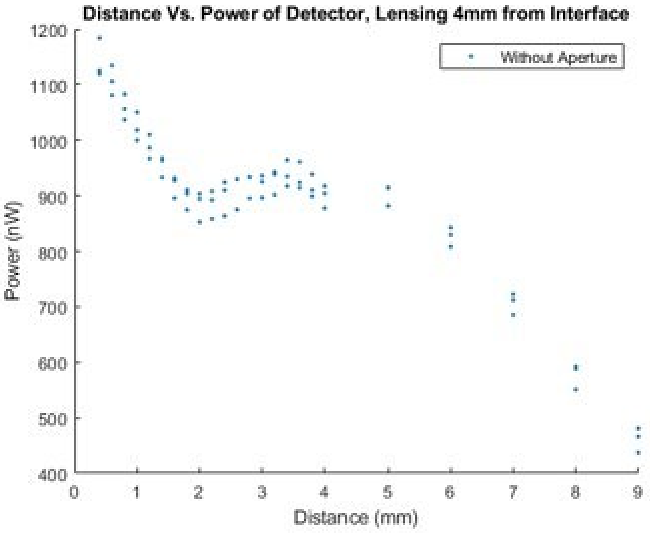

Figure B.9: Distance sweep using the setup of Figure 4.5; lenses 6 mm from interface.

Appendix C Copyright Permissions

Below is the copyright permission for Figure 1.1. All other reprint figures are from open access sources and/or fall under fair use.

ELSEVIER LICENSE
TERMS AND CONDITIONS
Dec 16, 2022

This Agreement between Mr. Joshua Creelman ("You") and Elsevier ("Elsevier") consists of your license details and the terms and conditions provided by Elsevier and Copyright Clearance Center.

License Number	5442590763942
License date	Dec 05, 2022
Licensed Content Publisher	Elsevier
Licensed Content Publication	Elsevier Books
Licensed Content Title	Methods in Cell Biology
Licensed Content Author	Natasha Shanker,Susan L. Bane
Licensed Content Date	Jan 1, 2008
Licensed Content Pages	30
Start Page	213
End Page	242
Type of Use	reuse in a thesis/dissertation
Portion	figures/tables/illustrations
Number of figures/tables/illustrations	1
Format	electronic
Are you the author of this Elsevier chapter?	No
Will you be translating?	No
Title	Low-Cost Submersible Fluorometer for Fresh and Marine Water Environments

Institution name	Dalhousie University
Expected presentation date	Jan 2023
Portions	Figure 5
Requestor Location	Mr. Joshua Creelman 2-96 Central Avenue Halifax, NS B3N2H8 Canada Attn: Mr. Joshua Creelman
Publisher Tax ID	GB 494 6272 12
Total	0.00 CAD
Terms and Conditions	

INTRODUCTION

1. The publisher for this copyrighted material is Elsevier. By clicking "accept" in connection with completing this licensing transaction, you agree that the following terms and conditions apply to this transaction (along with the Billing and Payment terms and conditions established by Copyright Clearance Center, Inc. ("CCC"), at the time that you opened your Rightslink account and that are available at any time at http://myaccount.copyright.com).

GENERAL TERMS

2. Elsevier hereby grants you permission to reproduce the aforementioned material subject to the terms and conditions indicated.

3. Acknowledgement: If any part of the material to be used (for example, figures) has appeared in our publication with credit or acknowledgement to another source, permission must also be sought from that source. If such permission is not obtained then that material may not be included in your publication/copies. Suitable acknowledgement to the source must be made, either as a footnote or in a reference list at the end of your publication, as follows:

"Reprinted from Publication title, Vol /edition number, Author(s), Title of article / title of chapter, Pages No., Copyright (Year), with permission from Elsevier [OR APPLICABLE SOCIETY COPYRIGHT OWNER]." Also Lancet special credit - "Reprinted from The Lancet, Vol. number, Author(s), Title of article, Pages No., Copyright (Year), with permission from Elsevier."

4. Reproduction of this material is confined to the purpose and/or media for which permission is hereby given.

5. Altering/Modifying Material: Not Permitted. However figures and illustrations may be altered/adapted minimally to serve your work. Any other abbreviations, additions, deletions and/or any other alterations shall be made only with prior written authorization of Elsevier Ltd. (Please contact Elsevier's permissions helpdesk here). No modifications can be made to any Lancet figures/tables and they must be reproduced in full.

6. If the permission fee for the requested use of our material is waived in this instance, please be advised that your future requests for Elsevier materials may attract a fee.

7. Reservation of Rights: Publisher reserves all rights not specifically granted in the combination of (i) the license details provided by you and accepted in the course of this licensing transaction, (ii) these terms and conditions and (iii) CCC's Billing and Payment terms and conditions.

8. License Contingent Upon Payment: While you may exercise the rights licensed immediately upon issuance of the license at the end of the licensing process for the transaction, provided that you have disclosed complete and accurate details of your proposed use, no license is finally effective unless and until full payment is received from you (either by publisher or by CCC) as provided in CCC's Billing and Payment terms and conditions. If full payment is not received on a timely basis, then any license preliminarily granted shall be deemed automatically revoked and shall be void as if never granted. Further, in the event that you breach any of these terms and conditions or any of CCC's Billing and Payment terms and conditions, the license is automatically revoked and shall be void as if never granted. Use of materials as described in a revoked license, as well as any use of the materials beyond the scope of an unrevoked license, may constitute copyright infringement and publisher reserves the right to take any and all action to protect its copyright in the materials.

9. Warranties: Publisher makes no representations or warranties with respect to the licensed material.

10. Indemnity: You hereby indemnify and agree to hold harmless publisher and CCC, and their respective officers, directors, employees and agents, from and against any and all claims arising out of your use of the licensed material other than as specifically authorized pursuant to this license.

11. No Transfer of License: This license is personal to you and may not be sublicensed, assigned, or transferred by you to any other person without publisher's written permission.

12. No Amendment Except in Writing: This license may not be amended except in a writing signed by both parties (or, in the case of publisher, by CCC on publisher's behalf).

13. Objection to Contrary Terms: Publisher hereby objects to any terms contained in any purchase order, acknowledgment, check endorsement or other writing prepared by you, which terms are inconsistent with these terms and conditions or CCC's Billing and Payment terms and conditions. These terms and conditions, together with CCC's Billing and Payment terms and conditions (which are incorporated herein), comprise the entire agreement between you and publisher (and CCC) concerning this licensing transaction. In the event of any conflict between your obligations established by these terms and conditions and those established by CCC's Billing and Payment terms and conditions, these terms and conditions shall control.

14. Revocation: Elsevier or Copyright Clearance Center may deny the permissions described in this License at their sole discretion, for any reason or no reason, with a full refund payable to you. Notice of such denial will be made using the contact information provided by you. Failure to receive such notice will not alter or invalidate the denial. In no event will Elsevier or Copyright Clearance Center be responsible or liable for any costs, expenses or damage incurred by you as a result of a denial of your permission request, other than a refund of the amount(s) paid by you to Elsevier and/or Copyright Clearance Center for denied permissions.

LIMITED LICENSE

The following terms and conditions apply only to specific license types:

15. **Translation**: This permission is granted for non-exclusive world **English** rights only unless your license was granted for translation rights. If you licensed translation rights you may only translate this content into the languages you requested. A professional translator must perform all translations and reproduce the content word for word preserving the integrity of the article.

16. **Posting licensed content on any Website**: The following terms and conditions apply as follows: Licensing material from an Elsevier journal: All content posted to the web site must maintain the copyright information line on

the bottom of each image; A hyper-text must be included to the Homepage of the journal from which you are licensing at http://www.sciencedirect.com/science/journal/xxxxx or the Elsevier homepage for books at http://www.elsevier.com; Central Storage: This license does not include permission for a scanned version of the material to be stored in a central repository such as that provided by Heron/XanEdu.

Licensing material from an Elsevier book: A hyper-text link must be included to the Elsevier homepage at http://www.elsevier.com . All content posted to the web site must maintain the copyright information line on the bottom of each image.

Posting licensed content on Electronic reserve: In addition to the above the following clauses are applicable: The web site must be password-protected and made available only to bona fide students registered on a relevant course. This permission is granted for 1 year only. You may obtain a new license for future website posting.

17. **For journal authors:** the following clauses are applicable in addition to the above:

Preprints:

A preprint is an author's own write-up of research results and analysis, it has not been peer-reviewed, nor has it had any other value added to it by a publisher (such as formatting, copyright, technical enhancement etc.).

Authors can share their preprints anywhere at any time. Preprints should not be added to or enhanced in any way in order to appear more like, or to substitute for, the final versions of articles however authors can update their preprints on arXiv or RePEc with their Accepted Author Manuscript (see below).

If accepted for publication, we encourage authors to link from the preprint to their formal publication via its DOI. Millions of researchers have access to the formal publications on ScienceDirect, and so links will help users to find, access, cite and use the best available version. Please note that Cell Press, The Lancet and some society-owned have different preprint policies. Information on these policies is available on the journal homepage.

Accepted Author Manuscripts: An accepted author manuscript is the manuscript of an article that has been accepted for publication and which typically includes author-incorporated changes suggested during submission, peer review and editor-author communications.

Authors can share their accepted author manuscript:

- immediately
    - via their non-commercial person homepage or blog
    - by updating a preprint in arXiv or RePEc with the accepted manuscript
    - via their research institute or institutional repository for internal institutional uses or as part of an invitation-only research collaboration work-group
    - directly by providing copies to their students or to research collaborators for their personal use
    - for private scholarly sharing as part of an invitation-only work group on commercial sites with which Elsevier has an agreement
- After the embargo period
    - via non-commercial hosting platforms such as their institutional repository
    - via commercial sites with which Elsevier has an agreement

In all cases accepted manuscripts should:

- link to the formal publication via its DOI
- bear a CC-BY-NC-ND license - this is easy to do
- if aggregated with other manuscripts, for example in a repository or other site, be shared in alignment with our hosting policy not be added to or enhanced in any way to appear more like, or to substitute for, the published journal article.

Published journal article (JPA): A published journal article (PJA) is the definitive final record of published research that appears or will appear in the journal and embodies all value-adding publishing activities including peer review co-ordination, copy-editing, formatting, (if relevant) pagination and online enrichment.

Policies for sharing publishing journal articles differ for subscription and gold open access articles:

Subscription Articles: If you are an author, please share a link to your article rather than the full-text. Millions of researchers have access to the formal publications on ScienceDirect, and so links will help your users to find, access, cite, and use the best available version.

Theses and dissertations which contain embedded PJAs as part of the formal submission can be posted publicly by the awarding institution with DOI links back to the formal publications on ScienceDirect.

If you are affiliated with a library that subscribes to ScienceDirect you have additional private sharing rights for others' research accessed under that agreement. This includes use for classroom teaching and internal training at the institution (including use in course packs and courseware programs), and inclusion of the article for grant funding purposes.

Gold Open Access Articles: May be shared according to the author-selected end-user license and should contain a CrossMark logo, the end user license, and a DOI link to the formal publication on ScienceDirect.

Please refer to Elsevier's posting policy for further information.

18. **For book authors** the following clauses are applicable in addition to the above: Authors are permitted to place a brief summary of their work online only. You are not allowed to download and post the published electronic version of your chapter, nor may you scan the printed edition to create an electronic version. **Posting to a repository:** Authors are permitted to post a summary of their chapter only in their institution's repository.

19. **Thesis/Dissertation**: If your license is for use in a thesis/dissertation your thesis may be submitted to your institution in either print or electronic form. Should your thesis be published commercially, please reapply for permission. These requirements include permission for the Library and Archives of Canada to supply single copies, on demand, of the complete thesis and include permission for Proquest/UMI to supply single copies, on demand, of the complete thesis. Should your thesis be published commercially, please reapply for permission. Theses and dissertations which contain embedded PJAs as part of the formal submission can be posted publicly by the awarding institution with DOI links back to the formal publications on ScienceDirect.

Elsevier Open Access Terms and Conditions

You can publish open access with Elsevier in hundreds of open access journals or in nearly 2000 established subscription journals that support open access publishing. Permitted third party re-use of these open access articles is defined by the author's choice of Creative Commons user license. See our open access license policy for more information.

Terms & Conditions applicable to all Open Access articles published with Elsevier:

Any reuse of the article must not represent the author as endorsing the adaptation of the article nor should the article be modified in such a way as to damage the author's honour or reputation. If any changes have been made, such changes must be clearly indicated.

The author(s) must be appropriately credited and we ask that you include the end user license and a DOI link to the formal publication on ScienceDirect.

If any part of the material to be used (for example, figures) has appeared in our publication with credit or acknowledgement to another source it is the responsibility of the user to ensure their reuse complies with the terms and conditions determined by the rights holder.

Additional Terms & Conditions applicable to each Creative Commons user license:

CC BY: The CC-BY license allows users to copy, to create extracts, abstracts and new works from the Article, to alter and revise the Article and to make commercial use of the Article (including reuse and/or resale of the Article by commercial entities), provided the user gives appropriate credit (with a link to the formal publication through the relevant DOI), provides a link to the license, indicates if changes were made and the licensor is not represented as endorsing the use made of the work. The full details of the license are available at http://creativecommons.org/licenses/by/4.0.

CC BY NC SA: The CC BY-NC-SA license allows users to copy, to create extracts, abstracts and new works from the Article, to alter and revise the Article, provided this is not done for commercial purposes, and that the user gives appropriate credit (with a link to the formal publication through the relevant DOI), provides a link to the license, indicates if changes were made and the licensor is not represented as endorsing the use made of the work. Further, any new works must be made available on the same conditions. The full details of the license are available at http://creativecommons.org/licenses/by-nc-sa/4.0.

CC BY NC ND: The CC BY-NC-ND license allows users to copy and distribute the Article, provided this is not done for commercial purposes and further does not permit distribution of the Article if it is changed or edited in any way, and provided the user gives appropriate credit (with a link to the formal publication through the relevant DOI), provides a link to the license, and that the licensor is not represented as endorsing the use made of the work. The full details of the license are available at http://creativecommons.org/licenses/by-nc-nd/4.0. Any commercial reuse of Open Access articles published with a CC BY NC SA or CC BY NC ND license requires permission from Elsevier and will be subject to a fee.

Commercial reuse includes:

- Associating advertising with the full text of the Article
- Charging fees for document delivery or access
- Article aggregation
- Systematic distribution via e-mail lists or share buttons

Posting or linking by commercial companies for use by customers of those companies.

20. **Other Conditions**:

v1.10

Questions? customercare@copyright.com or +1-855-239-3415 (toll free in the US) or +1-978-646-2777.